SOLVATION FORCES AND CONTACT MECHANICS AT THE NANOMETER SCALE IN MOLECULAR LIQUIDS

NITYA NAND GOSVAMI

NATIONAL UNIVERSITY OF SINGAPORE

2008

SOLVATION FORCES AND CONTACT MECHANICS AT THE NANOMETER SCALE IN MOLECULAR LIQUIDS

NITYA NAND GOSVAMI

B. Tech., Metallurgical Engineering
Institute of Technology, Banaras Hindu University (IT-BHU), India

A THESIS SUBMITTED FOR THE DEGREE OF

DOCTOR OF PHILOSOPHY

DEPARTMENT OF MECHANICAL ENGINEERING

NATIONAL UNIVERSITY OF SINGAPORE

2008

Acknowledgements

I would like to express my sincere gratitude to a number of unforgettable people whom I worked with as well as got to know closely during my research work at the Institute of Materials Research and Engineering (IMRE) and the National University of Singapore (NUS). I'm thankful to my supervisors, Dr. Sujeet Kumar Sinha for giving me a great opportunity to pursue my research at NUS and providing incessant moral support and motivation, Prof. M. P. Srinivasan for helping me throughout my research with his immense knowledge of chemistry, and most importantly, Dr. Sean O'Shea, who not only brought me closer to the reality of science, but also enthralled me with his kindness, quick wit, remarkable patience and extraordinarily inspiring supervision. I'll particularly miss the exciting group discussions at our favorite hangout place, *Pasir Panjang Village.*

I would like to thank Dr.Wulf Hofbauer for several exhilarating discussions, which gave me a flavor of his in-depth knowledge and experience and Prof. Chandrasekhar Natarajan for unwearyingly answering my never-ending list of questions. I would also like to thank my close friends at IMRE including Lena Lui, Ong Yi Ching, Leonard Lim, Linda Kunardi, Dr. Cedric Troadec, Kedar Hippalgaonkar, Dr. Abir De Sarkar and Dr. Rajeev Ahluwalia for their generosity and constant support, as well as Dr. Satyanarayana Nalam from NUS and Dr. Sudhiranjan Tripathy from IMRE for providing me a great opportunity to work together on several interesting ideas.

Last but not least, I'm truly grateful to my parents for their constant care and motivation, which is the biggest strength for my accomplishments.

Table of Contents

Summary

Solvation forces and contact mechanics between two confining surfaces at the nanometer scale is studied using the atomic force microscope (AFM), in particular with conducting cantilevers. Force curves with simultaneous current measurements revealed that continuum models are followed for a nanoscale contact in various liquids for the probe interacting with the underlying substrate (graphite) and with an ordered "solid-like" molecular monolayer (e.g. hexadecane). Similar behavior was observed for the confined monolayer of a heavily branched molecule 2,6,10,15,19,23-hexamethyltetracosane (squalane), which was previously believed to be in a disordered state. The solid-like behavior of the squalane monolayer was further confirmed by direct scanning tunneling microscopy (STM) imaging, in agreement with a recent simulation study. For solid-like monolayers (e.g. hexadecane, squalane) another distinct characteristic is that just prior to the squeeze-out of the confined monolayer, the molecules rearrange within the contact zone such that the tip-substrate separation decreases.

The squeezing of a monolayer of molecules which do not form an ordered solid-like layer (2,2,4,4,6,8,8-Heptamethylnonane (HMN) in our study) does not follow any continuum mechanics model. The tip-contact also fails to follow continuum models at higher loads, where the tip is in contact with the substrate. This is postulated to arise from the trapping of the disordered confined molecules, as indicated in a recent simulation. Such trapping occurs when the confined material is more "liquid-like". The trapping mechanism was corroborated by repeating the experiments at much slower speeds, for monolayer of

short-chain linear alkanes which are in disordered state at room temperature and at temperatures above the solid phase melting transition of ordered monolayers of hexadecane and squalane.

Solvation forces on a self-assembled monolayer (SAM) surface are also studied using conducting AFM (C-AFM) in order to understand the effects of surrounding fluids on measured contact resistance. The results show that solvation layering of liquids can also occur on a SAM surface. The measured contact resistance of the SAM is not affected by the solvation layering of liquids near the SAM surface. However, the mechanical response of the SAM is affected due to the change in the surrounding mediums, which has a significant influence on the measured resistance.

List of Tables

Chapter 3

Chapter 4

List of Figures

Chapter 1

Chapter 2

Chapter 3

Chapter 4

List of Abbreviations

AFM	Atomic force microscope
C-AFM	Conducting AFM
C10	Decane
C12	Dodecane
C14	Tetradecane
C16	Hexadecane
C_nH_{2n+2}	Linear alkanes
C10SH	Decanethiol
DLVO	Derjaguin-Landau-Verwey-Overbeek
DMT	Derjaguin Muller and Toporov
DSC	Differential scanning calorimetry
eSFA	Extended surface force apparatus
FCS	Fluorescence correlation spectroscopy
FSC	Fast spectral correlation
GIXD	Grazing incident X-ray diffraction
HMN	2,2,4,4,6,8,8-Heptamethylnonane
HOMO	Highest occupied molecular orbital
HOPG	Highly oriented pyrolytic graphite
I-V	Current-voltage
JKR	Johnson, Kendall and Roberts
LUMO	Lowest unoccupied molecular orbital
MD	Maugis-Dugdale
OMCTS	Octamethylcyclotetrasiloxane
SAM	Self-assembled monolayer
SFA	Surface force apparatus
SM-AFM	Sample modulation atomic force microscopy
SPM	Scanning probe microscopy
Squalane	2, 6,10,15,19,23-Hexamethyltetracosane
STM	Scanning tunneling microscopy
TB	Through-bond
TS	Through-space
UHV	Ultra high vacuum

List of Symbols

A_a Apparent contact area

A_r Real contact area

A_i Sum of the areas of contacting asperities

a_0 Contact radius at zero applied load

a Contact radius

a_s Contact radius at adhesion force minima

A_1 AC component of sample oscillation

A_0 DC component of sample oscillation

α =1 corresponds to the JKR model and α =0 corresponds to the DMT model.

β Decay coefficient for tunneling through the molecule

$\beta_{i.}$ Interaction damping

β_c Cantilever damping

c Outer radius

Γ Surface energy or the work of adhesion.

d_1 AC component of cantilever oscillation

d_0 DC component of cantilever oscillation

D Surface separation

δ_e Elastic deformation

δ_p Plastic deformation

δ Total deformation

δ' Phase Shift

E Elastic modulus

E_F Fermi level of metal electrode

E_{vac} Vacuum energy level

F Total force

F_c Adhesive force

F_a Applied force

$\hbar$ Plank constant $(\hbar = h/2\pi)$

h_0 Tip-sample distance where adhesive force is zero

H Hysteresis Ratio

i_t Tunneling current

k_c Spring constant

k_i Tip-sample interaction stiffness

K_s Spring stiffness

K Effective elastic modulus

λ Maugis parameter

l Mean free path of an electron

m Ratio between the contact radius a and c

m_e Effective mass of the electron

m^* Effective mass

N_e Electron density

N Number of molecules within the junction
p Fermi momentum
q Electronic charge
ρ Resistivity of the junction
R Electrical Resistance
R_M Maxwell resistance
R_{sh} Sharvin resistance
R_0 Eeffective resistance
r Tip radius
s Barrier width (Tunnel gap)
σ Molecular diameter
T Transmission coefficient
ν Poisson's ratio
V Applied voltage
V_c Cantilever deflection
V_{c0} Cantilever deflection (away from the surface, at F=0)
ϕ Local tunneling barrier height
ω Oscillation Frequency
Z Piezoelectric displacement
Z_0 Displacement Z where the cantilever deflection for $V_c = V_{c0}$
z_0 Equilibrium separation distance
Δz Spring deflection
Ω Sensitivity of the photodetector

Chapter 1

Introduction

1.1 Motivation

Understanding the interaction between two surfaces is of immense importance for solving various complex scientific and engineering problems [1]. Examples include friction, adhesion, wear, lubrication, deformation, fracture, colloidal suspensions, biological interactions etc. The contact mechanics, both static and dynamic behavior, at the nanometer or single asperity level underpins the complex surface interactions occurring at the macroscopic scale. This is due to the fact that the contact between engineering surfaces is dominated by asperities [1]. A typical contact between two macroscopic bodies is shown in Fig. 1.1, where the apparent contact area between surfaces is A_a and area between two contacting asperities is A_i. The real area A_r is the sum of the individual asperity contacts (Eqn. 1.1) and is almost always much smaller than the apparent contact area. The real contact area is a key parameter in tribology [1] and is required for calculations of various contact mechanics parameters such as friction, adhesion, stress, deformation etc [2].

Experimental techniques such as surface force apparatus (SFA) and atomic force microscopy (AFM) [3, 4] have for the first time allowed experiments to be performed with single asperity geometry. The Atomic Force Microscope (AFM) has become a routine tool to study force interactions and mechanics down to the nanometer scale. In AFM, a sharp (~ 20 nm radius) tip is brought into contact with a surface, equivalent to a single asperity. Thus, AFM measurements on different surfaces and in different mediums

can be used to understand the fundamental mechanical behaviour of a single asperity contact.

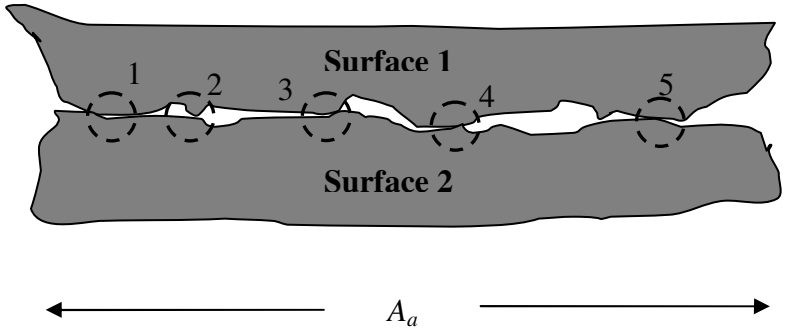

$$A_r = \sum_{1}^{n} A_i \leq A_a \tag{1.1}$$

Figure 1.1: Microscopic view of the contact area between two macroscopic objects. The apparent contact area is A_a and the real contact area is A_r, which is the sum of the individual asperity contacts A_i.

Simple theoretical models have also been developed since the first work by Heinrich Hertz in 1882 [5] to understand single asperity contact mechanics for elastic bodies. Hertz theory assumes negligible adhesion between the contacting bodies. Johnson, Kendall and Roberts (JKR) refined Hertz theory in calculating the theoretical displacement or indentation depth in the presence of adhesion [6]. Derjaguin, Muller and Toporov (DMT) [7] also modified the Hertz theory to take into account the adhesive forces between surfaces for very hard materials. Details of these theoretical models and their application in AFM are presented in Chapter 2. Several studies including our data (Chapter 4) have provided sufficient evidence that single asperity contact mechanics theories are valid for AFM experiments in many cases.

The problem of understanding interactions between two surfaces can become even more complex in the presence of an intervening medium, such as liquids in our studies. The theoretical foundation of force interactions between two approaching surfaces in a liquid medium was laid by Derjaguin-Landau-Verwey-Overbeek, known as the DLVO theory [8, 9]. The theory explains interactions between the surfaces by taking into account two opposing forces, attractive van der Waals forces and the repulsive double layer force [10] which is electrostatic in origin (see Fig 1.2). The van der Waals force is well described by continuum theories (Lifshitz theory [11]) and the double layer force by the Poisson-Boltzmann equation [10], both are long range interactions.

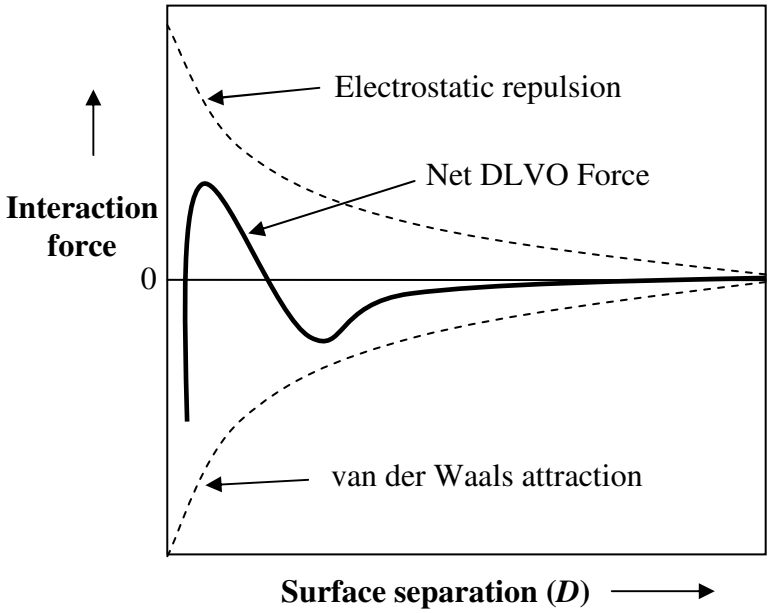

Figure 1.2: Typical force interaction curves of DLVO theory. Electrostatic repulsion and van der Waals attraction force curves are shown with dashed lines. The net DLVO force is indicated by the solid curve which is an algebraic sum of the two forces.

Later, further theoretical study and experimental work using the SFA in 1981 [3] showed the existence of oscillatory-type, short range forces in liquids when separation between the surfaces approached a few molecular diameters (see Fig. 1.3). Such forces could not be explained by the DLVO theory and result from a completely new phenomena, namely the formation of liquid into discrete layers near surfaces. The forces corresponding to the formation of the layers are termed "solvation forces".

AFM experiments [12] conducted in liquids also revealed the presence of solvation forces even at the nanometer lengthscales. Solvation forces hold importance in understanding the behavior of colloidal suspensions [13], nanofluidics [14], AFM imaging in liquids [15], tribology (i.e. adhesion, friction and wear) [16], interactions in biological systems [17] and more recently in scanning probe microscopy (SPM) studies of electron transport in single molecule experiments undertaken in liquids [18]. Further complexity in force interaction in liquid arises due to the fact that the intervening liquid itself can be very complex e.g. multi-component mixtures, amphiphilic, polymeric. Also, the confining walls are not necessarily ideally smooth and can be amorphous, crystalline, rough, crystallographically aligned or misaligned, rigid or soft and with varied surface chemistry (hydrophilic or hydrophobic).

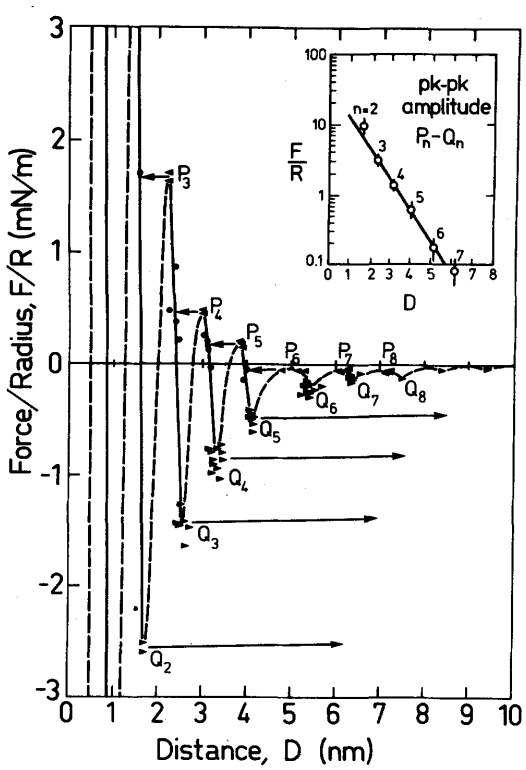

Figure 1.3: Measured oscillatory force between two mica surfaces immersed in the liquid OMCTS, an inert liquid of molecular diameter of ~ 0.85 nm. The arrows indicate inward or outward jumps from unstable to stable positions: the arrows pointing to the right indicate outward jumps from adhesive wells. The inset shows the peak-to-peak amplitudes of the oscillations as a function of surface separation (D), which have an exponential decay of decay length roughly equal to the size of the molecules. Data taken from ref. [3].

In this Thesis, the solvation forces and contact mechanics acting between two approaching surfaces have been studied using AFM in molecular liquids. A variety of inert and non-polar liquids (spherical, linear and branched) molecules are studied on graphite and self assembled monolayer surfaces to investigate fundamental problems related to solvation forces, boundary layer lubrication and charge transport across molecular layers. Specifically, experimental data is presented and resolved for the following problems; how is confined liquid squeezed out of a nanometer sized gap? What is the effect of molecular branching and the fluidity of the confined liquid on the squeeze-

out behaviour? To what extent can the conducting AFM technique be used to study the conductivity and related mechanical behaviour of confined fluids and monolayers?

1.2 Thesis Outline

Chapter 2 provides a review of non-DLVO forces, specifically oscillatory solvation forces as explored over the last two decades using SFA, AFM and computer simulations. Discussion is also given on the theoretical aspects of contact mechanics and charge transport mechanisms relevant to nanometer length scales. The details of materials and experimental methods used in this thesis are given in Chapter 3. The experiments of squeezing of "solid-like" monolayers of linear alkanes (hexadecane) and the branched alkane (squalane) using conducting AFM are detailed in Chapter 4. The data is explained using continuum mechanics models for an elastic solid for the tip either in contact with the underlying substrate or within the solvation layers. The use of conducting AFM allows more subtle details of the confined liquid to be observed and it is shown that rearrangement of the molecules (hexadecane and squalane) under the tip apex occurs just prior to the squeeze-out of the solvation layer closest to the surface. The solid-like nature of the hexadecane and squalane monolayer on graphite is verified by direct imaging using STM. In contrast, experiments on the branched alkane HMN, which forms a disordered monolayer, show striking differences in the solvation layering and squeeze-out behavior. Continuum elastic models cannot be applied to describe the contact, either on the disordered HMN monolayer or with the tip in contact with the graphite due to the trapping of HMN molecules within the tip-sample junction. Thus a clear difference is

demonstrated in the mechanical behaviour of a point contact depending on the order/disorder of the confined material.

In Chapter 5, the forces acting in a liquid is studied in the context of molecular electronics. Conducting AFM is undertaken on a decanethiol self-assembled monolayer (SAM) in three different fluids. The effect of solvation forces on the measured contact resistance of the SAM sandwiched between a Au(111) substrate and Au coated tip is found to be negligible. However, the surrounding medium strongly influences the mechanical response of the SAM and leads to a wide variation in the measured contact resistance. This is important as it demonstrates the interplay between mechanical response, environment and electrical behaviour when measuring electronic properties at the molecular scale.

Chapter 6 summarizes the major results and presents suggestions for future work.

Chapter 2

Literature Review

This chapter reviews the tremendous efforts which have been made in the past several decades to unravel the details of the properties of liquids under confinement between surfaces. Various tools have been used to understand the physics of confined liquids including computer simulations, surface force apparatus (SFA) and atomic force microscopy (AFM). These powerful techniques have revealed that liquids confined to extremely small volumes can behave like solids, non-Newtonian liquids or form ordered layers. Such behavior is entirely different from the bulk liquid and classical theories developed to explain interactions between two surfaces across a liquid medium are inadequate when the separation between surfaces approaches a few molecular diameters. Such dramatic behavior of confined liquids also carries great importance for various interfacial phenomena such as friction, adhesion and interactions in biological systems. In this chapter a review is provided of solvation forces and their measurement, with some emphasis on solvation on a graphite surface and the mechanical and electrical behavior of a point contact. The latter is essential for understanding the interaction of an AFM tip with a surface.

2.1 Solvation Force

The solvation force is a non-DLVO force which often exists when two surfaces are brought very close together (equivalent to 5-10 molecular diameters) in a liquid medium. Due to such extreme confinement, the liquid ceases to behave as a structureless continuum and can form discrete ordered layers, giving rise to a force which oscillates

with separation distance. For oscillatory solvation forces, the periodicity is equivalent to the diameter of the liquid molecules. These forces can arise purely from geometric packing, without any strong attractive liquid-liquid or liquid-solid wall interactions.

Oscillatory forces were first predicted theoretically in 1912 by Hardy [19]. The predictions of Hardy were corroborated by early experimental evidence of liquid structuring near liquid-solid interface or "deep surface orientation" in liquids, reviewed by Henniker [20]. Specific highlights of this early work are;

1. Taylor and King [21] found optical anisotropy in liquids much above the melting point of isotropic long-chain fatty acids. This effect suddenly disappeared as the temperature was further increased.
2. Lenher and McHaffie [22] found forces extending from the solid and from one molecule to another by exposing various solid plane surfaces to water or benzene vapor which allowed formation of films of defined thickness.
3. Boyes-Watson, Davidson and Perutz [23] showed methemoglobin crystals separated by layers of water using x-ray diffraction.
4. Brummage [24] found orientation patterns in films of straight-chain organic compounds, up to a critical temperature which was often well above the melting temperature, indicating some orienting influence due to the metal surface.
5. Deryagin and his group [25] showed about a ten fold increase in viscosity of an oil drop near a solid surface in comparison with the oil drop farther away from the solid.

6. Bradley [26] observed orientation through organic films while studying crystallization of ammonium iodide on mica, with or without a coating of cellulose acetate, showing propagation of the orientation effect of mica across the organic film.
7. Deryagin and Kusakov [27, 28] measured the compressive strength of a thin film of liquid compressed between a hydrogen bubble and a plane mica surface and found that the liquid film thickness reached an equilibrium value and became stable for several hours.

Henniker also reviewed several indirect experimental evidences for deep surface orientation including measurements of electrical conductance of oils, dielectric constant, multimolecular adsorption, x-ray diffraction, sciller layers, soap films, mechanical strength of liquid films, liquid flow in narrow passages, and adhesion. All these observations gave significant indications of short range structuring in liquids near liquid-solid interfaces.

However, none of the above experiments provided any details of the short range forces. The first direct experimental measurements of short range forces arising due to liquid structuring was only achieved in 1981 by Horn and Israelachvili using a surface force apparatus [3].

2.2 Experimental Techniques to measure Surface Forces

2.2.1 Surface Force Apparatus (SFA)

The development of the surface force apparatus (SFA) in 1981 by Israelachvili and co-workers [3] allowed a direct method to measure forces between two surfaces with great sensitivity in liquids.

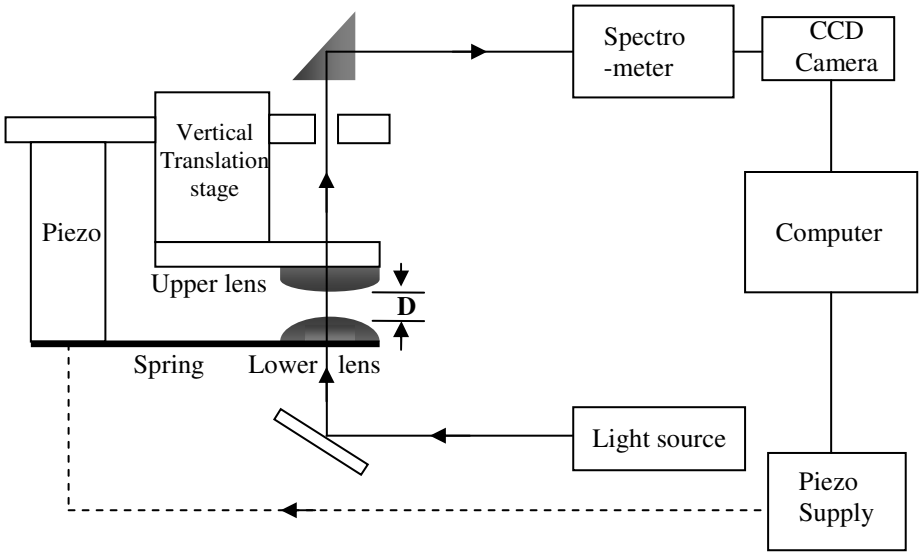

Figure 2.1: Schematic diagram of a conventional surface force apparatus (SFA). Two half silvered mica sheets are glued onto hemispherical lenses. The two mica surfaces are brought together using motor drives. The deflection of the spring holding one of the surfaces and the separation between the surfaces (D) is measured using optical interferometry.

Fig. 2.1 shows a schematic of the SFA which can measure adhesion and force-laws between two curved mica surfaces totally immersed in liquid or in gaseous media. The force (F) is found measuring the change in the spring deflection (Δz) and multiplying with the spring stiffness (K_s),

$$F = K_s \cdot \Delta z \tag{2.1}$$

An optical technique employing multiple beam interference fringes is used to estimate the separation between the surfaces (D) with an accuracy of ±1 Å. The separation of the surfaces can also be independently controlled to within 1 Å, using a piezo driven vertical translation stage and the force sensitivity is 10^{-8} N. The shape of interference fringes also allows quantitative estimation of the surface deformation to be found. The mica surfaces can be modified to study force interactions with various materials coated on the surface, such as polymers, monolayers, bilayers, metallic layers, protein layers etc [29-34]. A variety of liquids (aqueous, organic liquids and solvents, polymer melts, petroleum oils and liquid crystals, etc) have been studied.

Solvation forces were first observed using SFA by measuring forces between two mica surfaces immersed in a silicon liquid, octamethylcyclotetrasiloxane (OMCTS). Fig. 1.3 shows the original data with a clear oscillatory profile of the force between the surfaces. Subsequently, oscillatory forces were found to occur for almost all kinds of simple liquids and even for mixtures of liquids. The periodicity of the oscillations was equal to the molecular diameter of the confined liquid. A range of other forces between varieties of surfaces were studied with great sensitivity using SFA, including adhesion, friction, capillary, hydration and steric forces [35].

2.2.2 Solvation Forces using Surface Force Apparatus

An immense amount of work has been accomplished since the first development of SFA to study solvation forces and the various parameters affecting them, such as the structure of the liquid and the confining surface. In spherical or rigid molecular liquids such as benzene, toluene and OMCTS, oscillatory forces dominate the interaction between

surfaces below a separation of 5-10 molecular diameter. Similar effects were observed for linear molecules such as n-alkanes and alcohols. Asymmetric molecules with side groups or branching lack an axis of symmetry which can dramatically influence the solvation forces. For example iso-octadecane and polybutadienes showed a complete elimination of the oscillatory force law compared to their unbranched counterparts (octadecane and butadiene) [31, 36-38]. The molecular branches inhibit the formation of long range order within the confined liquid, thus decreasing the magnitude of the solvation force or in some cases completely removing oscillatory type behaviour.

For a liquid mixture the force laws were found to be unaffected if the volume fraction of the dominating component exceeds 90% [39]. However, for a 50-50 mixture, the forces were less well defined compared to the pure component. For a mixture of different shaped molecules, the oscillatory forces become even smaller in magnitude due to the inability of the molecules to pack well. For a mixture of immiscible liquids, the components can preferentially adsorb on the surface and dramatically affect the solvation forces, e.g. the presence of trace amounts of water can dramatically affect forces between two hydrophilic surfaces due to the preferential adsorption of water onto such surfaces [35].

The surface structure of the confining walls also significantly affects oscillatory forces [40-42]. The solvation forces were found to vary in magnitude with the registry between the lattice of the confining mica surfaces. Similar effects were found on the measured adhesive forces where different lattice registry can change the adhesion by a factor of two [43].

Apart from surface crystal structure, roughness plays a more crucial role for measurement of solvation forces. For randomly rough surface oscillatory forces can vanish completely even for roughness of the order of a few angstroms [44].

In recent years several advancements have been made in SFA to enhance the sensitivity of force measurements as well as to provide additional information about the confined liquid apart from simply measuring the force. Heuberger *et al* combined SFA with fast spectral correlation (FSC) interferometry, known as extended surface force apparatus (eSFA) [45], allowing simultaneous measurement of film thickness and refractive index with a much enhanced sensitivity than conventional SFA. The authors were able to determine density fluctuations within the probed volume extending over very long range (~ 1 μm). Importantly they concluded that the adhesive minima in the oscillations lie close to the expected continuum van der Waals force curve, which suggests that van der Waals adhesion cannot be enhanced by the deep energy minima of an oscillatory solvation force.

Granick and co-workers also modified the conventional SFA and integrated it with fluorescence correlation spectroscopy (FCS) [46]. This method allowed spatially resolved measurement of the rate of diffusion of the confined liquid molecules within the contact zone due to the change in the fluorescence intensity. These measurements showed that the diffusion rate varies within the contact zone, being more rapid near the periphery and slowest near the centre under confinement. The diffusion rates can be orders of magnitude slower than in the bulk liquid.

Another important modification of SFA has been to connect springs, detectors and motors such that the two surfaces can slide parallel to each other at a known separation [47-50]. Thus, the shear or friction forces can be measured in liquid. It is found that the shear force can also be quantized at nanoscale separation distances. The shear changes between discrete values depending on which solvation layer is being measured. Importantly, these experiments provide insight into the state of the confined material (i.e. does the material exhibit solid, glassy or liquid behaviour?), because the experiments can measure the time response of the sliding on application of shear [51]. The confined material becomes more solid or glassy under increasing confinement. For example, using OMCTS between mica surfaces, Granick *et al* [52] found the effective viscosity increased by three orders of magnitude as the separation between two surfaces was reduced from 7 layers to 2 solvation layers. Another remarkable result is the observation of stick-slip friction for highly confined liquids [47], a phenomena normally associated entirely with the sliding of solid materials.

2.2.3 Scanning Probe Microscopy (SPM)

Atomic force microscopy (AFM), scanning tunneling microscopy (STM) and their variations are collectively known as scanning probe microscopy (SPM). AFM was invented in 1986 by Gerd Binnig, Calvin Quate, and Christoph Gerber [4], shortly after the invention of STM by Gerd Binnig and Heinrich Rohrer [53]. These microscopy tools broke new ground as they allowed direct imaging of surfaces down to nanometer or even atomic scale.

The working principle of an STM (Fig. 2.2) involves scanning a conducting surface using a very sharp metal tip (a single atom at the end in most cases) which is controlled very close to the surface (within a nanometer or less) using piezoelectric actuators (or "piezoscanners") so that a tunneling current is detected. The tunnel current is maintained constant using the feedback electronics which adjust the tip-sample separation (D) in the surface normal direction (or z direction). In a second mode of operation the tunneling distance is maintained constant and the variation in tunneling current is monitored during scanning. This operation mode is called "constant height mode" and is good for a very flat surface because it allows much faster scanning as adjustment of the tip distance is not required. The piezoscanner enables rastering of the tip across the plane of the surface (the X and Y directions) which allows the STM to map the three dimensional electronic density of states of the surface. The tunneling current (i_t) varies exponentially with distance (s) as,

$$i_t \propto \exp(-2\chi \cdot s) \tag{2.2}$$

$$\chi = \sqrt{\frac{2m_e\phi}{\hbar^2}} \tag{2.3}$$

where m_e is the effective mass of the electron, ϕ is the local tunneling barrier height and $\hbar$ is the Plank constant. A 0.1 nm change in separation leads to an order of magnitude change in current. The exponential change in current over angstrom distances is the basis of the extremely high spatial resolution of STM, and remarkable lateral and vertical images of a variety of surfaces, down to the single atom level, can be obtained. Semiconductors [54], metals [55] and very thin insulating films, such as adsorbed organic

molecular layers on conducting surfaces [56], can be imaged with atomic/molecular resolution.

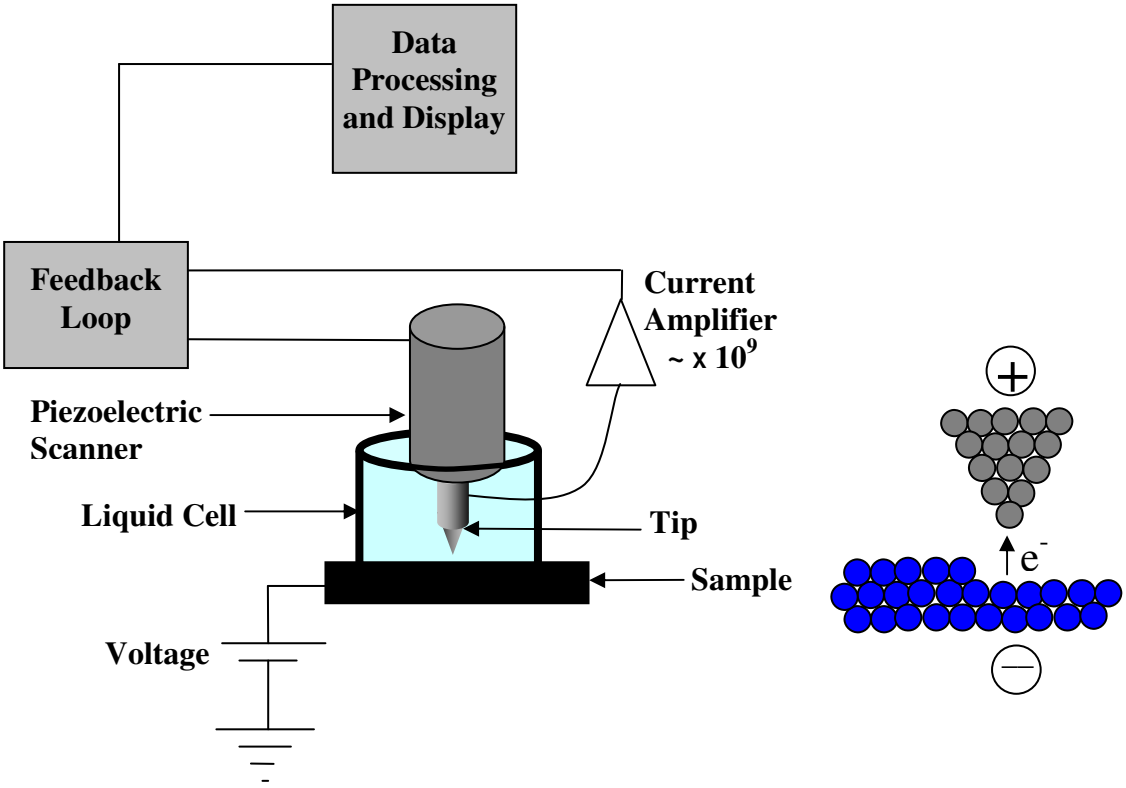

Figure 2.2 Schematics of the experimental setup for a scanning tunneling microscope.

In 1986 the AFM was invented [4] to overcome the limitation of STM having to operate on a conducting surface. AFM made it possible to image surfaces such as insulators and soft materials e.g. polymers and biological matter [57]. In the conventional, simplest version of an AFM setup (see Fig. 2.3), a tip is mounted at the end of a rectangular or a V-shaped micro-fabricated cantilever made up of Si or Si_3N_4. The deflection of the cantilever is monitored by shining a laser beam at the back of the cantilever and detecting the reflected laser by using a quadrant photodetector. The cantilever is approached to the sample surface using a coarse approach motor (just as in STM). At sufficiently close tip-

sample separation, the tip experiences a force interaction with the sample surface which deflects the cantilever, causing a shift in the position of the laser spot on the photodetector. The feedback controller electronics uses the photodetector signal to maintain a constant force (i.e. constant deflection of the cantilever) between the tip and the sample. An image of a surface can be produced by sweeping the voltage across the X and Y piezo scanners, as in STM, but in this case maintaining a constant deflection of the cantilever by controlling the Z piezo.

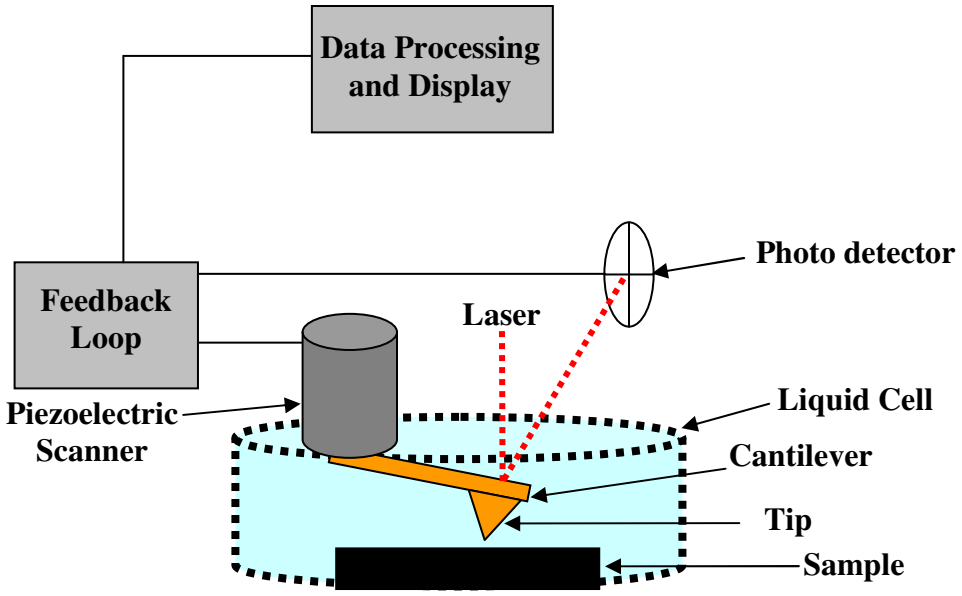

Figure 2.3: Schematic of an atomic force microscope for use in liquid.

The above laser system can easily detect extremely small vertical deflection (≤ 1.0 Å) of the cantilever and enables surface atomic structure to be imaged in real space. However, due to the finite contact area between the tip and sample when in mechanical contact, it is not possible to achieve true atomic resolution using the above static deflection

measurement technique. Images obtained give average information about the surface atomic structure and are termed "lattice resolution" [58]. Other imaging modes where cantilever is oscillated offer alternative imaging methods which can achieve true atomic scale resolution. The force interaction between the tip and the sample causes frequency, phase and amplitude changes in the oscillation of the cantilever which can be detected with higher sensitivity than measuring the static cantilever deflection [58]. The oscillation methods (also called AC, dynamic or non-contact AFM) also allow very soft samples to be studied (e.g. biological systems) which would be damaged due to high shear forces in static mode imaging. Dynamic modes of AFM mainly involve amplitude modulation where the change in oscillation amplitude or phase of the cantilever provides information about the force interaction. An alternative is frequency modulation where the change in the oscillation frequency is measured. This method allows a very small change in frequency shift to be detected and can achieve true atomic resolution in ultra high vacuum (UHV) [58] and very recently in liquids [59].

2.2.4 Solvation Forces using Atomic Force Microscopy

Solvation forces were first measured at the nanometer scale by AFM by O'Shea *et al* in 1992 [12, 60] using a Si_3N_4 cantilever on a graphite surface immersed in OMCTS and dodecanol. The period of force oscillations was commensurate with the diameter of the molecules. In OMCTS the solvation jumps were superimposed on an attractive van der Waals force while in dodecanol the solvation jumps were superimposed on a repulsive force. The background repulsive force in dodecanol arises because of the presence of trace amounts of water in the liquid, which preferentially adsorbs onto the tip surface

giving rise to an electrostatic repulsion from the resulting surface charge [61]. Initial experiments were performed in static mode. Later dynamic mode measurements were performed showing that such techniques provide a more sensitive measurement of solvation [62]. The AFM results were qualitatively similar but often differ in magnitude compared to SFA data. Differences could be due to much smaller confinement volume in AFM and nanoscale asperities at the tip apex dominating the interactions. Differences in AFM and SFA data due to microasperities was confirmed by Lim *et al* [63] by measuring solvation forces in OMCTS between a 10-μm size glass bead glued to an AFM cantilever and a graphite surface. Oscillatory forces were observed with the colloid tip but were the same order of magnitude as for sharp (~20 nm) AFM tips.

Dynamic AFM also allows the compliance and damping [64] of the confined liquid to be found. A marked increase in damping of the tip near the surface was found and linked to the increase in the effective viscosity of the confined liquid close to the surface. Recent measurements by Maali *et al* [65] and Patil *et al* [66] confirmed this interpretation. The dramatic increase in damping within the solvation layers close to a sample surface has serious consequences for non-contact imaging in liquid environments as the high resolution AC imaging techniques require a high mechanical quality factor to be effective.

Recently Fukuma *et al* achieved the first success in imaging up to two intrinsic hydration layers (i.e. solvation layers of water) adjacent to a lipid bilayer [67]. The results suggest that these hydration layers are stable enough to present multiple energy barriers to an

approaching nanoscale object e.g. proteins, ions etc which could affect membrane permeability. The molecular structure of the hydration layers revealed corrugations corresponding to the lipid head groups. Very large damping of the cantilever oscillations makes it difficult to probe the underlying substrate while imaging in non-contact mode [68]. The realization of true atomic resolution in liquids has opened a new era for AFM measurements, and solvation force studies will also benefit from this advance.

A variety of liquids has been investigated using AFM to understand the effect of molecular geometry on solvation forces. For example, Lim *et al* [69] reported the first experimental observation of solvation layering in a heavily branched alkane (squalane) using sample modulation AFM. This observation contradicted early SFA results which did not reveal any oscillatory force for several branched alkanes, including squalane [70]. More recently Granick *et al* revisited the problem using SFA and also confirmed oscillatory forces for squalane, and suggested the method of cleaving mica for SFA measurements could have dramatic effects on force measurements [71]. Repeated experiments by Israelachvili *et al* on squalane following Granick's experiments again showed monotonic force variation with no oscillations observed [72, 73]. Apart from force measurements using SFA and AFM, recent experiments employing neutron and helium atom scattering [74, 75] and X-ray reflectivity measurements [76] have indicated strong layering of squalane close to various solid surfaces, with squalane molecules lying parallel to the confining surface. A very recent simulation has shown for the first time that adsorbed squalane molecules can form ordered structures on a graphite surface [77]. Thus experiments performed on branched alkanes are still highly controversial [72, 73] and the effect of branching on solvation forces is still debatable.

In this work, the first experimental evidence of ordering in the highly branched alkane squalane is presented, which is in remarkable agreement with simulations [77]. However, another branched alkane HMN, which is asymmetric, more densely branched and with shorter backbone, remains in a disordered state. The effect of molecular ordering on solvation layering and squeeze-out of the two branched alkanes is addressed by simultaneously measuring force and current across the confined liquid using conducting AFM. The data reveals a strikingly different behaviour for the two branched alkanes, suggesting that their squeeze-out mechanism is different. The squeezing of the confined squalane monolayer reveals ordered solid like behavior and can be described by continuum mechanics model. Squeezing of HMN reveals significant variability in data due to its disordered state which leads to gradual thinning of the film. The ordered or disordered state of the confined liquid thus has a dramatic effect on the solvation force measurements.

2.3 Computer Simulations of Solvation Forces

Although SFA and AFM provided experimental evidence that confinement induced ordering which can lead to an oscillatory force profile in liquids close to smooth solid surfaces, these techniques have limitations in interpretation due to their restricted ability to perform experiments over wide length scales, time scales and selection of surfaces with specific chemistry [56]. Various theoretical approaches such as density functional and computer based Monte Carlo or Molecular Dynamics simulations have been employed to develop further understanding of the behavior and properties of confined liquids in the last three decades.

Mitchell, Ninham and Pailthorpe [78] examined the breakdown of continuum theories for particle interactions across liquids in the large distance regime and found that the Lifsitz theory still describes the interaction as the dominant contribution is the dispersion force. Mitchell *et al* also highlighted the work of Langmuir [79], Derjaguin [80] and Onsager [81], which had previously raised concerns over the possibility of short range structural forces, but were forgotten after the success of DLVO theory [7, 9]. Langmuir indicated that short-range structure can propagate from surfaces and from molecule to molecule giving rise to strong forces between surfaces [82]. In a subsequent paper Mitchell, Ninham and Pailthorpe [83] showed that short range forces due to liquid structuring dominate the particle interactions at small distances. Using Monte Carlo simulations, Abraham [84] showed that oscillatory forces may arise as an effect of liquid-structured wall interaction and liquid-liquid interaction. Snook *et al* [85-87] applied Monte Carlo simulation using canonical and grand canonical ensembles to understand the density profile of liquids confined between two hard walls and found strong density inhomogeneity of the liquids close to the solid walls, revealing the existence of solvation forces. Magda *et al* [88] used molecular dynamics simulations and also found density oscillations and solvation layering in confined liquids, in agreement with studies based on Monte Carlo simulations. Methods based on density functional theories were first developed by Tarazona [89-91] and Vanderlick *et al* [92] These also revealed density and force oscillations in hard spherical liquids confined between two solid walls, similar to the Monte Carlo results. Further theoretical efforts were being made to understand various key parameters affecting the solvation forces in liquids such as the shape of the confined molecules [93-96], roughness of the confining walls [97, 98] etc.

In view of the single asperity nature of the contact in AFM and SFA experiments, how liquids are squeezed out of the contact when two approaching surfaces interact with each other is of significant importance. This question also has direct relevance to lubrication, friction, adhesion and wear [99] and simulations have focused on understanding solvation forces for different molecular shapes, particularly linear and branched alkanes [93-95, 100-103]. The majority of computer simulation results reveals that linear alkanes form solvation layering with molecules arranged with their long axis parallel to the confining walls and are squeezed out of contact zone in discrete steps. However for branched alkanes, the layers are liquid-like due to the poor in-plane order [93, 94, 100-102]. Persson *et al* further extended computer simulations beyond density or force oscillations and studied layering transition i.e. the squeeze-out mechanism of a layer, for various linear and branched alkanes [99]. The squeeze-out process is an activated phenomena [104] and hence is strongly dependent on the temperature and rates of the experiment. A significant result was that squeeze-out of the last layer of a linear alkane leads to complete removal of the molecules from the contact zone above a critical pressure. However branched alkanes have poorer in-plane ordering and the squeeze-out of the last layer is very sluggish which leads to trapping of the molecules, even for a nanoscale contact [99]. This phenomena is shown experimentally in Chapter 4.

2.4 Contact Mechanics of Solids

Problems of contact mechanics such as friction and adhesion have been challenging since 15^{th} century. The first studies were attributed to Leonardo da Vinci (1452-1519), followed by Coulomb (1736-1806), Desaguliers (early 18^{th} century) and later pioneered

by Bowden and Tabor (1950) [1]. Surface roughness posed a great challenge to explain experimental results using theory because surface roughness makes it impossible to determine the real contact area. Elastic relaxation of high asperities break the adhesive contact of lower lying asperities, which makes analysis very difficult [2]. To circumvent these difficulties, experimental methods were developed to perform experiments with single asperity contacts. Once this was achieved with SFA and AFM, the data showed good agreement with continuum theories developed for single asperity contacts [35, 105]. Most of the analytical models deal with elastic contact at the asperity and these are revised below. Plastic deformation can also occur in AFM experiments but the underlying analysis is semi-empirical for nanoscale contacts.

The continuum models described below all assume the deformations to be purely elastic, the materials to be isotropic and the elastic properties of the materials to remain unchanged under load [2]. The atomic structure of the materials is not taken into account and the contact radius (a) should be small compared to the radius (r) of the contacting sphere (Fig. 2.4).

2.4.1 Hertz Model

Hertz develop the first model in 1881 [5] for an elastic contact of a sphere on a flat surface. All the surfaces were assumed to be perfectly smooth. The schematic diagram indicating the deformation mechanism according to the Hertz's model is shown in Fig. 2.4.

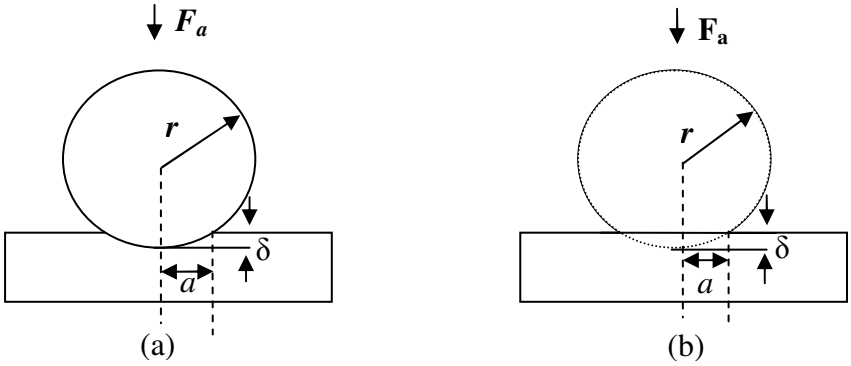

Figure 2.4 Schematic representation of Hertz contact mechanics model for a single spherical asperity in contact with a flat surface. (a) A rigid sphere pressed against a compliant plane substrate. (b) A compliant sphere is pressed against a rigid substrate. *r* is the radius of the spherical asperity, F_a is the applied normal load, *a* is the radius of the contact and δ is the elastic deformation.

Hertzian mechanics is applicable to contacts with negligible attractive surface forces or at high applied load. The adhesive force, (F_c) and contact radius at zero applied load (a_0), are zero. The important relationships in the Hertz theory are:

Contact radius, $$a = \left\{ \frac{3r}{4K} F_a \right\}^{1/3} \tag{2.4}$$

Elastic deformation, $$\delta_e = \frac{a^2}{r} = \frac{1}{r^{1/3}} \left(\frac{3F_a}{4K} \right)^{2/3} \tag{2.5}$$

Effective elastic modulus of the contacts, $$\frac{1}{K} = \frac{1-\nu_1^2}{E_1} + \frac{1-\nu_2^2}{E_2} \tag{2.6}$$

Here E_1 and E_2 are the elastic modulus of the sphere and the flat material, ν_1 and ν_2 are the respective Poisson's ratio, F_a the applied force, and *r* the sphere radius.

2.4.2 DMT Model

In most practical situations, the surface forces are not negligible, and $a_0 > 0$. Derjaguin, Muller and Toporov presented a simple model (DMT model) in 1975 [7] to take into account the adhesive force outside the contact region. The model takes adhesive force as a constant offset to the applied normal load. For a sphere on flat the adhesive force can be written, $F_c = 2\pi \cdot r\Gamma$, where Γ is the surface energy or the work of adhesion. The important relationships in the DMT model are:

Contact radius, $a = \left\{ \frac{3r}{4K} \left(F_a + F_c \right) \right\}^{1/3}$ (2.7)

Contact radius at zero applied load, $a_0 = \left\{ \frac{3r}{4K} F_c \right\}^{1/3}$ (2.8)

Elastic deformation, $\delta_e = \frac{a^2}{r}$ (2.9)

The DMT model assumes similar contact geometry as Hertz, i.e. loading and unloading is a smooth process, meaning no adhesion hysteresis is present for DMT contact. The DMT model fits well hard/rigid contacts where deformation due to adhesive forces outside the contact zone is negligible.

2.4.3 JKR Model

The Johnson, Kendall and Roberts (JKR) theory was proposed in 1971 [6] to describe the contact mechanics of systems with high surface energy, compliant materials and spheres with large radius. The theory takes into account the short-range surface-surface forces within the contact zone, including adhesive contributions. However it neglects the long range forces outside the contact zone, resulting in an infinite stress at the edge of the

contact. The loading and unloading process for JKR model involves hysteresis, i.e. the contact forms a neck which abruptly breaks when a negative load is applied (Fig. 2.5).

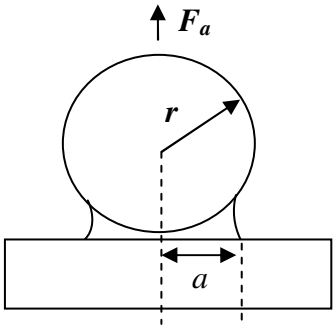

Figure 2.5 Schematic representation of JKR mechanics model for a spherical asperity contact with a flat surface. A neck forms at negative load while the sphere is detached from the surface.

The important relationships in the JKR model are:

Adhesive force for a sphere on flat, $F_c = \frac{3}{2}\pi \cdot r\Gamma$

Contact Radius, $a = \left\{\frac{3R}{4K}\left(F_a + 3\pi \cdot r\Gamma + \sqrt{6\pi \cdot r\Gamma F_a + (3\pi \cdot r\Gamma)^2}\right)\right\}^{1/3}$ (2.10)

Contact radius at zero applied load, $a_0 = \left\{\frac{3r}{4K} 6\pi \cdot r\Gamma\right\}^{1/3}$ (2.11)

Elastic deformation, $\delta = \frac{a^2}{r} - \frac{2}{3}\sqrt{\frac{6\pi\Gamma a}{R}}$ (2.12)

The contact radius at the adhesion force minima, when the sphere detaches the surface, is,

$$a_s = 0.63 \cdot a_0 \quad (2.13)$$

The JKR model has been extensively used to describe AFM point contacts.

2.4.4 Maugis-Dugdale Model

The Maugis-Dugdale (MD) model was developed in 1992 [106] and takes long range forces into account which were neglected in the JKR model. The MD model is thus more general and reproduces the Hertz, JKR and DMT models as special cases. Maugis used a parameter λ (first introduced by Tabor) which defines the applicability of a specific model for a given system. Here,

$$\lambda = \frac{2.06}{z_0}\left(\frac{r \cdot \Gamma^2}{\pi \cdot K^2}\right)^{1/3} \tag{2.14}$$

where z_0 is the equilibrium separation distance between the sphere and the substrate.

If $\lambda > 5$, the JKR model is followed. If $\lambda < 0.1$, the DMT model is followed.

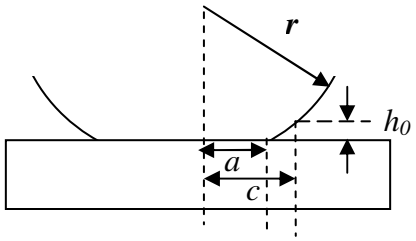

Figure 2.6 Schematic representation of the MD model for a spherical asperity contact with a flat surface. A constant attractive force acts over a circular region of radius *c* and the attractive force falls to zero at a tip sample distance of h_0.

For Maugis-Dugdale model, the load *F* is related to the contact radius *a* by the following two equations by the means of parameter *m*.

$$\frac{\lambda \cdot \hat{a}^2}{2}\left[\sqrt{m^2-1}+\left(m^2-2\right)\cos^{-1}\left(\frac{1}{m}\right)\right]+\frac{4\lambda^2 \cdot \hat{a}}{3}\left[\sqrt{m^2-1}\cos^{-1}\left(\frac{1}{m}\right)-m+1\right]=1 \qquad (2.15)$$

$$\hat{F}=\hat{a}^3-\lambda \cdot \hat{a}^2\left[\sqrt{m^2-1}+m^2\cos^{-1}\left(\frac{1}{m}\right)\right] \qquad (2.16)$$

where, $\hat{F}=\frac{F}{\pi \cdot r\Gamma}$ and $\hat{a}=a\cdot\left(\frac{K}{\pi \cdot r^2\Gamma}\right)^{1/3}$.

The parameter *m* represents the ratio between the contact radius *a* and an outer radius *c* (Fig. 2.6). The radius *c* represents the limit up to which a significant adhesive force is acting.

The MD model can be used to fit AFM data and provides a deep understanding of the mechanics of the contact [107]. However, analysis of the experimental data using Eqn. 2.15 can become overly complicated.

Carpick *et al* developed a generalized model [108] which helps to eliminate the mathematical difficulties. The relationship between load and contact radius for the generalized model is,

$$\frac{a}{a_{0(\alpha)}}=\left(\frac{\alpha+\sqrt{1-F_a/F_c}}{1+\alpha}\right)^{2/3} \qquad (2.16)$$

where $a_{0(\alpha)}$ is the contact radius at zero applied load. Using α=1 corresponds to the JKR model and α=0 corresponds to the DMT model. α is related to the Maugis parameter λ by an empirical expression,

$$\lambda = -0.924 \cdot \ln(1 - 1.02\alpha) \tag{2.17}$$

In this work, current vs. force data obtained using conducting AFM is fitted using the generalized model (Eqn. 2.16), which provides the value of the parameters α and $a_{0(\alpha)}$. Hence, the appropriate continuum models can be directly recognized based on the numerical value of α.

2.5 Charge Transport at the Nanoscale

The use of conducting AFM (C-AFM) requires an understanding of how current flows at nanometer length scales. The description of charge transport between two metallic electrodes either in physical contact or separated by a nanoscale gap (e.g. a monolayer of organic molecules) differs markedly from conduction at macroscopic length scales. A simplified theoretical background of charge transport at the nanometer scale is reviewed in this section.

2.5.1 Point Contact Conductance

When two conducting surfaces are brought into intimate contact with a nanoscale contact area of the junction, a "point contact" is established between the two surfaces. For a macroscopic junction area, the resistance is defined by Ohm's law where current across the junction varies linearly with voltage. However, when the size of the junction is smaller than the mean free path (l) of electrons in the material, the resistance of the contact does not follow Ohm's law [109]. At such length scales, the electron transport is ballistic i.e. in case where electron scattering is negligible or absent.

For an electron mean free path (l) much smaller than the contact radius (a) of the junction ($l << a$), the Maxwell resistance [110] formula (also known as spreading resistance or diffusive resistance) is valid. The point contact resistance (R_M) is given by,

$$R_M = \frac{\rho}{2a} \tag{2.18}$$

where ρ is the resistivity of the junction. For metals,

$$\rho = \frac{p}{N_e q^2 l} \tag{2.19}$$

where N_e is the electron density, q is the electronic charge and p is the Fermi momentum.

For an electron mean free path much larger than the contact radius of the junction ($l >> a$), the Sharvin resistance [111] formula is valid. The point contact resistance (R_{sh}) is given by,

$$R_{sh} = \frac{4\rho \cdot l}{3\pi \cdot a^2} \tag{2.20}$$

In AFM experiments the typical contact radius is of the order of a few nanometers, which is much smaller than the mean free path of electron in metals or in graphite. Thus, the Sharvin equation is used to fit the current vs. force data presented in Chapter 4. Note that at a fixed applied voltage, the current is proportional to the contact area ($\pi \cdot a^2$). Thus conducting AFM can be used to measure the change in contact area with load. The contact area is a fundamental measurement required for all the theoretical models of the mechanical response.

2.5.2 Tunneling through a Metal-Molecule-Metal Junction

A more common situation in AFM is to have a poorly conducting material (e.g. an oxide, protein, organic molecule, etc) sandwiched between the conducting surfaces of the tip and the substrate. In this thesis, solvation layers of organic liquids and self-assembled monolayers are studied. Thus, the experimental data needs to be modeled as a metal-molecule-metal electrical junction. A common approach to model charge transport across metal-molecule-metal junction is to approximate the transmission with a single barrier as used for dielectric materials, so that the salient electronic features can be discerned (Fig. 2.7).

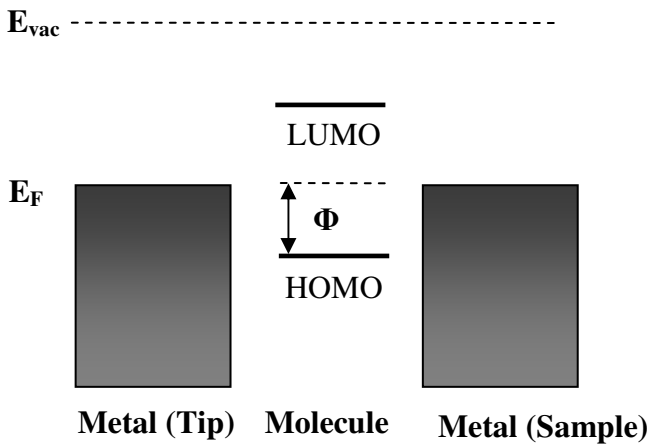

Figure 2.7: Diagram showing energy levels of metal electrodes (tip and substrate) and the molecules between the electrodes. E_F is the Fermi level of metal electrodes (assuming similar metals), E_{vac} is the vacuum energy level and Φ is the barrier height.

Such approaches are based on Simmons model for electron tunneling across a barrier [112] for which,

$$i_t = \pi a^2 \frac{q}{2\pi \cdot hs^2}\left[(\phi - qV/2)e^{-B.s\sqrt{\phi - qV/2}} - (\phi + qV/2)e^{-B.s\sqrt{\phi + qV/2}}\right] \quad (2.21)$$

where i_t is the tunneling current, ϕ is the barrier height, h is Plank constant, m_e is the electron mass, q is the electronic charge, V is the applied voltage, s is the barrier width and $B=4\pi\sqrt{(2m_e)}/h,$. More complex expressions can be obtained to include effective electron mass, non-rectangular barriers or image charge effects. At low bias Eqn. 2.21 can be approximated to,

$$i_t = \pi a^2 \frac{q^2\sqrt{2m_e\phi}}{h^2 s} e^{-B.s\sqrt{\phi}} V \quad (2.22)$$

Importantly, note that the current is proportional to the contact area. In conducting AFM experiments this allows the relative change in contact area ($\pi \cdot a^2$) to be monitored as a function of load. For molecular systems, Eqn. 2.22 is usually re-written $i_t = V/R$, with the resistance (R) defined as,

$$R = R_0 e^{\beta.s} \quad (2.23)$$

where $\beta=B\sqrt{\phi}$ is the decay coefficient for tunneling through the molecule and R_0 is the effective resistance of the molecule-metal contacts.

Engelkes *et al* [113] reported the inadequacies of Simmons model for molecules by careful analysis of the fitting of the I-V curves measured for metal-molecule-metal junctions formed by sandwiching alkanethiol self-assembled monolayers between a Au(111) substrate and a Au coated AFM probe. The resulting parameters were clearly in error e.g. the fitted contact area and the barrier height obtained generated unrealistic values. One difficulty is that the Fermi level of the metal contact should be close to either the molecule's highest occupied molecular orbital (HOMO) or lowest unoccupied

molecular orbital (LUMO) energy level for the Simmons model to be a valid approximation [114]. The exact position of the Fermi level is not known for saturated alkane molecules sandwiched between metallic electrodes. However, the HOMO-LUMO gap for adsorbed alkanes is large (~10 eV) and the metal Fermi level is "almost certainly" several electron volts from the molecule orbitals [115], thus making the utility of Eqn. 2.23 very doubtful. Another difficulty is that the Simmons type models do not describe the overlap of the molecular orbitals with the tip or substrate energy levels, which effectively lowers the transmission barrier [113]. An accurate description of the tunneling process across molecules must be done quantum mechanically, accounting for coupling between the electrode and molecule energy states. Approaches for molecules adsorbed on a metal surface include the use of an extended Huckel method [116], density functional theory [117] and a simple perturbation method [118] These approaches give good descriptions of the relative change in transmission across the adsorbed molecule and hence are useful to explain contrast variations in STM images. However, approximations and uncertainty in the numerical values of parameters limit the accuracy of all these methods for the calculation of the *absolute* current flow, which is the quantity of interest in this study.

For length scales smaller than the mean free path of electrons, of a metal-molecule-metal junction involves quantum coupling between the orbitals of the molecules, both of the metal electrodes, and through the binding sites of the molecule. The resistance (R) of such a contact junction is described by the Landauer formula [119]:

$$R = \frac{h}{2e^2 NT} \tag{2.24}$$

where T is the transmission coefficient which is determined by the net orbital overlap between electrodes and N is the number of molecules within the junction where the molecules can be treated as parallel resistors with only weak cooperative effects. Note that $2e^2/h$ is the quantum unit of conductance.

Following a simplified model of Engelkes *et al,* the transmission can be separated into components as $T = T_{tip}T_{sub}T_{mol}$ [113] , comprising the tip contact (T_{tip}), the substrate contact (T_{sub}) and the molecule (T_{mol}). Hence, Eqns. 2.23 and 2.24 can be combined in the low bias limit as,

$$R_0 = \frac{h}{2q^2 N_e}\frac{1}{T_{sub}}\frac{1}{T_{tip}} \tag{2.25}$$

$$e^{\beta \cdot s} = \frac{1}{T_{mol}} \tag{2.26}$$

The above equation is used in this work for estimation of *absolute* metal-molecule contact resistance.

2.6 Problems Requiring Nanoscale Current and Force Measurements

2.6.1 Lubrication and Friction

Macroscopic surfaces are composed of a large number of nanoscale asperities. The mechanical interaction between the surfaces is dominated by these asperities which dictate friction, adhesion and wear between the two surfaces. The contacting surfaces may have different bulk properties (perfectly elastic, perfectly plastic, elastic-plastic etc) which also have direct impact on the contact mechanics.

Several experimental approaches have been attempted to understand friction, adhesion and contact mechanics down to a single asperity contact, such as nano-indentation [120], SFA [35] and AFM [105, 107]. Nano-indentation experiments are limited to high levels of applied loads (typically several μN) [120], where severe surface deformation may take place. The SFA and AFM allows one to control forces to much lower levels (order of nN) which allows analysis of mechanical behavior of various surfaces within the elastic regime and facilitate studies of the mechanical properties of soft materials such as organic molecular layers [60] e.g. solvation layers of confined organic liquids and chemically or physically adsorbed molecular layers, which are the materials of interest in this dissertation.

The SFA studies material confined over distances of tens of micrometers, yet a tribology applications (see Section 1.1) concern how material acts when confinement occurs at nanometer length scales. The AFM measures forces between two surfaces but with typical contact areas of ~10nm^2. Thus AFM appears ideal to study fundamental tribology problems and a range of force interactions (solvation, friction, colloidal, DLVO etc.) have been measured between the AFM tip and a variety of surfaces. However, it remains experimentally challenging to obtain detailed picture of the mechanics of the contact because knowledge of friction, adhesion, stress, pressure, deformation, which requires the measurement of the contact area (see Section 2.4) and this is different at nanometer length scales.

Two approaches to obtain direct information of the nanoscopic contact area in AFM are to measure either the friction or current from the tip apex. Lantz *et al* showed that the variation of friction with load [105] is proportional to the contact area found by continuum mechanics theory (Maugis-Dugdale model). These results provided ample evidence that the AFM tip can be treated as a single asperity and friction is directly proportional to contact area for a single asperity contact. Lantz *et al* further performed indentation experiments using a metal coated AFM tip [107] and measured the variation of current with load at constant voltage, assuming current is directly proportional to the contact area. The variation of current with load was again found to be in excellent agreement with the Maugis-Dugdale model.

Thus, the simultaneous measurement of the current and force provides a direct means of obtaining *relative* variation of contact area with load. However, using electrical measurements to obtain the *absolute* value of the contact area remains a serious challenge due to the limited information regarding nanoscale electrical properties of materials e.g. the mean free path of electrons is not known with great accuracy [107]. Also, for conduction across a confined organic film, as of interest in lubrication, the current variation is extremely sensitive to even sub-angstrom changes in separation between the AFM tip and the substrate [53].

Conducting AFM and continuum models are used throughout this thesis to interpret change in the tip-sample contact area under varying load. The alkanes used in this study form solvation layers on graphite. The layer closest to the graphite substrate is strongly

bound, which can be regarded as an adsorbed monolayer. Pressure must be applied to squeeze-out the molecular layers and bring the AFM tip and graphite surfaces together. Thus the alkane + graphite system provides a model single asperity system for problems in boundary lubrication and point contact mechanics in liquid. How is the lubricant squeezed out from the junction? What are the pressures involved? What is the state of the confined material? These are some of the questions of scientific and technical interest in tribology and, as shown in Chapter 4, conducting AFM can elucidate such issues by revealing subtle changes in the contact junction which are not observed in standard force measurement.

2.6.2 Molecular Electronics

Making reliable electrical contacts at the nanoscale with an ensemble of molecules is of interest for applications in molecular electronics. One of the key requirements is to obtain a reliable measurement of the conductivity of a single (or few) molecules. At present, reported molecule conductivity can differ by orders of magnitude for the same molecule measured using identical techniques. Numerous methods have been used to measure the conductivity of single molecules, and all are based on sandwiching the molecules to be measured between two metal electrodes. These methods have been shown in the following research:

1. Gregory *et al* [121] presented a simple method to make electrical contact to molecular layers using two conducting crossed wires separated by a monolayer of the adsorbed

molecules. Using this method the authors measured electrical conduction down to single molecule level and even single electron tunneling.

2. Reed *et al* [122] proposed the mechanical break junction, where a metallic wire is immersed in a solution of molecules to be studied. The wire is broken using mechanical bending stress. The molecules adsorb on the surface of the broken joints, which are then brought back together by releasing the bending stress until the onset of conductance enables one to perform electrical measurements on the molecules present within the junction.

3. Frank *et al* [123] used a drop of mercury as a gentle and variable electrode to measure electrical properties of a single carbon nanotube, making contact by dipping the nanotube within the mercury drop. Slowinski *et al* [124, 125] studied electrical transport properties across alkanethiol monolayers using a mercury drop electrode covered with a monolayer of alkanethiol molecules in a electrochemical solution. This method allowed thickness dependent measurement of charge transport across the monolayer by changing the size of the drop or by changing the length of adsorbed molecules. They concluded that charge transport across the alkanethiol monolayer has two major components: a through-bond (TB) component and chain to chain coupling or through-space (TS) component. The TB transport component is dominant.

4. Wold and Frisbie [126] used conducting AFM to contact organic thin films, specifically self-assembled monolayers (SAM). The C-AFM technique has advantages over the other techniques in terms of the simplicity of use, molecular spatial resolution and the ability to simultaneously measure mechanical and electrical

properties of the molecular junction. Using C-AFM Frisbie *et al* conducted an extensive study of length dependent charge transport of various alkanethiol monolayers [113, 127], electrical breakdown of the junctions [128], charge transport across a bilayer junction [128], and the effect of end group chemistry and metal work function on charge transport [129]. A further refinement is to undertake C-AFM in a fluid environment [18]. This minimizes surface contamination and eliminates capillary forces, which in turn provides good control of the metal-molecule contact and minimizes damage of the molecular layers.

However, the central problem remains that a range of C-AFM studies conducted on simple monothiol self-assembled monolayers (SAM) in a variety of surrounding media (liquids and air) have a discrepancy by orders of magnitude in the measured contact resistance. Results of these studies have been reviewed by Salomon *et al* [130] but the detailed picture of the metal-molecule contact behavior in fluid media remains unclear. There have been a few recent studies to understand the effect of the surrounding media on molecular junction properties, namely; (i) Xiulan *et al* [131] showed that for electron transport through a single alkane dithiol molecule in various liquid media, the measured conductance was independent of the applied normal force and the fluid media used. This highlights an important distinction between dithiol SAM and the monothiol SAM showing that the transport properties of the dithiol SAM junction are independent of the media and the force because of the chemical binding of the molecule to the metallic electrodes. However, it is also important to note that many molecules of interest will not form a chemical bond to metal

electrodes, and a general method for measuring molecular conduction is desirable. (ii) Break junction studies of conductance of metal contacts [132] show significant variation in various liquid media and fluid layering was a proposed reason for such effect i.e. a higher resistance would be measured if the liquid were trapped between the tip and the SAM.

In Chapter 5, C-AFM is used to study the liquid monothiol SAM interface, the solvation layering which gives rise to oscillatory forces prior to the tip contact with the SAM, and the effect of these forces on the measured SAM contact resistance. The changes occurring in the transport characteristics of the junction in various surrounding media were also measured as a function of applied force. Hexadecane and OMCTS were chosen as liquid media as these liquids are completely inert and are geometrically well defined. These liquids have also been studied rigorously to understand confinement effects. It is found that electrical measurements of the alkane monolayer SAM junctions are highly dependent upon the elasticity of the SAM (which in turn may depend on the surrounding fluid) and the applied force because the tunnel current between the two metal electrodes is determined by the deformation of the SAM. Thus the measurement of the electrical properties of the molecular films is intimately connected to the mechanical response of the tip-sample contact, which changes with the local environment i.e. surrounding medium. This appears to be a key reason for the wide variation in the measurement of single molecule conduction.

Chapter 3

Experimental Methodologies

3.1 Scanning Probe Microscopy

Scanning probe microscopy (SPM) techniques were developed with the invention of scanning tunneling microscopy in 1981 [4, 53]. These techniques allow imaging of various surfaces using a physical probe which can be scanned over the surface using a piezoelectric scanner. The probe is scanned over the surface line by line to obtain an image of a surface. SPM has been proven to be an indispensable tool for the development of nanoscience and technology. This technique allows one to obtain a high resolution image of various material surfaces down to nanometer or atomic scale in real space and also it provides a means to simultaneously probe various surface interactions involving force, current, light, thermal gradient, spin polarized current, magnetic field etc. A disadvantage of SPM is it's slow speed to obtain images, although efforts are being currently made to greatly improve the rate of data acquisition. Various modes of SPM technique have been developed depending on the imaging interaction. Table 3.1 presents a list of some different variations of SPM:

Table 3.1: Modes of SPM

AFM • Contact mode • Force modulation mode • Tapping mode • Non-contact mode	Atomic Force Microscopy
FFM	Friction Force Microscopy
STM	Scanning Tunneling Microscopy
SNOM	Scanning Near-field Optical Microscopy
MFM	Magnetic Force Microscopy
KPFM	Kelvin Probe Force Microscopy
SECM	Scanning Electrochemical Microscopy
SThM	Scanning Thermal Microscopy
SPSM	Spin Polarized Scanning Tunneling Microscopy
SHPM	Scanning Hall Probe Microscopy
SCM	Scanning Capacitance Microscopy
EFM	Electrostatic Force Microscope
MRFM	Magnetic Resonance Force Microscopy
ESTM	Electrochemical Scanning Tunneling Microscope
SVM	Scanning Voltage Microscopy
SICM	Scanning Ion-Conductance Microscopy
PSTM	Photon Scanning Tunneling Microscopy
SGM	Scanning Gate Microscopy

3.1.1 AFM Setup

Fig. 2.3 shows a simple schematic diagram of an AFM used in this work. The commercial setup (Molecular Imaging Corp., USA) allows simultaneous measurement of tip-sample interaction forces as well as current flow between a conducting substrate and a metal (Au or Pt) coated AFM tip. For conducting AFM (Fig. 3.1), a conducting force sensing probe is connected to the virtual ground of a current to-voltage amplifier (Kiethley model 6485) with variable sensitivity of 1 V nA^{-1} to 1 V mA^{-1} and corresponding typical RMS noise levels of 20 fA to 100 nA. A 30 kΩ resistor is connected in series to limit the current. The sample is isolated from ground and connected to a voltage provided by the control electronics. STM experiments can also be performed using the same setup with STM scan heads. The microscope is placed inside an acoustic and mechanical vibration isolation chamber on a thick metal platform suspended with the help of stiff bungee chords. The isolation chamber is placed on an air table (Newport) which further dampens the mechanical vibrations. The measurements can be done either in air or in liquid environment. Liquid environment provides much less contamination and eliminates capillary forces allowing better control of tip-sample forces and improved imaging of soft materials such as self-assembled monolayers, biological systems etc. To perform AFM experiments in liquids, a Teflon liquid cell is mounted on top of the sample (Fig. 2.3). The cantilever is fully immersed inside the liquid cell to perform the AFM experiments.

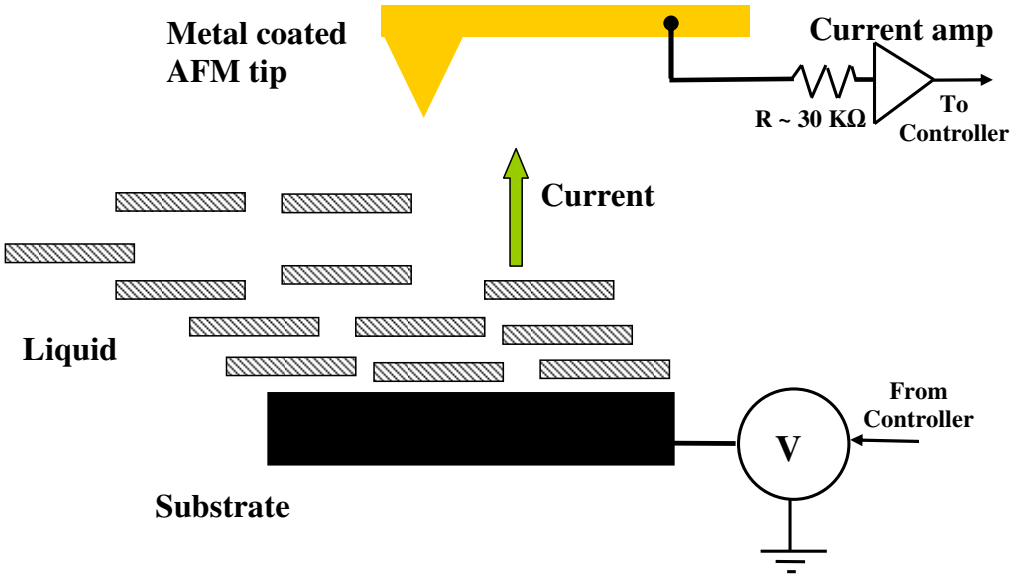

Figure 3.1: Schematics of a conducting atomic force microscope (C-AFM). The bias voltage (*V*) is supplied by the AFM control electronics. The output from the current amplifier is read as an additional input channel by the AFM controller.

3.1.2 Force Measurements in Static Mode

Most of the data presented in this work is undertaken in the contact (or static deflection) mode. The interaction force between the tip and the sample surface can be measured by monitoring the change in the static deflection of the cantilever upon interaction with the sample. In a typical force curve cycle acquired in a static mode AFM experiment, the cantilever is approached to the surface from a given distance by software controlled ramping of the Z-piezo DC voltage, the cantilever is pressed on the surface up to a certain limit and is retracted by reversing the Z-piezo voltage signal to complete the cycle. The raw data consists of the cantilever deflection and the change in displacement of the piezoelectric scanner during the approach and the retraction cycles. The force vs. tip-

sample distance curve can be obtained from the deflection vs. piezoelectric displacement curve using simple mathematical calculations.

As an example Fig. 3.2a shows a force curve taken on a decanethiol (C10SH) self-assembled monolayer (SAM) surface in OMCTS liquid. When the probe is distant from the SAM surface the deflection of the cantilever is constant (at value V_{c0}) as the force is immeasurably small. As the probe approaches closer to the SAM surface and starts interacting with the sample, the cantilever begins to deflect because of forces acting on the tip apex. In Fig 3.2a the steps observed in the deflection curve are due to the solvation layering of OMCTS. The tip pushes through individual OMCTS layers and squeezes them out above a certain force. After the last OMCTS layer is removed, the deflection of the cantilever shows a continuous linear increase with displacement due to the hard wall repulsion i.e. the tip is now in contact with the SAM surface. The retraction curve shows linear decrease in deflection with displacement as the cantilever is pulled away from the surface. Before the cantilever jumps off the surface (at point A) the deflection (V_c) goes lower than the level when the cantilever is far away from the surface (i.e. $V_c < V_{c0}$). This happens due to the adhesion of the tip to the SAM surface. Several solvation layers are observed in the retraction curve as well. Finally the cantilever deflection returns to a constant level (V_{c0}) far away from the sample as the force acting on the tip again becomes immeasurably small.

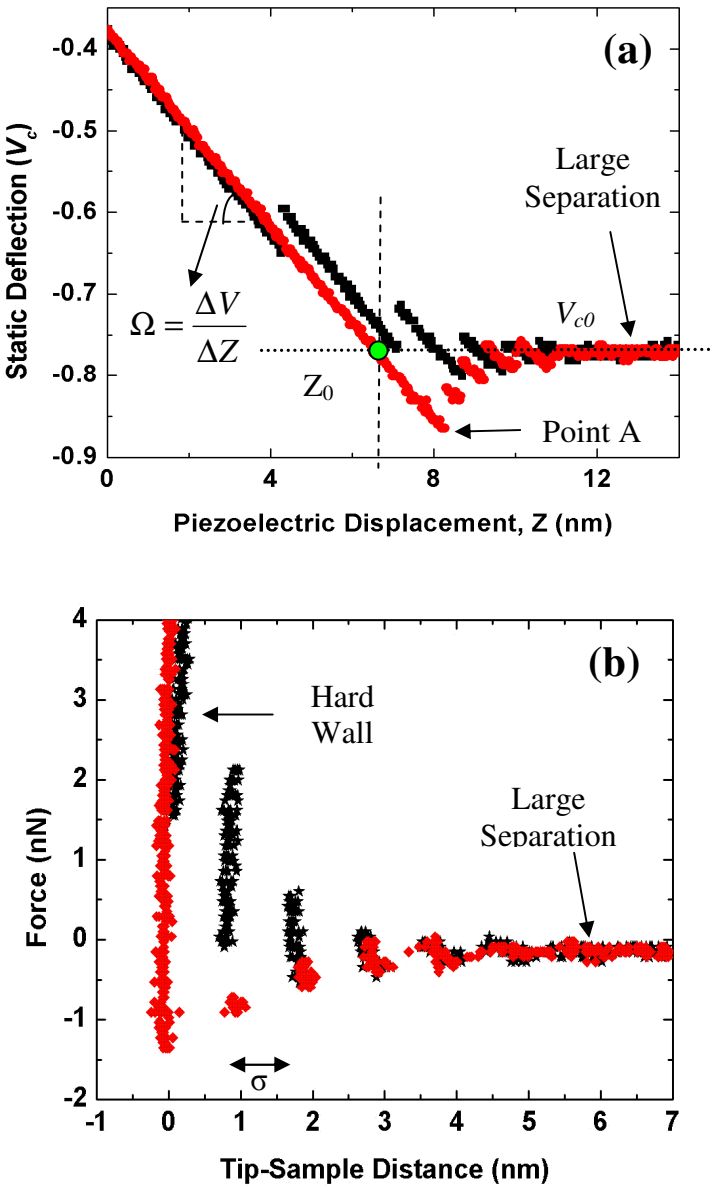

Figure 3.2: AFM force curve acquisition on decanethiol SAM surface in OMCTS. (a) Raw data: Approach (black) and retraction (red) curve showing cantilever deflection vs. piezoelectric displacement. The curve shows several jumps (solvation layers) before the tip contacts the sample surface. Z_0 and V_{c0} are defined by the dashed line. (b) Conversion of curve (a) to obtain true force vs. distance curve. The jump distance between the layers corresponds to the diameter of the OMCTS molecule. The tip contacts the SAM surface at D=0.

In order to extract the force vs. tip-sample distance curve (Fig. 3.2b), the piezoelectric displacement data (Fig. 3.2a) has to be modified. The force (F) can be directly calculated from the cantilever deflection using Hooke's law,

$$F = k_c \cdot \frac{(V_c - V_{c0})}{\Omega} \tag{3.1}$$

where k_c is the spring constant of the cantilever, V_c is the measured deflection of the cantilever (in volts) during a force curve acquisition and V_{c0} is the deflection of the cantilever far away from the surface (where F=0). The sensitivity of the photodetector (Ω in volts/nm) is calculated from the slope of the deflection curve in hard wall contact (see Fig. 3.2a),

$$\Omega = \frac{\Delta V_c}{\Delta Z} \tag{3.2}$$

The piezoelectric displacement (Z) can be accurately calibrated for an individual AFM (see Section 3.2.1). The tip-sample distance (D) is calculated from the piezoelectric displacement (Z) as,

$$D = (Z - Z_0) - \frac{(V_c - V_{c0})}{\Omega} \tag{3.3}$$

where Z_0 is the displacement Z where the cantilever deflection V_c equals V_{c0} with the cantilever in hard contact with the surface (see Fig. 3.2a).

The converted data (Fig. 3.2b) shows the tip contacts the surface at D=0 and the distance between the solvation "jumps" is ~8 Å, the approximate molecular diameter (σ) of the OMCTS molecule. The force required to squeeze-out a layer increases as the tip moves closer to the surface. Note that repulsive forces are positive and attractive forces are negative. In this example, the adhesive force (F_c) is -1.4 nN.

3.1.3 Sample Modulation AFM in liquids

In this work, the stiffness of the SAM samples is also measured directly using sample modulation atomic force microscopy (SM-AFM). This technique involves exciting a sinusoidal oscillation of the sample at a given frequency, with very small amplitude, and measuring the response of the cantilever as the stiffness and damping of the tip-sample contact changes [63, 133].

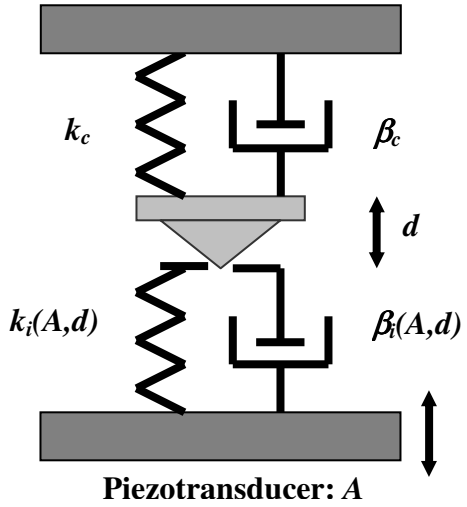

Figure 3.3: The rheological model for sample modulation where the amplitude of the piezotransducer [133] driving the sample is A and the tip displacement is d. The cantilever is represented by a spring with spring constant k_c, a dashpot with damping β_c, and an effective mass of m^*. The tip-sample interaction is represented by a spring k_i and a dashpot β_i.

At sufficiently small separations the oscillating sample induces vibrations in the cantilever because of the tip-sample interaction forces. To analyze the dynamic response of the cantilever for small amplitude sinusoidal oscillations, the cantilever motion can be approximated to simple harmonic motion. A schematic rheological model of the sample-modulation system is shown in Fig. 3.3. The tip displacement and the amplitude of the

sample motion are denoted with d and A respectively. The cantilever is represented by a spring constant k_c, damping β_c, and an effective mass of m^*. The tip-sample interaction stiffness is represented by a spring k_i (the desired quantity) with damping β_i. Note that the interaction stiffness is related to the tip-sample force as k_i = dF/dD, where F is the normal force and D is the tip-sample separation.

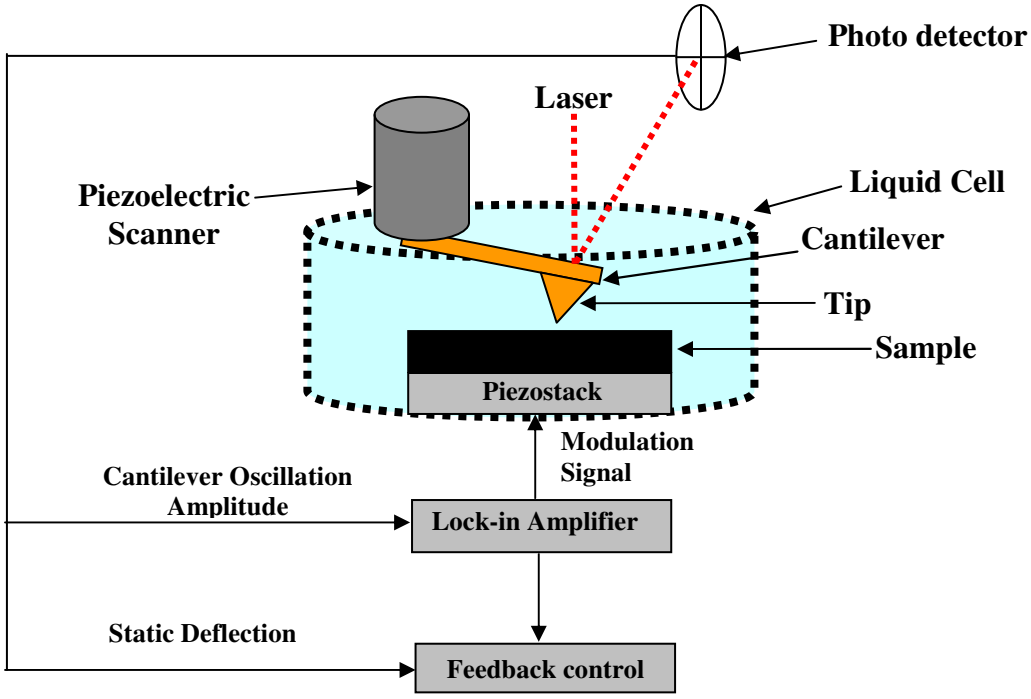

Figure 3.4: Schematic of the experimental setup for the sample-modulation technique.

The equations of motion describing this system are [134];

$$A = A_0 + A_1 \cos \omega t \,, \tag{3.4}$$

$$d = d_0 + d_1 \cos(\omega t - \delta) \,, \tag{3.5}$$

and

$$m^{*}\ddot{d} + 2m^{*}\beta_c\dot{d} + k_c d = 2m^{*}\beta_i(\dot{z} - \dot{d}) + k_i(z - d) \tag{3.6}$$

Where a single *dot* ('·') on *d* refers to the rate of change and a *double dot* ('¨') refers to the acceleration, δ' is the phase shift between the sample and cantilever motions. The subscripts 0 and 1 denote the dc and ac components respectively of *d* and *A*. The solution is

$$\frac{d_1}{A_1} = \frac{k_i[1 + (2m^{*}\omega\beta_i / k_i)^2]^{1/2}}{\sqrt{\left(k_i + k_c - m^{*}\omega^2\right)^2 + [2m^{*}\omega(\beta_i + \beta_c)]^2}} \tag{3.7}$$

and

$$\tan\delta' = \frac{2m^{*}\omega[\beta_i(m^{*}\omega^2 - k_c) + \beta_c k_i]}{k_i(k_i + k_c - m^{*}\omega^2) + (2m^{*}\omega)^2\beta_i(\beta_i + \beta_c)} \quad . \tag{3.8}$$

In the low-frequency limit ($\omega \to 0$), Eqn. 3.7 reduces to

$$\frac{d_1}{A_1} = \pm\frac{k_i}{k_i + k_c} \tag{3.9}$$

and the phase shift δ' becomes negligible.

Since the frequency of modulation used experimentally is always much lower than the resonance frequency of the cantilever, Eqn. 3.9 can be used to find the interaction stiffness k_i by measuring the change in the amplitude of the cantilever oscillation (d_1). The sample oscillation (A_1) and cantilever stiffness (k_c) are known.

To perform the experiments the sample is placed firmly onto a piezoelectric plate inside the AFM liquid cell (Fig. 3.4). A lock-in amplifier (EG&G 7265) is used to drive the piezotransducer and to measure the induced cantilever oscillations (d_1).

The experiments presented in Section 5.3.4 were performed using Si cantilevers of stiffness ~ 40 N/m (Nanosensors Gmbh). The resonance frequency of the cantilever was measured to be ~270 kHz in air. The sample is modulated at oscillation frequency of ~600 Hz, with a very small peak-to-peak amplitude (A_1) (~2 Å in our experiments). Detailed discussions of the measurement are given in Section 5.3.4. Thus Eqn. 3.9 can be used to find the interaction stiffness (k_i). Typically this is done as the tip-sample distance is varied, thus yielding a stiffness k_i versus distance curve.

3.2 AFM Piezo Calibration

The piezoelectric scanner moves the tip (or sample) in the horizontal (X, Y) or surface normal (Z) directions. Calibration is undertaken by imaging a known sample and the methods used in this work are detailed below.

3.2.1 Z Piezo Calibration

A freshly cleaved HOPG surface exposes a very clean atomically flat basel plane of graphite. The surface also consists of several atomic steps of well known height which can be used to calibrate the AFM/STM piezo scanner in the Z direction. Fig. 3.5 shows an AFM image of HOPG where a single atomic step and a double atomic step are

observed. The known individual atomic steps of HOPG are ~3.4 Å [135] in height and Z can be calibrated accordingly.

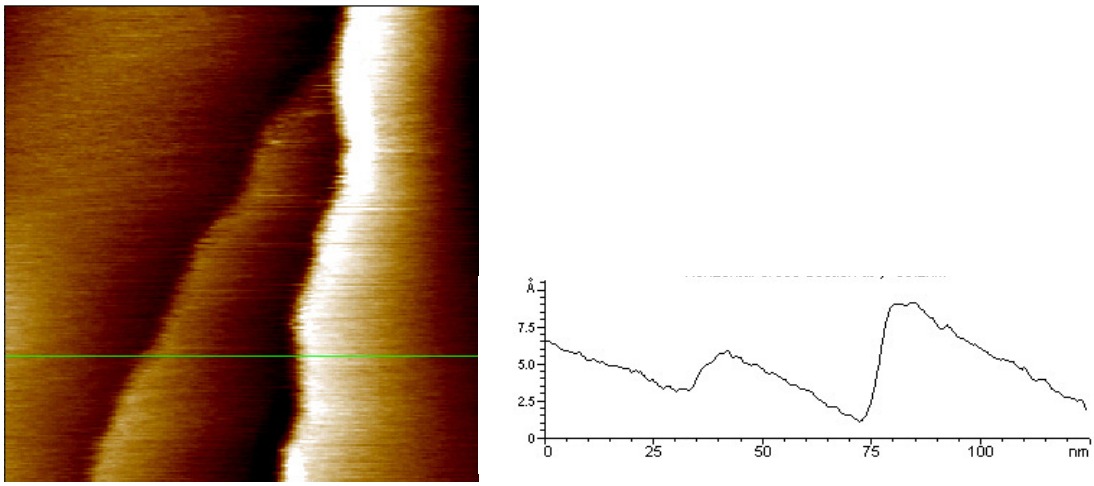

Figure 3.5: 125 nm × 125 nm contact mode AFM topographic image of a HOPG surface. Single and double atomic steps are observed with observed height of ~3.5 Å and ~7.0 Å respectively.

3.2.2 X and Y Piezo Calibration

Muscovite mica is used for calibration in the X and Y direction as the lattice resolution image of mica can be readily obtained in air. Muscovite mica is a naturally obtained mineral composed of silicates of aluminium and alkalis with hydroxyl (chemical formula: $H_2KAl_3(SiO_4)_3$) [136]. Mica is cleaved easily along the basel planes to provide an atomically flat surface over a very large area and is extensively used as a substrate. Fig. 3.6 shows the atomic structure of muscovite mica. The cleaved basel plane shows a hexagonal lattice with spacing of ~5.2 Å. Fig. 3.7 shows a lateral force microscopy image of mica revealing the hexagonal lattice. The X and Y piezoscanners can be calibrated from these images.

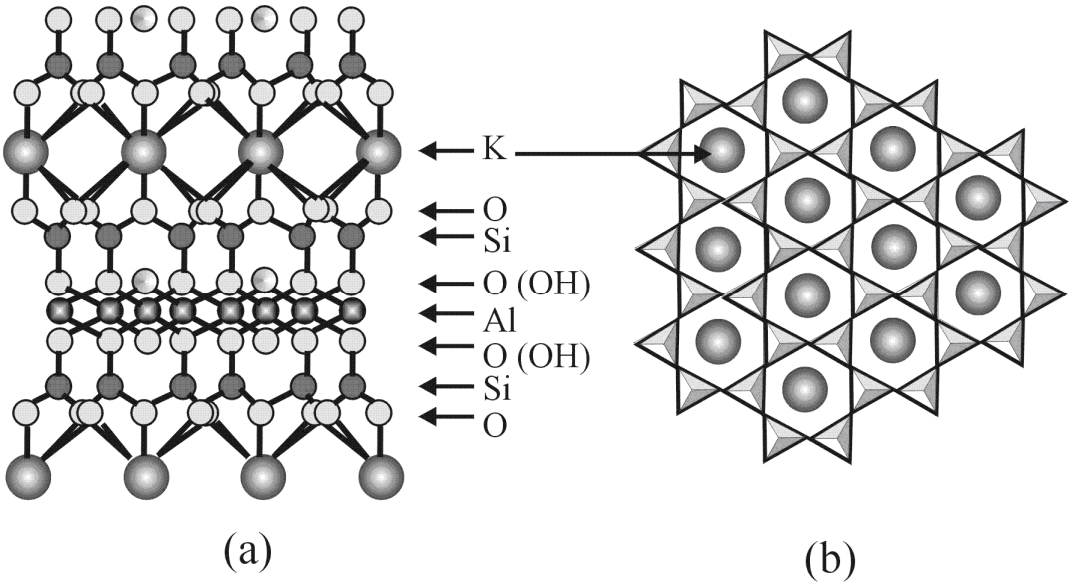

Figure 3.6: (a) The crystallographic arrangement of atoms in mica. (b) Top view of the atomic arrangement of mica [137].

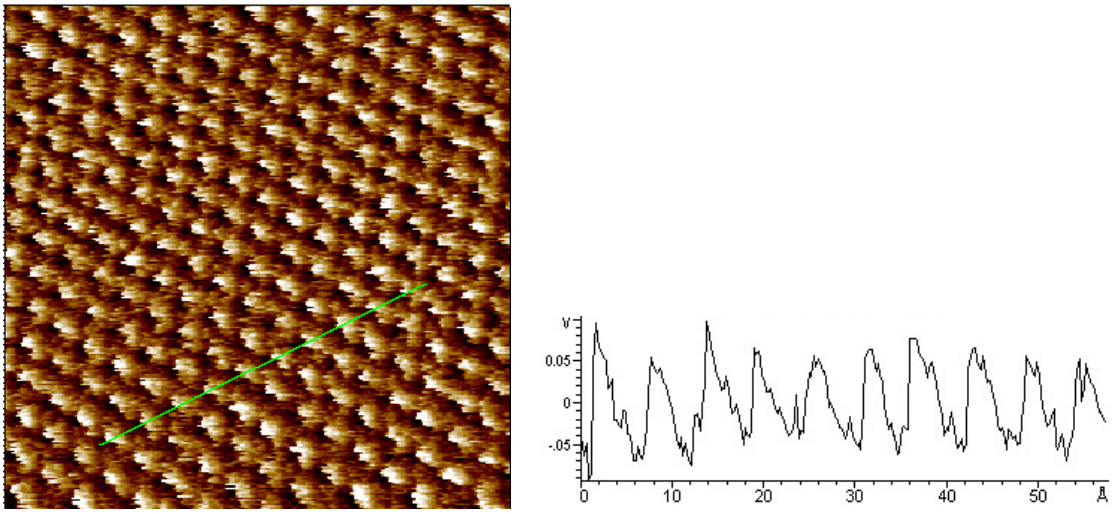

Figure 3.7: Lattice resolution image of a mica surface (8 nm × 8 nm) in friction mode. The hexagonal lattice is clearly observed.

3.3 Tip Preparation and Characterization

To perform the AFM experiments in contact mode for imaging, force curve and conducting AFM experiments, the choice of cantilever spring constant is critical. To

measure solvation forces, which are weak and short-range, soft rectangular cantilevers (Olympus RC800PSA (ORC8), spring constant 0.38 or 0.76 N/m) made of Si_3N_4 were found to be very suitable (Fig. 3.8). The dimensions and resonance frequency of the cantilevers, which together define the spring constant of the cantilever [138], were measured for every cantilever used and found to be in close agreement with the manufacturer's values.

To construct conducting AFM tips, Si_3N_4 rectangular cantilevers were coated with 5 nm Cr followed by 30-40 nm Au in a thermal evaporator at a pressure of ~2×10^{-5} Pa. All the tips were prepared fresh for each experiment as degradation in tip conductivity was noticed if the tips were stored in a dry box for several days. The change in spring constant of the cantilever due to Cr/Au coating was not taken into account, as this effect has been found to be negligible for thin films [139].

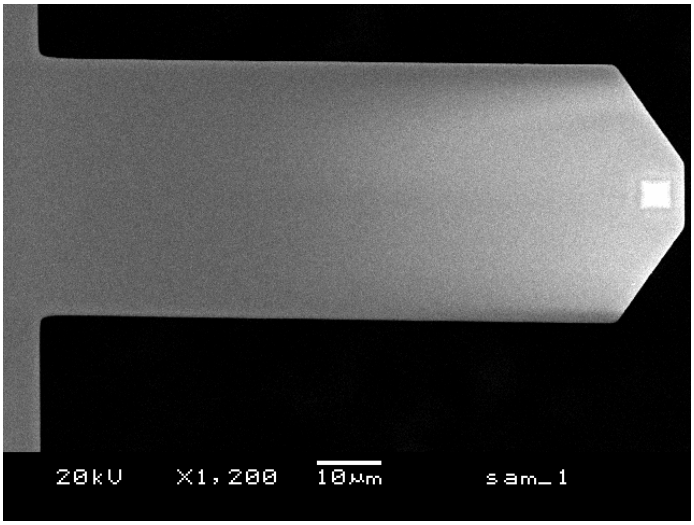

Figure 3.8: SEM image of a typical rectangular Si_3N_4 cantilever used in this work for contact mode imaging and measuring solvation forces. A pyramidal tip is mounted at the end of the cantilever.

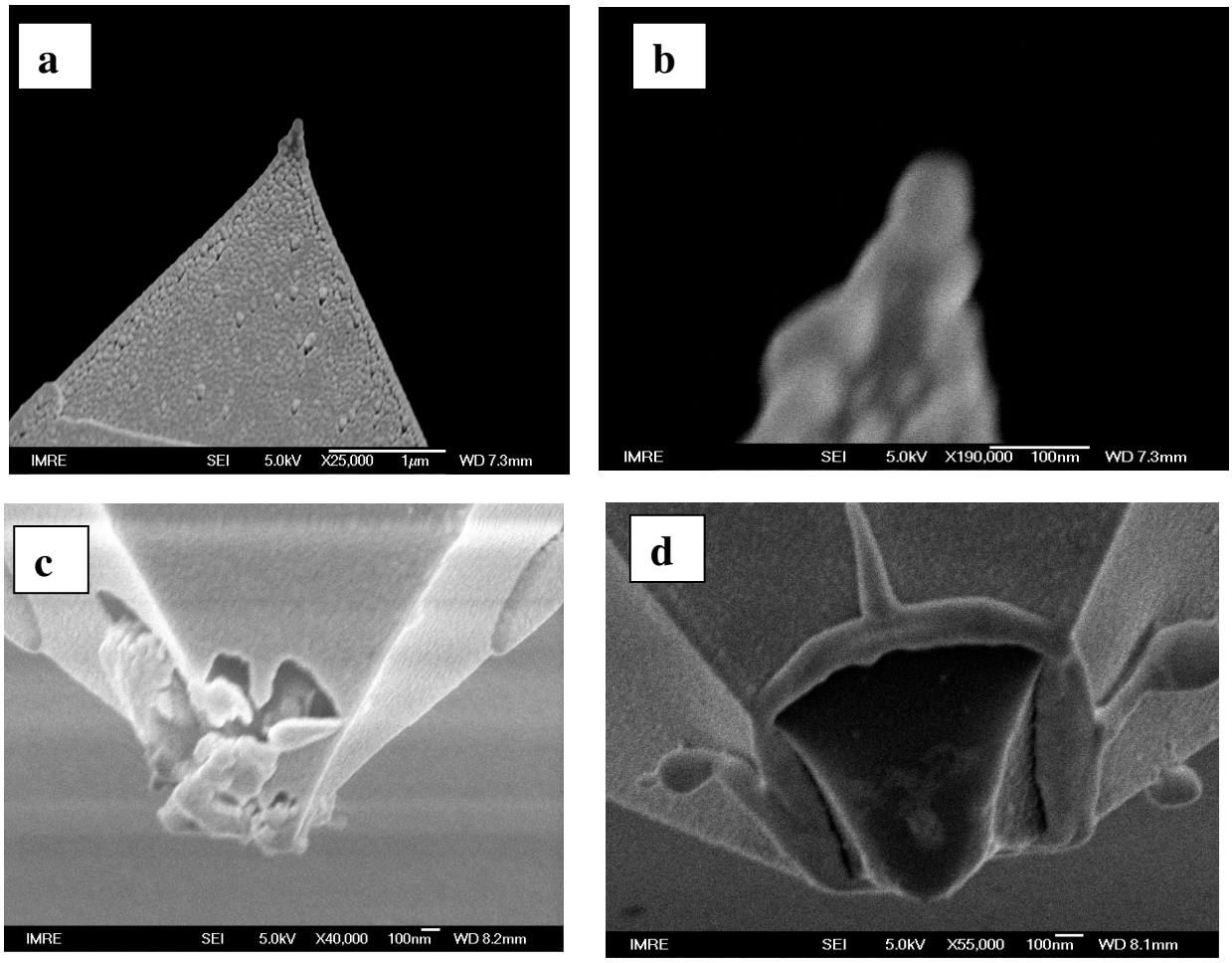

Figure 3.9: SEM images of the Au coated tips: (a) and (b) images of a tip obtained after force spectroscopy experiments. Such images are used to estimate the tip radius of curvature (in this case ~ 30 nm). (c), (d) SEM images of tips which were damaged during the experiments. In (d) melting of the Au coating has occurred.

Special precautions were taken for experiments with conducting cantilevers as the Au coating is very delicate. In contact with a sample extremely high stress (~1-2 GPa) occurs near the tip apex which can lead to damage or wear of the Au coating. Thus, the probes were not scanned very often on the surface and only a limited number of force curves (~10-20) were obtained with each individual probes. The voltage between the tip and sample was always kept below 1.0 Volts in all the experiments. At higher applied

voltages the Au coating at the tip apex may melt and also undesirable electrostatic forces start dominating the short range forces of interest. After each experiment, the tips were carefully imaged at high resolution using a FESEM to measure the tip radius of curvature and also to ensure the integrity of the Au coating (see Fig. 3.9).

3.4 Materials

3.4.1 HOPG

Highly oriented pyrolytic graphite (HOPG) is used in this study as a conducting, atomically flat substrate on which solvation forces can be easily observed in the chosen liquids. HOPG is a high purity crystal of carbon where the sheets of carbon (called "graphene") are stacked parallel to each other (Fig. 3.10). Within a sheet, the carbon atoms are covalently bonded, which makes HOPG a good conductor of heat and electricity along the atomic plane. Perpendicular to the atomic planes, the sheets are weakly bonded via van der Walls interactions which leads to poor electronic coupling of the carbon atoms and is the reason for poor thermal and electrical conductivity [140]. The weakly bonded layers make it easy to cleave HOPG using masking tape which produces a clean, atomically flat surface ideal for various microscopy experiments. Fig. 3.11 shows an STM image of HOPG after piezo calibration, showing a step height of ~0.35 nm which is close to the known value of ~0.34 nm [135]. The lattice image shows hexagonally packed carbon atoms with atomic spacing of ~0.25 nm after calibration. This spacing is different than the distance between carbon atoms within the atomic plane. This effect arises due to the ABAB…. type stacking of the atomic planes, where alternate atomic planes are shifted in such a way that only half of the carbon atoms (B atoms) in

one plane overlap with the carbon atoms in the adjacent plane. This is the reason STM images show hexagonal lattice images, where individual bright spot correspond to the alternate carbon atoms of HOPG basel plane which fall on the hollow site of the adjacent layer below (see Fig. 3.10).

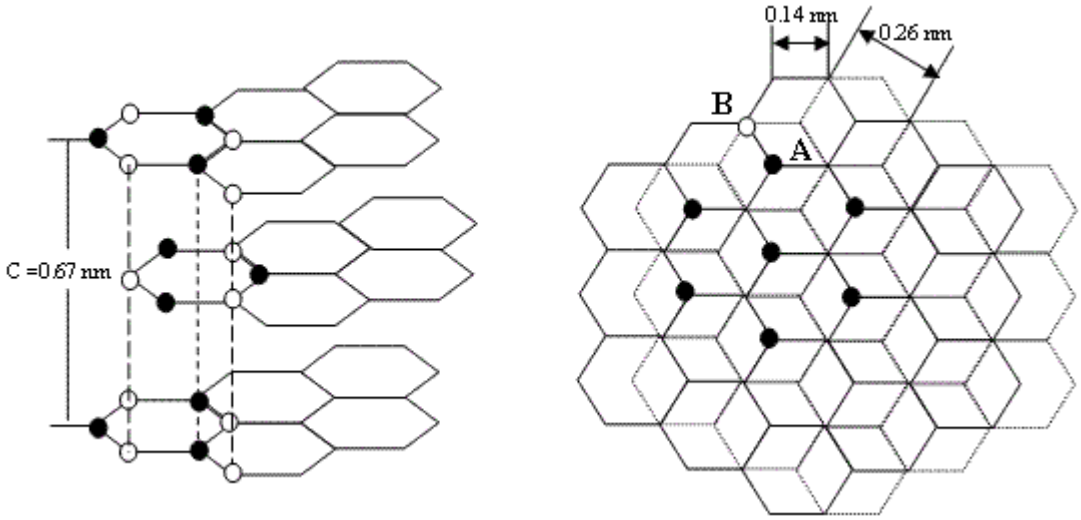

(a) **(b)**

Figure 3.10: (a) Crystallographic arrangement of HOPG, showing the stacking of atomic layers (ABAB) with the distance between two similar planes being ~0.67nm. (b) Top view of HOPG indicating the lattice positions of carbon atoms in adjacent graphitic layers (top layer: continuous line, bottom layer: dotted line). Overlapping carbon atoms are defined as B atoms (open circle) while the non-overlapping ones are defined as A atoms (filled circle). A carbons located above hollow sites (hexagonal center) in the adjacent layer are the sites detected by STM as indicated by the bright spots in Figure 3.11 (b). The spacing between A atoms is 2.46 Å.

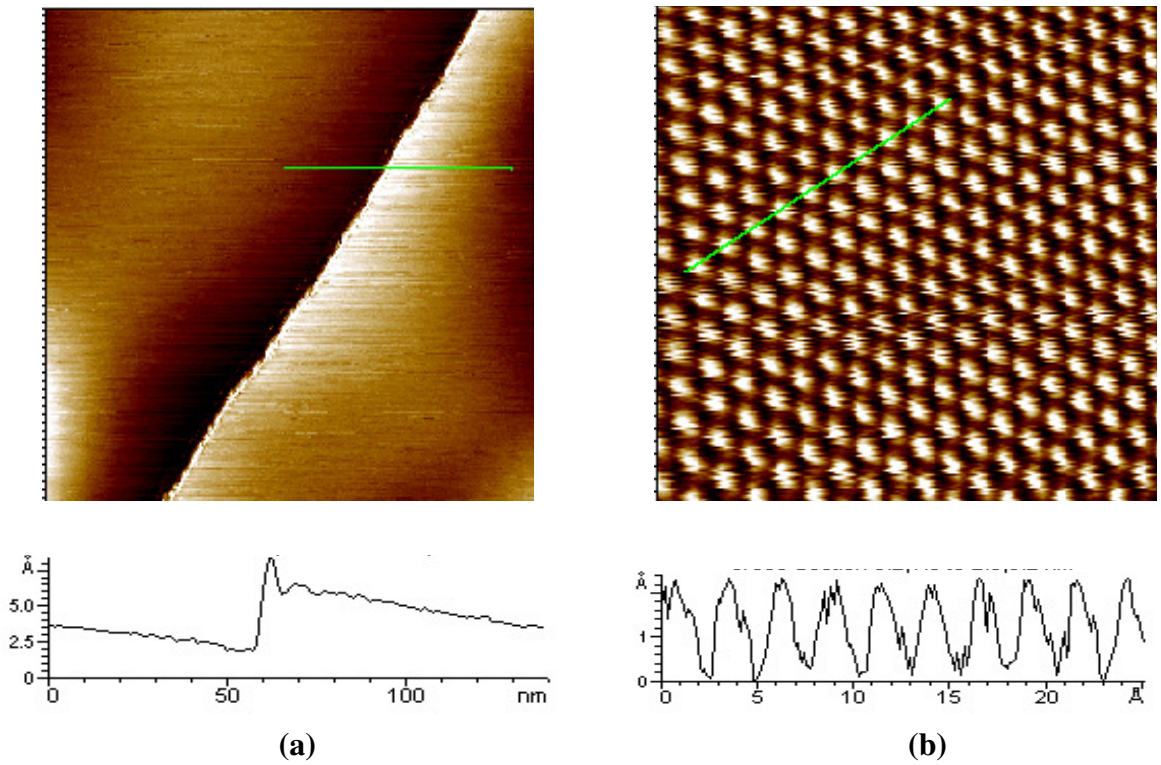

Figure 3.11: (a) 300 nm × 300 nm STM topographic image of a freshly cleaved HOPG surface showing a single atomic step of height ~3.5 Å. Tunneling conditions: V_{sample} = +100 mV, i_t=200 pA. (b) 4 nm × 4 nm STM topographic image showing the HOPG lattice. The bright dots represent A atoms in Figure 3.10b with a spacing of ~2.5 Å. Tunneling conditions: V_{sample} = +100 mV, i_t=200 pA.

3.4.2 Au (111) on Mica

High quality, atomically flat Au films are required as a substrate for the deposition of thiol self-assembled monolayers (see Section 3.4.3) Epitaxial Au(111) films were deposited on a mica surface by thermal evaporation of gold on mica under high vacuum [141]. Polycrystalline Au (99.999% purity) was purchased from Electronic Materials Technologies Pte Ltd. Mica sheets were purchased from Mica Fab. Inc. Freshly cleaved

mica sheets are introduced into an evaporator and were heated at constant temperature (550 °C) for 22 hours. The mica substrates were then cooled to 450 °C in 30 minutes and a 100 nm thick Au (111) film was deposited by thermal evaporation at a base pressure of ~2 × 10^{-5} Pa and a rate of ~1 Å/s. After deposition, the substrates are cooled to room temperature at a constant rate of ~1 °C /min.

STM imaging of Au(111) in liquid tetradecane (Aldrich, purity>98%) was performed at room temperature. After a freshly prepared Au(111) sample was taken out of the evaporator, a small drop of pure tetradecane was quickly placed on it. STM imaging was then performed. The Au(111) films show grains of Au with atomically flat terraces (Fig. 3.12(a)) with hexagonal atomic packing (Fig. 3.12c), which confirms the (111) orientation. The well known Au (22 × √3) reconstruction was observed on atomically flat terraces (see Fig. 3.12 b), in agreement with observations made in UHV environment [142, 143]. Molecular scale imaging, taken at smaller tunnel current, reveals the lamellar stripes of the tetradecane monolayer which has formed on the surface (Fig. 3.13a and b), in excellent agreement with the literature [144].

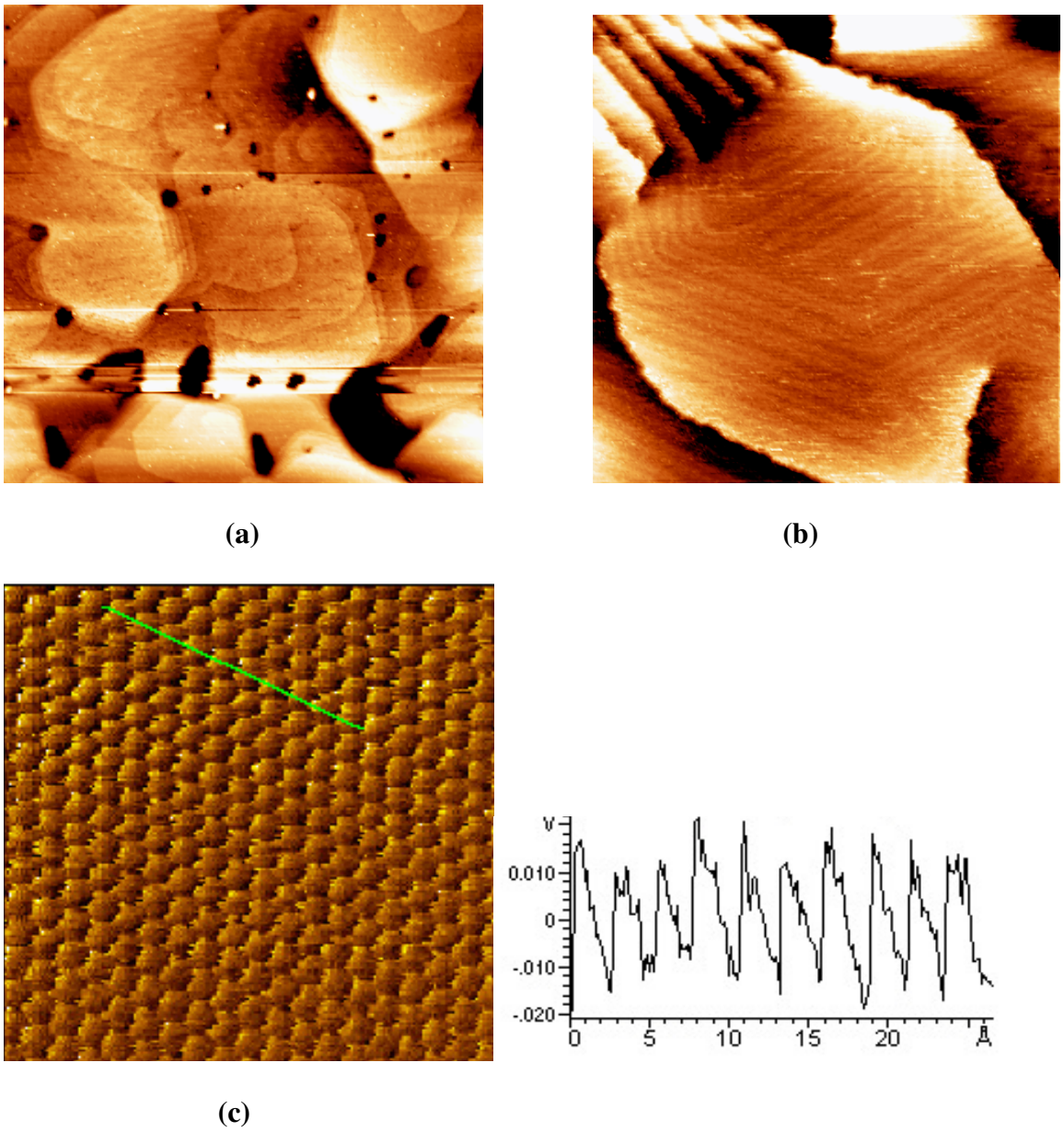

Figure 3.12: (a) Topographic STM image of a freshly prepared Au(111) surface (500 nm × 500 nm) taken in tetradecane. Tunneling conditions: V_{sample} = 400 mV, i_t=20pA. (b) Topographic STM image of Au(111) (100nm × 100nm) showing atomically flat surface with (22 × √3) known surface reconstruction. Tunneling conditions: V_{sample} = 400 mV, i_t=30 pA. (c) Friction mode AFM image of Au(111) surface (4.5 nm × 4.5 nm), taken in air, showing hexagonal packing of surface atoms with lattice spacing of ~2.7 Å.

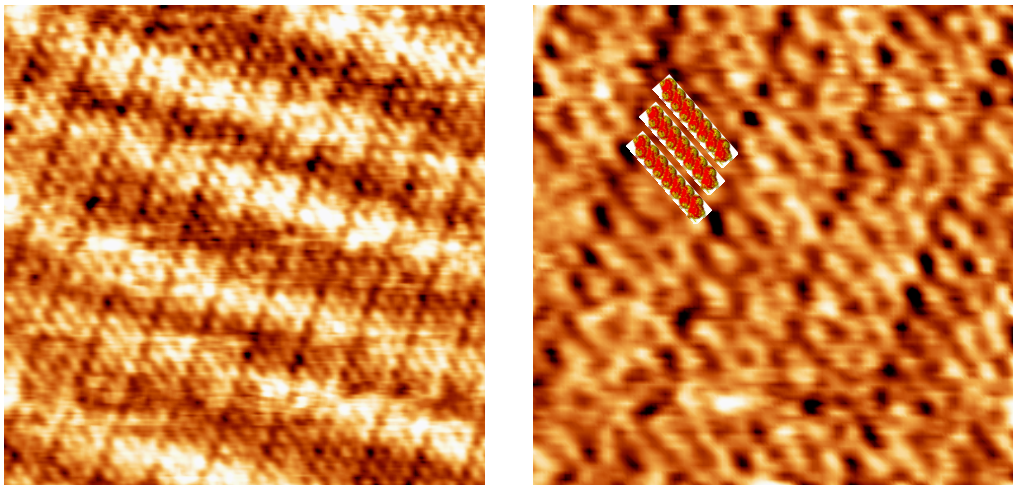

(a) **(b)**

Figure 3.13: (a) STM topographic image taken at the tetradecane/Au(111) interface (17nm × 17nm) revealing lamellar stripes of tetradecane molecules. Tunneling conditions: V_{sample} = 400mV, i_t=10pA. (b) STM topographic image of tetradecane molecular stripes (8nm × 8nm) showing individual tetradecane molecules within the stripes. Tunneling conditions: V_{sample} = 400mV, i_t=10pA.

3.4.3 Self-assembled Monolayer (SAM) on Au (111)

The SAM are used in this work as a "molecularly rough" surface for studying solvation forces and as a model system for measuring molecular conductivity relevant to research into single molecule electronics. A self-assembled monolayer (SAM) is a single layer of molecules on a solid surface which spontaneously forms on exposure to the molecules. A SAM can be prepared on a surface via various techniques such as molecular beam epitaxy, chemical vapor deposition or solution growth [145]. Growth of SAM from solutions of desired molecules is the simplest method of preparation. One of the most widely studied SAM is formed by various alkanethiols on Au(111) surface [145]. Alkanethiol molecules strongly adsorb on a Au surface via the S-Au bond (binding energy 85–145 kJ/mol) [146].

In this work n-decanethiol (labeled C10SH) SAM was formed on fresh Au (111) substrates by immersion in 1mM chloroform solutions for ~15 hours. The Au (111) substrates were immediately placed in freshly prepared n-decanethiol (C10SH) solution, just after removal from the evaporator. Decanethiol (Aldrich) was used as purchased. After SAM formation the samples were rinsed copiously with pure chloroform and dried under a N_2 gas stream immediately before introduction into the AFM liquid cell.

The structure of the prepared SAM was studied by STM in air and in liquid medium. The adsorption and growth of alkanethiol monolayer on a Au(111) surface takes place over a period of time. Initially alkanethiol molecules bind to the gold surface in a lying-down orientation where the alkyl chain of the molecules lies flat on the gold surface. As the concentration of the molecules increases on the surface, at some coverage the alkyl chains start lifting off the substrate and aligning normal to the surface, with one end of the molecule anchoring to the surface via the gold-sulfur bond [146]. Finally, the molecules form hexagonally packed structures in individual domains, with molecules occupying alternate voids on the underlying Au(111) surface which has a $(\sqrt{3}\times\sqrt{3})R30^{o}$ structure. The molecules are tilted ~30^{o} from the surface normal in the closed packed structure (see Fig. 3.14b). Fig. 3.14b shows an image of C10SH SAM formed on Au(111). The dark pits are known as etch pits and they form as a result of highly exothermic adsorption of the thiol molecules on the surface leading to a nonequilibrium surface rearrangement [147]. Studies have ruled out the chemical etching of the Au as a cause for the pit formation [148]. Fig 3.15 shows an image of the molecular arrangement

of the alkanethiols on Au(111). The c(4×2) lattice [149], which is know to be the thermodynamically most stable phase of the alkanethiol monolayers, is always observed. STM images showing the c(4×2) lattice reveals thiol molecules of two different contrasts [150, 151]. This was originally attributed to an alternation of the plane defined by the all-trans hydrocarbon backbones [152-154]. More recently, modeling of grazing incident X-ray diffraction (GIXD) profiles suggested that neighboring sulfur atoms pair to form a surface disulfide in addition to alternation of the hydrocarbon backbones, which was supported in a subsequent study that employed resonant sum-frequency generation [155, 156].

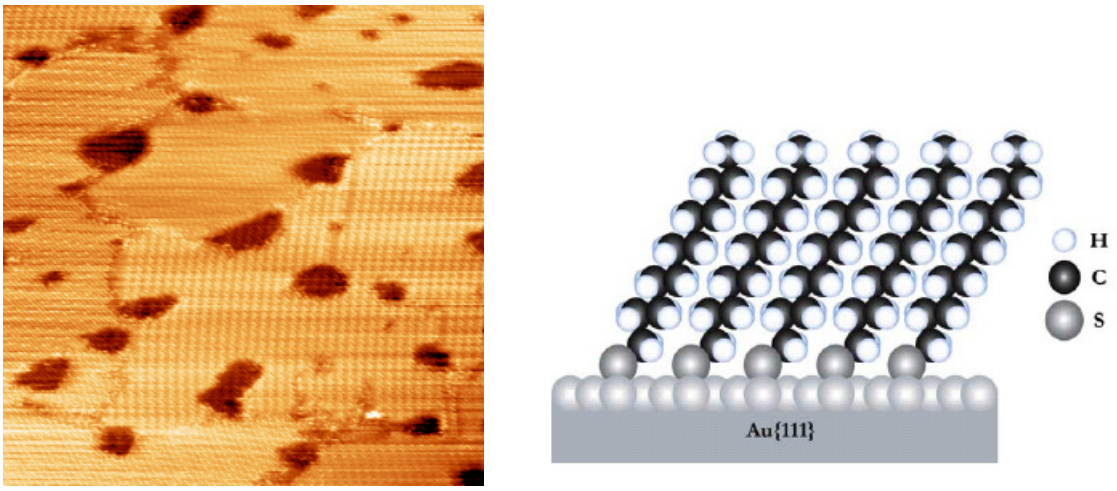

(a) **(b)**

Figure 3.14: (a) STM topographic image (50 nm × 50 nm) of n-decanethiol SAM on Au(111) showing a well packed structure with various domains, domain boundaries and etch pits. Tunneling conditions: V_{sample} = -1.0V, i_t=2 pA. (b) A schematic of the final configuration of an alkanethiol SAM on Au (111) taken from ref. [157].

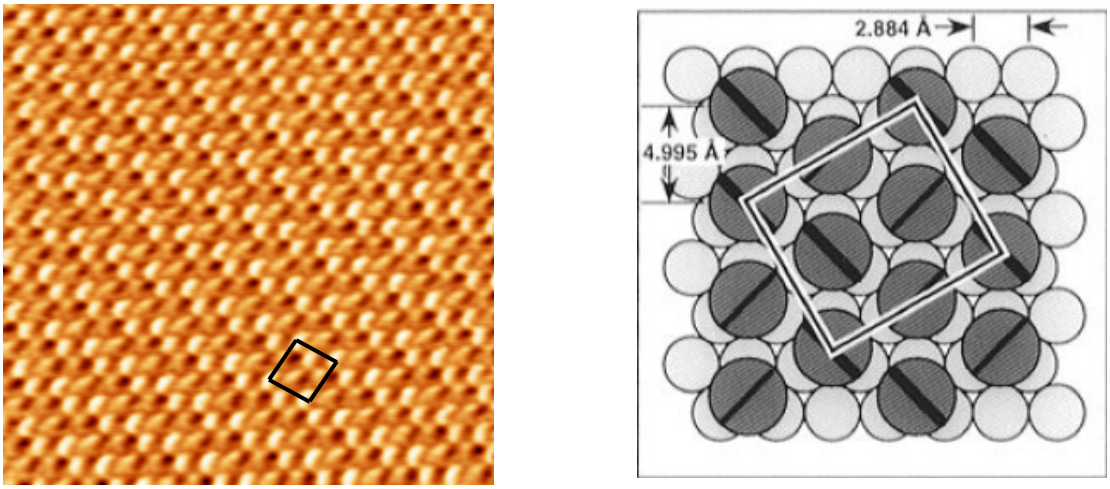

(a) **(b)**

Figure 3.15: STM topographic image (10 nm × 10 nm) of n-decanethiol SAM on Au(111) showing the well known c(4×2) phase. Tunneling conditions: V_{sample} = -1.0V, i_t=2 pA. Model showing the molecular packing in the c(4×2) phase taken from ref. [149].

3.4.4 Liquids

Most of the experiments in this work are performed in simple liquids (linear alkanes, branched alkanes and spherical molecules). All the liquids were purchased from Aldrich (purity ≥ 98 %) and were used without any further purification. These liquids are non-polar, non-crystalline, inert and geometrically well defined. These liquids have been extensively studied as model lubricants in a variety of approaches including AFM, SFA and theoretical modeling [3, 12, 15, 36, 39, 44-47, 60, 62, 64-66, 69-71, 77, 93-96, 100-103, 158-166].

Linear alkanes (C_nH_{2n+2}) above a critical chain length (n=14 at room temperature) form well ordered monolayers on HOPG and are ideal systems for understanding solvation forces and lubrication at the molecular scale. A linear alkane used extensively in this

work is hexadecane (Fig. 3.16a). Hexadecane has a chain length of ~2.36 nm [36] and a diameter of ~0.45 nm.

Squalane is a branched alkane (2,6,10,15,19,23 hexamethyltetracosane) with a linear backbone of 24 carbon atoms (Fig. 3.16b). The branching adds complexity to the shape of a linear alkane and has attracted attention to understand the effect of branching on the magnitude of solvation forces and changes in lubrication behaviour [69, 71, 74-76]. Indeed, squalane is often used as a model boundary layer lubricant. 2,2,4,4,6,8,8-Heptamethylnonane (HMN) is another branched alkane used in this work. HMN has much shorter backbone (9 carbon) compared with squalane (Fig. 3.16c). HMN was chosen because it's molecular weight is similar to hexadecane but the molecular shape is complex. Thus this molecule provides an interesting system for a direct comparison between a linear alkane and its branched isomer. As will be shown, molecular branching has profound consequences on the behaviour of the confined fluid.

Octamethylcyclotetrasiloxane (OMCTS) is used in our studies (Chapter 5) to understand fluid confinement of spherical molecules, particularly solvation effects in conducting AFM measurements of charge transport across a self-assembled monolayer [130]. OMCTS is a spherical and large molecule (Fig. 3.16d) and it is relatively easy to observe solvation layering in simple static mode AFM experiments. Further, OMCTS has been extensively studied using the SFA method so there is literature available for comparison with the AFM data [35].

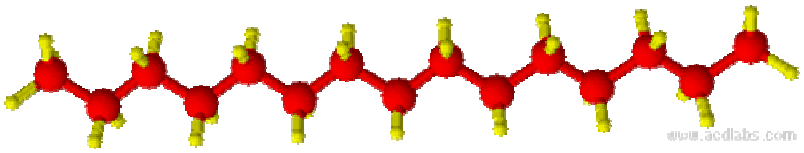

(a) Linear Alkane: Hexadecane (C16H34)

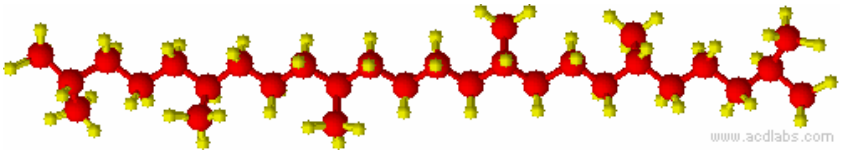

(b) Branched Alkane: 2,6,10,15,19,23-hexamethyltetracosane (Squalane:C30H62)

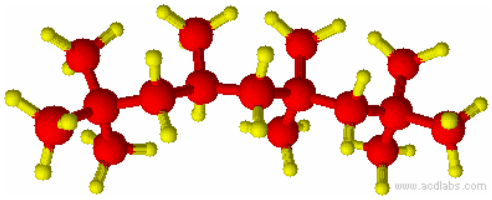

(c) Branched Alkane: 2,2,4,4,6,8,8-heptamethylnonane (HMN: C16H32)

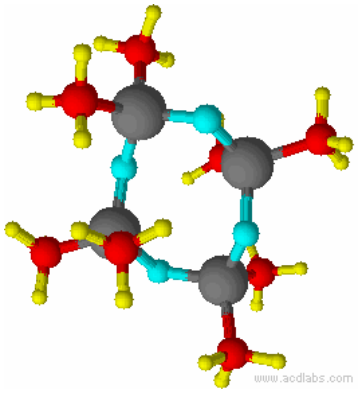

(d) Spherical Molecule: Octamethylcyclotetrasiloxane (OMCTS: $[SiO(CH_3)_2]_4$

Figure 3.16: Atomic configuration of the liquid molecules, (a) Hexadecane $C_{16}H_{32}$, (b) Squalane, $C_{30}H_{62}$, (c) 2,2,4,4,6,8,8-Heptamethylnonane or HMN, $C_{16}H_{32}$, (d) Octamethyltetrasiloxane of OMCTS $[SiO(CH_3)_2]$. The atomic labels are:

H C O Si

Chapter 4

Measurements on HOPG in Liquids

In this chapter the major emphasis is laid on understanding the behavior of liquids with different molecular shapes confined between a sharp conducting AFM tip and an atomically flat graphite (HOPG) surface. A comparative study is performed between linear and branched molecular liquids (Hexadecane, Squalane, and HMN). Images of the adsorbed liquid layer closest to the graphite surface (the monolayer) are also presented. Simultaneous measurement of current with force measurement is presented in each liquid and results are explained based on continuum mechanics models (as discussed in Chapter 2).

Such experimental study gives us detailed information of the squeeze-out mechanism of the liquid layer closest to the graphite surface as well as the mechanical interaction of the AFM probe with the graphite surface in the presence of various liquids. The molecular shape affects the ordering of molecules, which in turn affects the solvation forces and squeeze-out of the confined molecules. We find dramatic differences in solvation forces and squeeze-out behavior of confined molecules, which is strongly related to the state (i.e. ordered or disordered) of the confined liquid. We provide the first experimental evidence of ordering in a heavily branched alkane (squalane) monolayer in liquid, which agrees with recent simulations. We also find that ordered monolayers (e.g. squalane and hexadecane at room temperature) show solid-like behavior and exhibit similar lubrication properties, such as solvation forces and squeeze-out behavior. In contrast, disordered

monolayers, such as 2,2,4,4,6,8,8-heptamethylnonane at room temperature, do not show such behavior. This behavior is also observed in preliminary experiments on short-chain linear alkanes (dodecane and decane), which do not form ordered monolayers at room temperature. We show that this behavior is intimately related to the temperature and timescales of the experiment because the squeeze-out phenomena is thermally activated. Note that the data shown is representative of many individual force curves taken with at least five different tips for each experimental variation.

4.1 Solvation Forces measured using AFM in Liquids

Solvation forces are measured in pure liquids with different molecular architecture, namely linear alkanes (Hexadecane) and branched alkanes (Squalane and HMN) using gold coated Si_3N_4 cantilevers of spring constant ~ 0.38 or 0.76 N/m. In the force curves, the tip in contact with the HOPG is labeled as n=0, the monolayer as n=1, and subsequent solvation layers as n=2, 3, etc.

4.1.1 Hexadecane

Hexadecane has been widely studied in order to understand solvation forces in linear alkanes confined between two surfaces, using both AFM [167] and SFA [36]. AFM force measurements in hexadecane on graphite reveal oscillatory type solvation forces as the probe approaches close to the graphite surface. Around 5-8 layers are easily observed in the contact mode AFM force curve (Fig. 4.1). Hexadecane strongly adsorbs on the basel plane of graphite, forming a well ordered monolayer with lamellar structure [167]. These lamella can be imaged using AFM if the force is controlled within the first layer (n=1) or

using STM. Details of imaging are given in Section (4.2.1). The magnitudes of the forces agree well with previous experiments [167] and the solvation jump distance is 4.7±0.7 Å, corresponding to the molecules lying flat on the surface.

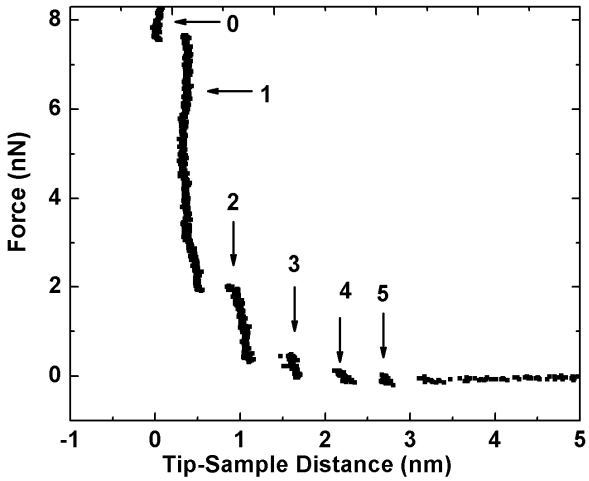

Figure 4.1: Force as a function of the tip-sample separation for hexadecane on HOPG. Solvation "jumps" are observed in the force curves and are labeled n=0 to 5, with n=0 being the tip in contact with the HOPG substrate. Data is taken at room temperature with a Au coated cantilever of spring constant 0.76 N/m and tip radius ~25 nm.

4.1.2 Squalane

Linear alkane molecules (e.g. hexadecane) reveal discrete solvation layering where molecules are arranged with their long axis parallel to the confining walls [36]. Studies on branched alkanes remain controversial. Early research suggested there was no layering for branched molecules under confinement [70, 168], the idea being that the side chain branches disrupt the ability of the molecules to form a layer. More recent studies showed that layering also occurs for branched molecules under confinement [93-95, 99-103]; however, the layering is weaker than linear alkanes due to the poorer in-plane ordering [93, 94, 99-102]. In the development of solvation layers in branched alkanes, the extent

of branching and symmetry of the molecules can play an important role. A recent simulation has revealed that in-plane ordering and branching can also dramatically affect how the confined fluid is squeezed out of the contact [99]. The branched alkane remains in a disordered or liquid-like state and the squeeze-out of the last layer is more sluggish, which leads to trapping of the molecules within the contact zone.

Our measurements also indicate strong solvation layering of squalane close to HOPG surface, with the molecules lying parallel to the surface. Fig. 4.2 shows force curves taken in squalane on HOPG. For squalane, ~5-6 jumps in the force curves were observed. The average solvation jump is 6.2±1.1 Å. Imaging of the layer closest to the graphite surface (n=1) has been obtained for the first time and is discussed in detail in Section 4.2.2.

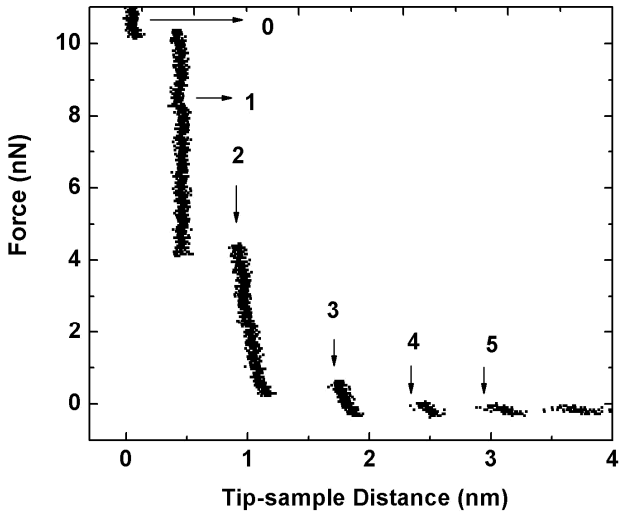

Figure 4.2: Data showing force as a function of the tip-sample separation for squalane on HOPG. Clear solvation jumps are observed indicated by n=1-5, where n=0 is the graphite surface. Data is taken at room temperature with a Au coated cantilever of spring constant 0.76 N/m and tip radius ~ 36 nm.

4.1.3 *2,2,4,4,6,8,8*-Heptamethylnonane (HMN)

HMN is a branched isomer of Hexadecane and Fig. 4.3 shows a representative force curve. Very weak solvation layering is observed and most of the force curves do not reveal sharp solvation jumps between layers. The slow transition between solvation layers more resembles that of yielding of a polymer monolayer [169] and small kinks (shown by unlabelled arrows) observed in the layer closest to the graphite surface (n=1), suggest a change in conformation of the confined molecules under compression. The separation between solvation layers is ill defined but appears to be 5.7±1.9 Å for the n=2 or 3 layer. This suggests that the molecules to a large extent are aligned parallel to the confining surfaces.

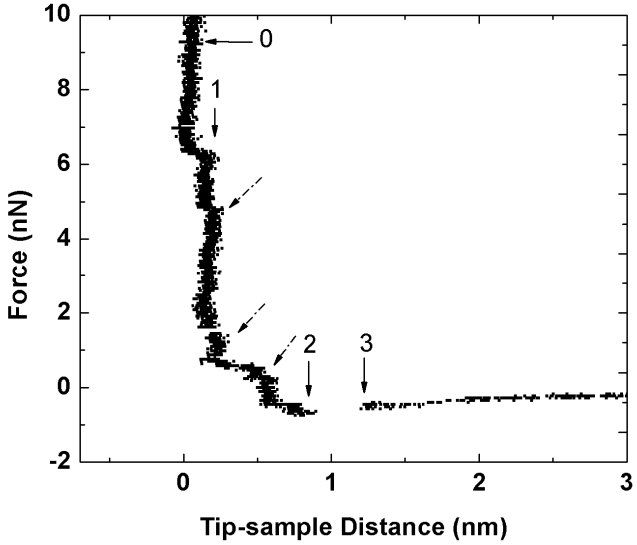

Figure 4.3: Data showing force as a function of the tip-sample separation for HMN on HOPG. HMN shows very weak jumps indicated by n=0-3 (n=0 is the graphite surface) with several kinks (shown with unlabelled arrows) in the force curve. Data is taken at room temperature with a Au coated cantilever of spring constant 0.76 N/m and tip radius ~ 19 nm.

4.2 Imaging of Adsorbed Molecules using STM and AFM

4.2.1 Hexadecane

Hexadecane molecules strongly adsorb on basel plane of graphite and form highly ordered lamellar structure which can be imaged using AFM or STM. AFM images reveal lamellar structure of the hexadecane monolayer when the value of the applied force is set within the bounds defined by n=1 in the force curve (see Fig. 4.4). When the imaging force is increased the monolayer is squeezed out, the tip contacts the HOPG (n=0) and an image of the graphite lattice is observed. The imaging of the HOPG provides additional proof that the hard wall contact has been reached and the assignment of D=0 is correct. Both the topographic and friction force signal reveal the lamellar structure of hexadecane (Fig. 4.5). STM can produce images with greater resolution (see Fig. 4.6) as contact mode AFM resolution degrades due to the finite tip-sample contact area.

It has been a debatable issue whether the multiple layers are "pre-existing" due to adsorption or appear purely due to the effect of confinement. There is no experimental evidence of imaging of more than one layer of short-chain alkane such as hexadecane. The only image of the n=2 layer has been reported for a very long-chain alkane n-$C_{36}H_{74}$ [170, 171]. Grazing incidence X-ray [172], differential scanning calorimetry (DSC) [173, 174], neutron scattering [173, 175, 176] and simulations [101, 177] indicate that 1 to 2 solvation layers occur on a free surface but the layering fades very rapidly with distance. The observation of 5-8 solvation layers in the AFM force curve thus strongly suggests that the solvation forces arise from a combination of mechanisms, with the most tightly

bound layers (n=1 to ~3) being due to adsorption and the outer layers (n≥3) arising from confinement of the fluid between the two solids. Note that the temperature also plays a key role. DSC and neutron diffraction experiments show that on graphite the ordered monolayer of a linear alkane melts significantly above the bulk melting temperature of the liquid [173, 175, 176]. Such data is taken on a free surface. The second layer (n=2) in such systems melts only just above the bulk. For hexadecane, the bulk melting temperature is <20 °C, which is well below the experimental temperatures of Fig. 4.4 (25 °C) whereas the monolayer melting temperature on HOPG is ~55 °C [174]. These considerations fit well to the conjecture that the AFM force curves are a mix of confinement and surface induced layering.

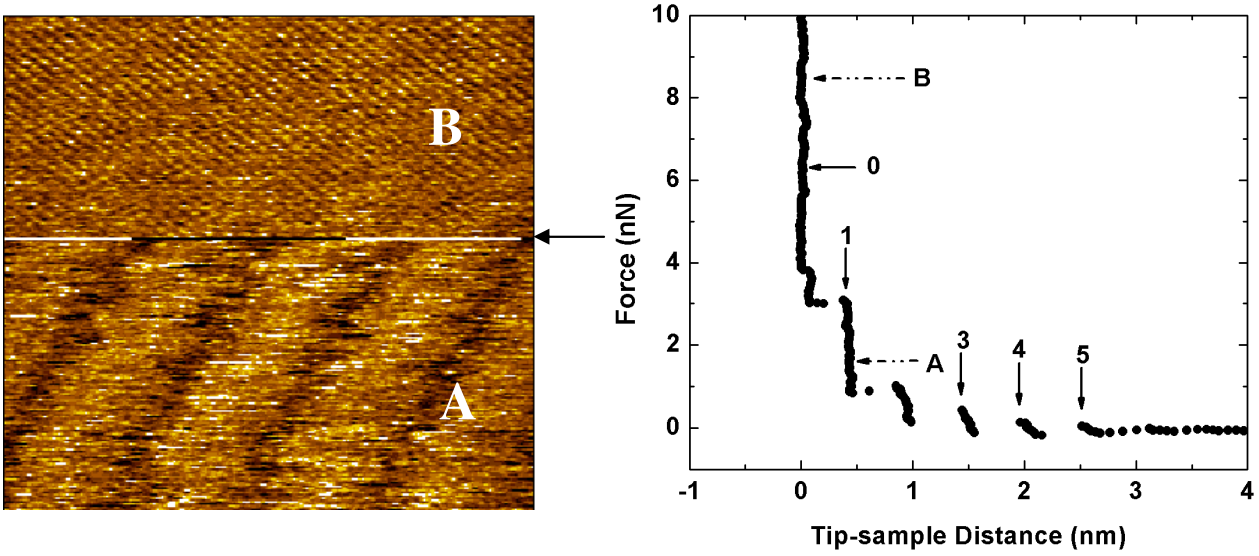

(a) **(b)**

Figure 4.4: (a) 12.5 nm × 12.5 nm contact mode AFM topographic image of hexadecane monolayer adsorbed on HOPG. (b) The corresponding force curve. In region A the imaging force is 1.7 nN and the monolayer (n=1) is imaged. At the position of the arrow, the force is increased to 8.5 nN and the graphite lattice (n=0) is now imaged in region B.

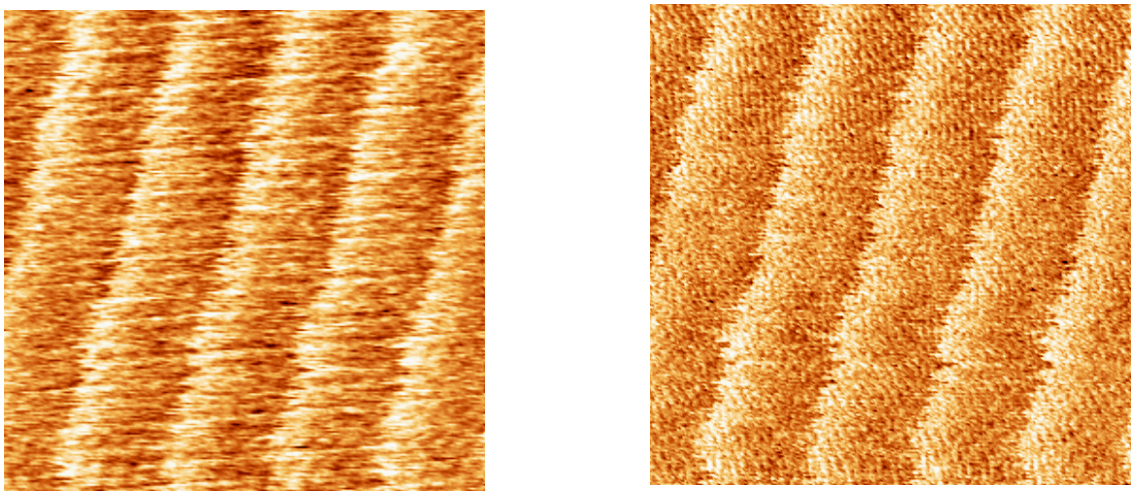

(a) **(b)**

Figure 4.5: 15 nm × 15 nm AFM image ((a) topographic image, (b) friction image) of the hexadecane monolayer (n=1) on graphite at room temperature using a super sharp tip (radius < 10nm). Spring constant = 0.15 N/m.

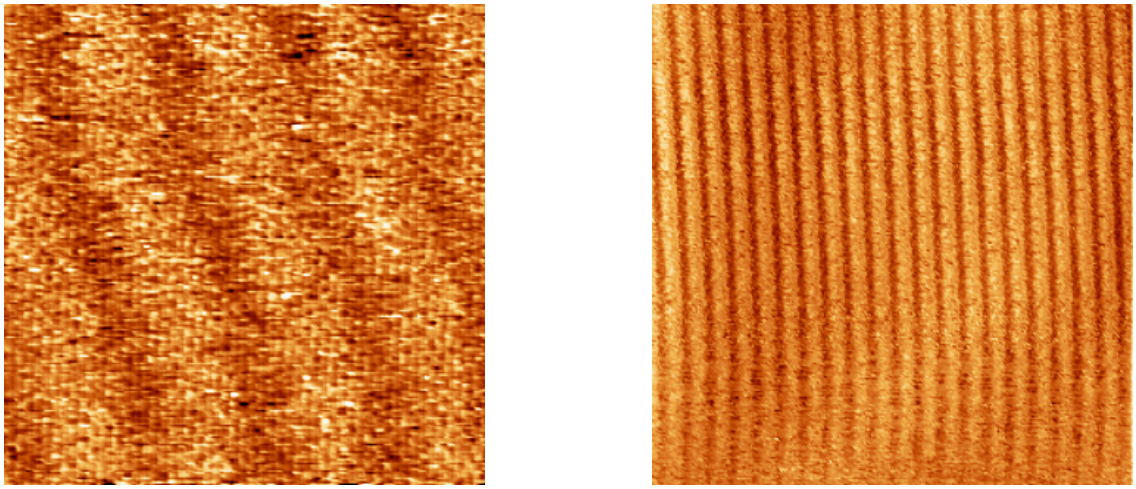

(a) **(b)**

Figure 4.6: STM images of hexadecane monolayer on HOPG. (a) 50 nm × 50 nm topographic image showing ordered lamellar. Tunneling Condition: V_{sample} = -800mV, i_t = 3 pA. (b) 9.5 nm × 9.5 nm topographic image showing atomic resolution. Tunneling Condition: V_{sample} = -1800 mV, i_t = 6 pA.

4.2.2 Squalane

The branched alkane squalane has been extensively studied to understand effect of branching on solvation forces and boundary lubrication. Recent measurements using the surface force apparatus (SFA) [71], atomic force microscopy [69], neutron and helium atom scattering and X-ray reflectivity have indicated strong layering of squalane close to various solid surfaces [74-76], with the molecules lying parallel to the surface. However, the structure of the adsorbed molecules remains unclear. Previous AFM experiments [69] could not obtain images of squalane on HOPG, presumably due to poor contrast from the very low frictional forces acting. Diffraction methods cannot probe the existence of ordering over small lengthscales. Indeed a recent simulation has shown that adsorbed squalane molecules can form ordered structure on a graphite surface [77] and explains why the structure is difficult to observe using diffraction techniques. Here we present the first experimental confirmation of surface ordering in a highly branched alkane (squalane) using STM imaging, which is in remarkable agreement with the simulations.

STM imaging of the squalane-graphite interface at 25 ^{o}C reveals ordered domains of lamellar structure formed by the squalane molecules (Fig 4.7 a). Molecular resolution images reveal individual squalane molecules aligned parallel to each other (Fig 4.7 b). The lamellar spacing is ~4.0 nm.

We observe a diffuse boundary between the squalane lamellar stripes. In comparison, the linear alkanes such as hexadecane and tetracosane (a molecule of similar chain length to squalane), show a very sharp lamellar boundary at room temperature (see Fig. 4.8 and ref.

[178]). A diffuse boundary could arise either from due to interdigitation of the molecules between lamellar or from increased molecular motion (vibration, rotation) arising from the side chains hindering a close packing of the molecules i.e. the side chains result in a lowering of the potential barriers to molecular motion. This interpretation is supported by images of linear alkanes at high temperature, showing that the lamellar boundary begins to blur as the temperature increases e.g. for tetracosane blurred boundaries occur at ~ 40 °C [178].

Another interesting difference with linear alkanes is the observation of two regions of different contrast within individual squalane molecules (Fig 4.7b) which could arise due to the backbone of the molecule twisting out of the plane over part of it's length. This probably arises from the molecule trying to configure to the closest packing condition.

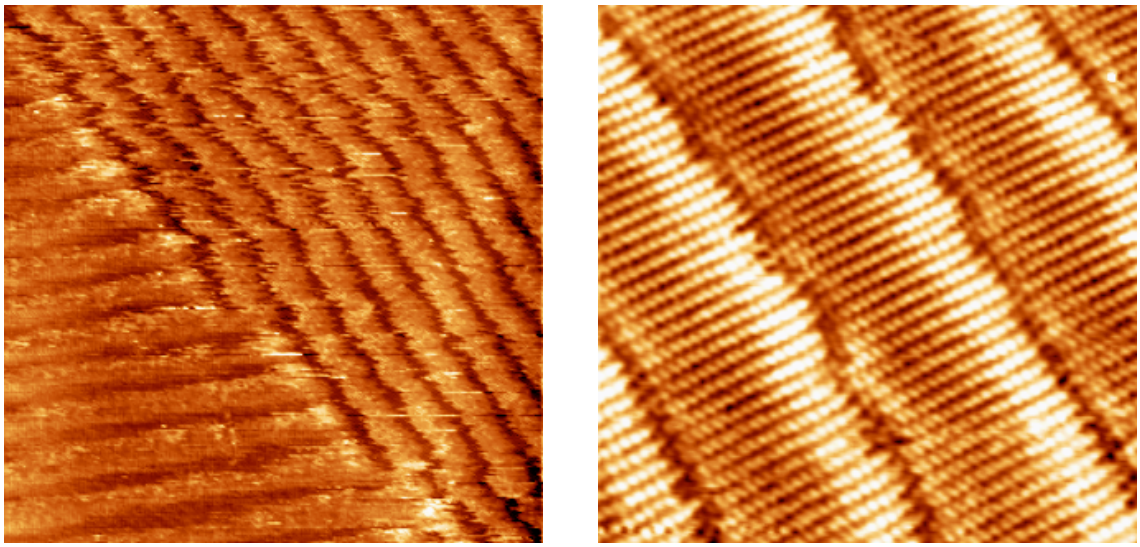

(a) **(b)**

Figure 4.7 (a): 60 nm x 60 nm STM topographic image of squalane molecules adsorbed on HOPG revealing ordered domains. Tunneling Condition: V_{sample} = 600 mV (sample positive), i_t = 5 pA. (b): 13 nm x 13 nm STM topographic image of squalane molecules adsorbed on HOPG revealing molecular resolution. Tunneling Condition: V_{sample} =1000 mV (sample positive), i_t = 12 pA. Imaging is performed at room temperature.

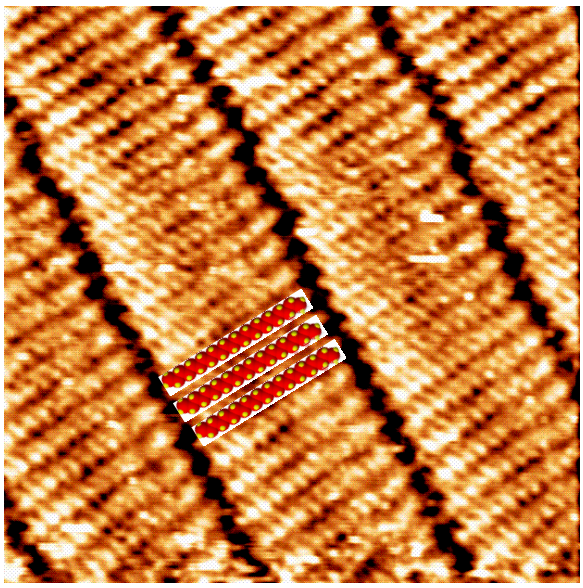

Figure 4.8: 10 nm × 10 nm STM topographic image of a tetracosane (n-C24H50) monolayer adsorbed on HOPG, obtained at room temperature. The sample is prepared by dissolving tetracosane approx 1.0 mg in ~1.0 ml phenyloctane. Tunneling Condition: V_{sample} =1200 mV (sample negative), i_t = 2 pA. The images reveal sharp boundary between individual lamellar stripes.

4.2.3 HMN

The data obtained in HMN shows that weak solvation layering occurs in HMN. AFM and STM imaging of these molecules close to the HOPG surface did not reveal any "ordered layer" suggesting that the molecules are in disordered state. Imaging using AFM even at very low forces (~1-2nN) reveals the underlying HOPG lattice, suggesting that the molecules are weakly adsorbed and can be easily dislodged from within the contact zone when lateral forces are applied. Indeed, at low forces HMN molecules are probably still trapped within some part of the contact zone while another part of the tip apex contacts the surface, giving rise to the HOPG image. This conclusion can be made based on the

current vs. force curves of the HMN on HOPG system and is fully discussed in the next section.

4.3 Simultaneous Force and Conductivity Measurements

In this section results obtained from simultaneous measurement of the conductivity and forces using conducting AFM (C-AFM) across various liquids (hexadecane, squalane and HMN) confined between a gold coated AFM tip and a graphite surface are presented. The current flow with a fixed bias voltage is measured simultaneously with the force curve acquisition. The data obtained is compared with continuum mechanics models to describe the mechanics of the confined monolayer as well as the interaction of the Au coated probe with the underlying HOPG surface.

4.3.1 Hexadecane on HOPG

This section describes the data obtained using C-AFM in hexadecane. This case is discussed in detail as the basic outcomes can be extended to encompass the data for other liquids. Firstly the tip-HOPG contact (n=0) is investigated. This is important as it establishes that the elastic continuum mechanics model is valid for these systems. Next, the tunneling current in the n=1 and n=2 solvation layers is studied as a function of the applied force, which yields details of the molecular behavior of the confined material.

4.3.1.1 Conduction through the Au-HOPG Contact

We begin an analysis of the force curves by first considering the tip-graphite contact (the region n=0 in Fig. 4.1). This serves two purposes, namely, a) to give confidence in the

application of elastic models to describe the mechanical response, and b) to verify that the tip has indeed pushed through the hexadecane and is in contact with the substrate. Fig. 4.9 shows the raw C-AFM force curve for a Au coated tip contacting HOPG in hexadecane. On approach (Fig. 4.9a) the current is less than ~10 nA (fixed bias = 0.6 V) until the last solvation layer n=1 is squeezed from the tip-sample gap. Once this occurs the tip forms a mechanical contact with the HOPG (n=0) and the current becomes very large (>200 nA).

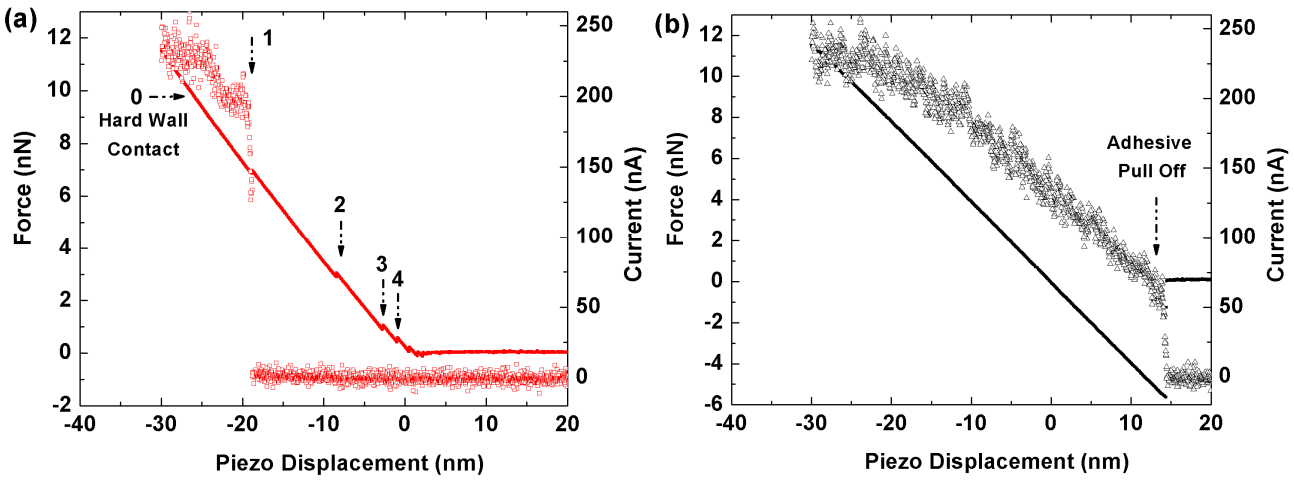

Figure 4.9: Raw data showing simultaneously measured force (solid line) and current in hexadecane. (a) Approach, the small jumps show the tip squeezing out solvation layers. A sharp rise in current is observed (circles) when the tip contacts the graphite surface above the force required to squeeze-out the last hexadecane monolayer. (b) Retract, a finite current is measured (triangles) during the pull off curve down to the adhesive minima.

The current flow is also monitored as the tip is pulled off the surface (Fig. 4.9b). Note that a finite current is measured over the entire pull-off force curve, including the adhesive minima. This is an important observation because wear or contamination of the

metal coating at the tip apex is a serious problem in C-AFM [107]. A previous study has reported forces of order ~1000 nN to break through supposed "solvation layers" of hexadecane on HOPG using C-AFM [163]. Given our data, it is not realistic that the multiple current "jumps" observed in reference [163] are associated with solvation layering. We believe the underlying reason for this error is wear or contamination of the tip apex i.e. very large forces are required in their study to achieve an initial current flow.

We are confident that the tip is in contact with the HOPG in the region n=0 because,

a) The HOPG lattice can be imaged. During AFM imaging, the lamellar structure of the hexadecane monolayer (n=1) can be imaged at low force (Fig. 4.4a) but disappears and the HOPG lattice appears when the imaging force becomes sufficiently high (a few nN).

b) The contact resistance of the HOPG can be measured. We do not observe any noticeable difference in contact resistance values measured in air or in liquid environment at similar applied loads. Current-voltage (I-V) curves were performed (Fig. 4.10) showing linear I-V with a contact resistance near zero bias of 110±40 MΩ per nm^2 (in air), which is in agreement with previous studies for metal-HOPG contacts [107, 179-182]. The contact resistance in hexadecane was found to be 95±47 MΩ per nm^2. The large error values arise from the use of different tips. The contact resistance was always at least 20 times smaller for the tip-graphite contact (n=0) compared with the first layer (n=1) for a given tip.

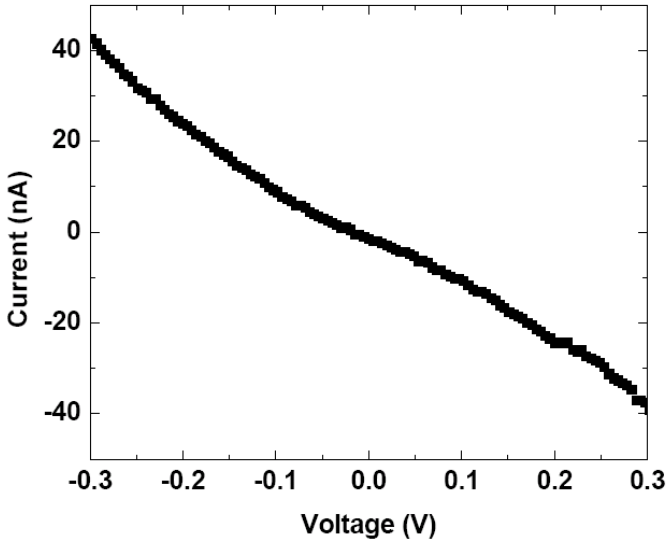

Figure 4.10: I-V obtained with a Au tip in contact with HOPG in air at an applied load of ~8 nN. The tip radius is ~25 nm.

To directly compare with analytical models, it is more convenient to re-plot the current as a function of force, as shown in Fig. 4.11, because the current is proportional to the contact area. In this example, the tip pushes through the n=1 layer at ~ 7.0 nN on approach. The pull off curve is more instructive because forces are measured over a large range, down to the adhesion minima (in this example, F_c ~ 6.0 nN). The pull off curve thus provides a more accurate comparison with models of the point contact mechanics, and in Fig. 4.11 the calculated contact area is found from a Maugis-Dugdale fit (blue solid curve).

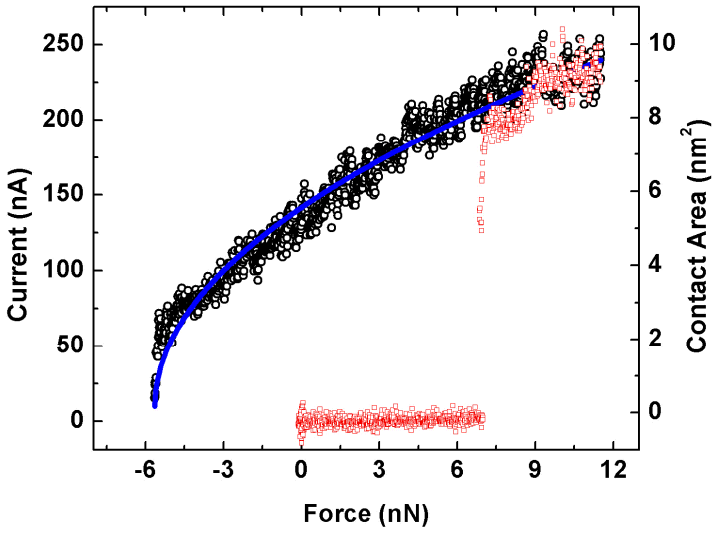

Figure 4.11: Current vs. force curve for the tip in contact with the graphite (n=0). On approach (circle) the tip pushes through the solvation layers and contacts graphite surface at ~7 nN. The tip is then pulled off the surface (black). The variation in current is fitted with the Maugis-Dugdale model (solid curve) to give the contact area. Data is taken at room temperature with a Au coated cantilever of spring constant 0.76 N/m and tip radius ~25 nm.

We now describe the tip-HOPG contact mechanics model in more detail. In all cases we consider, the measured current is proportional to area. Thus a plot of current versus force, as in Fig. 4.10, shows the *relative* change in area with applied force, which in turn can be compared with contact area calculated from the applied force coupled with a suitable mechanical model of the point contact [107]. We apply the Maugis-Dugdale (MD) model for an elastic contact (see Section 2.4.4). As shown below, this approach appears valid. In the MD model the contact radius a can be written (see Eqn. 2.16) as:

$$a = a_0 \left(\frac{\alpha + \sqrt{1 - F_a / F_c}}{1 + \alpha} \right)^{2/3} \tag{4.1}$$

where a_o is the contact radius at zero normal force, F_a is the applied normal force and F_c is the pull off force.

Here α =1 corresponds to the Johnson-Kendall-Roberts (JKR) model for an adhesive contact and α = 0 corresponds to the Derjaguin-Muller-Toporov (DMT) model of a hard contact. Eqn. 4.1 provides a good fit to the current vs. force data (solid line, Fig. 4.11) with a value of α = 0.073 i.e. close to the DMT model. Thus the *relative* change in contact area is well described for the hexadecane-HOPG contact by an elastic continuum model.

The *absolute* value of the contact area is more difficult to obtain. Values can be found from either fitting mechanical models, as above, or from the current measurement. To obtain contact area from a current measurement requires the detailed current transport mechanism to be known. In the case of the tip-HOPG contact, the contact radius can be assumed to be much smaller than the mean free path of electrons (l), and the Sharvin equation for the resistance (R_{Sh}) can be applied (see Section 2.5.1),

$$R_{sh} = \frac{4\rho l}{3\pi a^2} \tag{4.2}$$

where ρ is the mean resistivity. As the current scales linearly with area πa^2 we need only compute the area at one data point. The calculated value of "electrical" contact area for the data of Fig. 4.11 at zero applied force is ~ 5.8 nm^2, using ρ ~ 5000 μΩ.m [140] and l =10 nm.

How does the "electrical" area compare with the corresponding "mechanical" area? For simplicity we calculate mechanical area using the DMT model as in this case all the model parameters are known experimentally. Contact area calculated from the DMT model (α=0) gives values only ~20% different than those found using the full MD model. The contact radius in the DMT model is (see Section 2.4.2),

$$a = \left\{ \frac{3r}{4K} \left(F_a + F_c \right) \right\}^{1/3} \tag{4.3}$$

where R is the tip radius of curvature and K is the effective modulus,

$$K^{-1} = \frac{3}{4} \left(\frac{1-\nu_1^2}{E_1} + \frac{1-\nu_2^2}{E_2} \right) \tag{4.4}$$

with E being Young's modulus, ν the Poisson ratio and subscripts 1,2 referring to gold and graphite respectively. Using ν_1=0.33, ν_2=0.43, E_1=78 GPa and E_2=36.5 GPa (for graphite along the c-axis) results in K= 39.5 GPa. For the data of Fig. 4.11 we measure r=25 nm, giving the calculated "mechanical" contact area at zero force as 7.4 nm^2.

The electrical and mechanical estimates of the contact area (5.8 nm^2 and 7.4 nm^2 respectively) are very close in the example given. However, this is probably fortuitous. The uncertainties are large (specifically ρ, l in Eqn. 4.2 and K in Eqn. 4.3) and do not allow a strong statement to be made as to which approach, electrical or mechanical, provides a better measure of absolute contact area. The use of different tips is also a

source of uncertainty. All that can be stated is that *qualitatively* the electrical and mechanical approaches give the same order of magnitude in contact area. Nevertheless, a consideration of the errors involved leads to the conclusion that the mechanical model is possibly the best. The error in R is small as we find that for Au coated tips the SEM images invariably show a smooth and well defined tip curvature. The major uncertainty for the "mechanical" contact area lies in the value of modulus K. However, even if K varies between that of pure gold and pure graphite, the calculated contact area only changes by less than a factor of ~2. In contrast, in the electrical model, the estimated mean free path and hence contact area could vary by an order of magnitude.

The main result of this section is that simple elastic models of the point contact are useful to describe the tip-HOPG contact in liquid even for very small contact areas (1-10 nm^2).

4.3.1.2 Conduction through Hexadecane Solvation Layers

We now consider the solvation layers and in particular the monolayer (n=1). Fig 4.12 shows raw data for simultaneous current vs. force measurements taken for hexadecane on HOPG using a Au coated probe. Several jumps (labeled n=1 to 5) are observed in the force curve as the tip approaches the substrate, corresponding to layering of the confined hexadecane. The simultaneously measured current flow is shown for the first hexadecane layer (Fig. 4.12a) and within the second layer (Fig. 4.12b). Separate plots are required as the current is orders of magnitude different between layers. This is expected as the current flow occurs through tunneling. For the second layer the current is <1.0 pA and a lock-in amplifier was used to extract the signal from the noise (a 75 mV AC pk-pk sine

wave modulation at 87 Hz was superimposed on the applied DC voltage). No current could be observed within the third layer because the tip-substrate separation is too large and the tip-substrate tunnel current is negligibly small. I-V curves show that the contact resistance (i.e. near V=0V) within the layer varies from (0.5-1.25 GΩ).

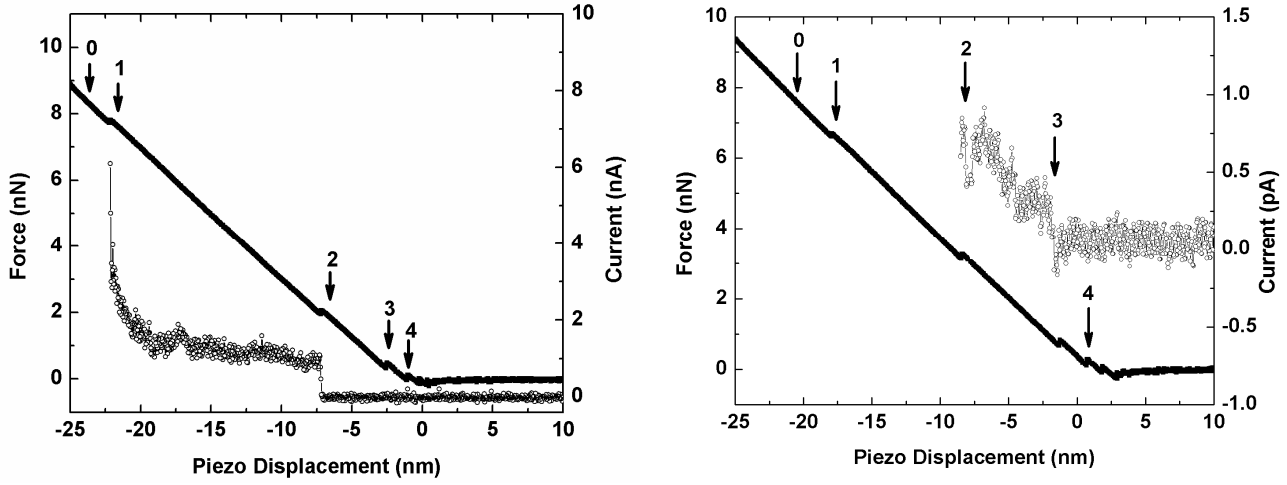

(a) **(b)**

Figure 4.12: Simultaneous force (solid line) and current (circle) measurements for hexadecane on HOPG as a function of displacement of the piezoelectric actuator. Current is shown for (a) the n=1 layer; (b) n=2 layers. The tip is approaching the surface. Solvation "jumps" are observed in both the force and current curves and are labeled n=0 to 4, with n=0 being the tip in contact with the HOPG substrate. Data is taken at room temperature with a Au coated cantilever of spring constant 0.76 N/m and tip radius ~ 25 nm.

In all experiments at room temperature there is a sudden, discontinuous jump in the current as the tip transverses a solvation layer (Fig. 4.12). More interesting is the presence of two distinct current regions within the first layer (Fig. 12a), with a very sharp increase in current just before the tip punches through the hexadecane monolayer to

contact the underlying HOPG substrate. This intriguing behaviour was observed in almost all of the force curves and is discussed in detail below.

Having verified the elastic model approach is reasonable for the HOPG contact, we now apply it to the first hexadecane layer (n=1). The variation arises from the use of different tips. The approach force curve (Fig. 4.12a) is plotted as a current vs. force curve in Fig. 4.13. The two distinct regions we label the "fast" current region, designating the very rapid change in current at high force, and the "slow" current region occurring at lower forces, where the current rises very gradually with force. The DMT model is used and is a very good description of the mechanical response of the monolayer (see inset Fig. 4.13). The estimated contact area falls to less than 0.7 nm^2 just at the adhesive minima (typically -2 to -3 nN). An effective modulus of K=39.5 GPa is used as before because although the modulus of the hexadecane film is unknown, the deformation of the monolayer is negligible based on the very small change in both current and force, as explained below.

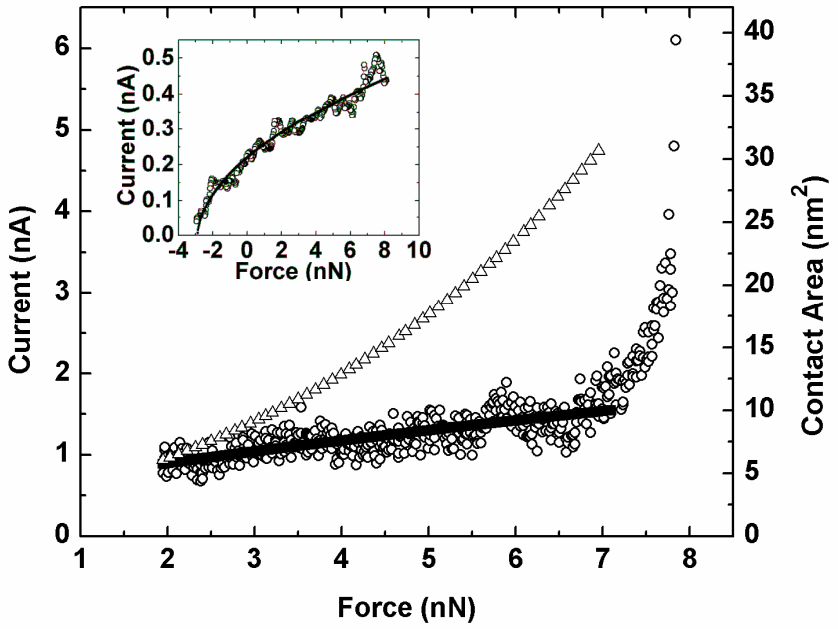

Figure 4.13: Current vs. force curve on approach for the tip in contact with the first hexadecane layer (n=1). There are distinct "slow current" and "fast current" regions. A DMT profile is superimposed (solid curve) to estimate the mechanical contact area. The curve (Δ) shows the expected current variation if the confined molecules were assumed to undergo deformation upon significant compression which is clearly not the case. The inset shows data, taken with a different tip, as the tip is pulled off the first layer. The variation of current follows DMT mechanics with very small contact area (~0.7 nm^2) at the adhesive minima (-2.9 nN).

The current flow across the hexadecane layer occurs by tunneling [115]. The current at constant voltage is proportional to the contact area, allowing *relative* changes to be monitored straightforwardly. However, the *absolute* value of the contact area cannot be accurately evaluated at present from the current measurement (see Section 4.3.1.3) because no theoretical model is available which gives accurate numerical values of the tunnel current magnitude [113] inclusive of the tunneling contribution arising from the mixing of the electrode and molecule energy level (see Section 2.5.2). Thus the

mechanical modeling, as in the n=0 case, again proves the most reliable for evaluating the *absolute* contact area.

In the slow varying current region the DMT model provides a good fit and the contact area increases from ~5.8nm^2 at 2nN to ~10.2 nm^2 at 7nN. The fact that the current follows the DMT profile suggests that the small increase in current in this region arises chiefly from an increase in contact area. The alternative explanation is that the tip-substrate distance is decreasing with increasing load. However, this is not the case as a calculation using the DMT model shows the deformation of the entire tip-monolayer-HOPG system is 0.13 nm at the maximum force of 7 nN. The tunnel current is exponentially sensitive to the tip-surface separation and a decrease of 0.13 nm in the tip-surface separation would lead to a current increase of ~10 fold (see Section 2.5.2, Eqn. 2.23) as the force changes from 2 to 7 nN. This is clearly not the case in the slow current region and we conclude that the hexadecane is rigid enough to maintain the tunnel gap and the principal deformation under load is occurring in the softest material, namely the HOPG substrate. The negligible deformation of the hexadecane monolayer in comparison to the deformation of the tip or HOPG is the reason the modulus of the tip-HOPG contact is used (E=39.5 GPa) in our calculations. Another way to highlight the rigidity of the n=1 layer is to assume that the hexadecane molecules are more compliant than either gold or HOPG. If this were the case, the current variation will be dependent on the deformation in the confined monolayer in addition to changes in contact area. Deformation of the monolayer leads to an exponential increase in current because the tip-to-substrate distance will decrease with increasing load. The resulting variation in tunnel current as a function of force (F) for the DMT or Hertz model is [183],

$$i \propto (F + F_c)^{2/3} * \exp\left((F + F_c)^{2/3} \right) \tag{4.5}$$

This current variation is shown qualitatively as a curve (Δ) in Fig 4.13 and clearly does not describe the data.

In the fast current region, just before the tip punches through to the substrate, the current rises by a factor of ~4. This behaviour cannot be explained by the fitting of a continuum mechanics model, at least under the assumption that current flow is proportional to area, and there is no corresponding change observed in the applied force curve. Thus we rule out that the contact area suddenly increases by elastic deformation of the substrate or tip. Plastic deformation of the substrate or tip cannot occur at the observed pressure (~1.0 GPa), which is smaller than the yield stress for materials of nanoscale volume [184]. It is important to note here that although the yield stress for bulk metals is ~0.01 to 0.1 GPa, the material in our experiments has only nanoscale volume which results in yield stresses close to the theoretical limit, as shown in previous experiments e.g. ~2 to 6 GPa for Au [185]. An alternative explanation is that a hole nucleates in the monolayer, with the removal of one or several molecules, prior to the complete squeezing out of the hexadecane. The tip would penetrate into the hole giving an increased tunnel current. This situation appears unlikely as no change in current is observed when the tip is continuously scanned across the surface (by 50 nm) whilst controlling at a force that lies within the fast current region (Fig. 4.14). In this figure, a normal force curve would show as a slice along the y axis. Another factor against tip penetration is that if one molecule is removed from the gap then the remaining molecules will be squeezed out extremely

rapidly as the elastic shear forces that result from such an event drive the system to a new equilibrium, as found theoretically [186]. In our experiments nucleation would describe the rapid transition *between* layers, not the fast current rise of Fig. 4.13.

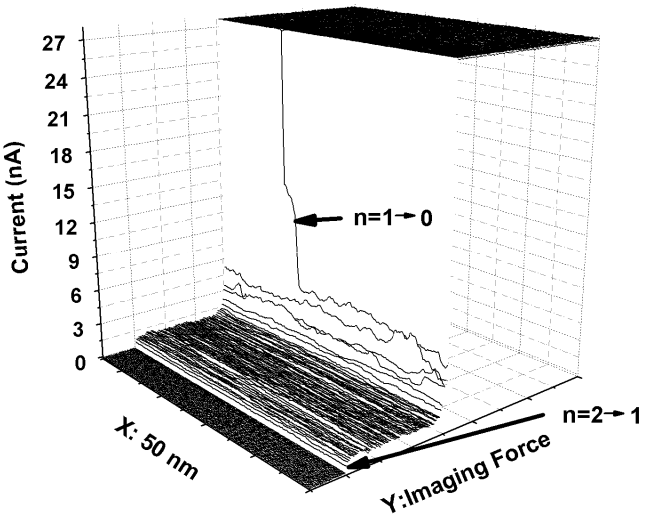

Figure 4.14: Data showing variation of current (z axis) measured through the tip while scanning a 50 nm × 50 nm HOPG area in hexadecane. The force (y axis) was slowly increased during imaging. There are two clear steps observed as the force set point was varied, causing n=2→1 and n=1→0 layer transitions.

Our favoured model is that the molecules remain under the tip apex in the fast current region. Prior to the complete n=1→0 layer transition there is a rearrangement of molecules under the tip apex leading to a smaller tunnel gap. The conformation change within the hexadecane monolayer results in either a thinner layer or the possibility that gold atoms from the tip interdigitate between the hexadecane molecules. This hypothesis ties in with the observation in AFM measurements that the solvation "jump" closest to the surface (n=1→0) is a smaller displacement than other jumps [187]. We also observe this behaviour and Table 4.1 shows the average distance the tip "jumps" between layers. The outer "jump" distances (n≥2) all have similar value (4.5 Å) whereas the n=1→0

transition is 1Å smaller, a difference corresponding very closely to the expected change in tip-substrate separation (0.8Å) calculated for the observed increase in tunnel current of ×4. The hypothesis is also supported by molecular dynamics computer simulations of liquid Xe confined between two solid walls [165] which show that Xe can undergo a phase transformation, leading to a smaller wall-wall separation, prior to a n=2→1 layer transition. The same group has found similar behavior for the squeeze-out of n-butane [99].

Table 4.1: A comparison of the distance the tip "jumps" as a layer transition occurs. The distance is considerably smaller for the jump from the first layer to the HOPG (n=1→0) compared with layers further from the surface (n≥2).

Reference	Transition n =1→0	Transition n ≥ 2	Notes
This work	3.5 ± 0.5 Å	4.5 ± 0.4 Å	Hexadecane on HOPG
Franz *et al* [188]	3 to 4 Å	4 to 5 Å	Linear chain alcohols on HOPG
Christenson *et al* [36]	-	4 to 5 Å	SFA of alkanes on mica

An alternative explanation which we cannot exclude is that the sudden rise in current is due to pressure induced resonant tunneling. The energy levels of the hexadecane may shift due to conformation changes induced by the applied pressure such that tunneling is enhanced as a molecular energy level moves close to the Fermi level. This appears unlikely given that the HOMO-LUMO gap is very large (~8 eV), there are no states within the gap, and most data for alkane systems show current flow results from non-resonant tunneling [113, 115].

The contact area in the fast current region is found using the DMT model, from which the pressure required to squeeze-out the n=1 layer can be found. The pressure is not uniform across the contact zone, being much higher in the centre e.g. for the DMT model the centre pressure is a factor of 3/2 higher than the average pressure. Thus the conformation change of the confined hexadecane prior to squeeze-out would be expected to occur at the tip apex. For Fig. 4.13 we find that just before the monolayer is removed the contact area is ~10.7 nm^2 giving the average pressure to squeeze-out the layer as ~0.73 GPa, with a pressure at the tip apex of ~1.1 GPa.

Not surprisingly, the observed squeeze-out pressure changes due to experimental variation (e.g. approach speed, experimental error, differing molecular arrangements at the contact) and the use of different tips. Thus a statistical value of the squeeze-out pressure is preferred. Fig. 4.15a shows several representative curves detailing the n=1→0 transition curves. The curves essentially reveal reproducible behavior in all cases except that the force needed for the layer squeeze-out varies by a factor of ≤2. Further, the squeeze-out process itself is thermally activated [104] and thus the force needed to remove a layer varies statistically i.e. at a given force the tip will attempt many times to overcome the energy barrier for hole nucleation to initiate squeeze-out and at finite temperature there is a (Boltzmann weighted) probability that the nucleation will occur. This effect has been shown explicably by Butt *et al* [189] for the squeeze-out of the adsorbed lipid layers. Fig. 4.15b shows a histogram of the squeeze-out pressure required for the n=1→0 transition in hexadecane with data taken from various probes and repeated experiments. The median squeeze-out pressure is 0.79 GPa.

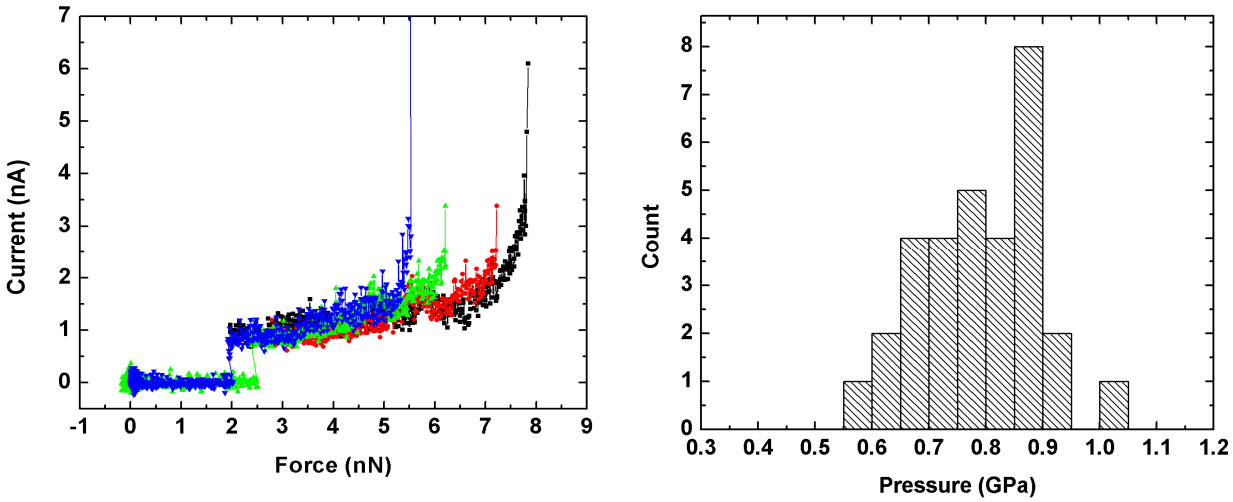

Figure 4.15 (a) Repeated current vs. force data obtained on the hexadecane monolayer (n=1). (b) Histogram of the squeeze-out pressure for the n=1→0 transition. Data is taken from five individual AFM probes. The tip-sample contact area used in the calculation of the pressure is found using the DMT model for each force curve.

The calculated areas of ~10 nm^2 at the n=1→0 squeeze-out corresponds to ~ 10 hexadecane molecules in the contact zone. This is much less than comparable squeezing experiments using the SFA involving contact areas of ~1000 μm^2. In SFA measurements [46] there is a gradual thinning of the confined film as it is squeezed between two surfaces, with regions of n and n-1 layers coexisting within the time frame of the squeeze-out experiment. This results from a balance between the hydrodynamic pressures exerted by the liquid and elastic restoring forces from the deformed solid surfaces [190]. Such behaviour is not expected over the length scale of AFM measurements and hydrodynamic descriptions of the squeeze-out are not appropriate. The AFM experiments resemble a single asperity contact and are expected to be closer to descriptions provided by computer simulations [104]. Indeed molecular dynamics computations show the average squeeze-out pressure for tetradecane confined between

two gold surfaces is ~0.8 GPa for the n=1→0 transition [166], which is comparable with our experimental data (~0.7GPa). Note that the relevant data set from the simulations [166] is the so called "un-pinned" case, in which the substrate-adsorbate interaction is weak. This is certainly the case for alkanes adsorbed on HOPG [115], with the characteristic monolayer domain structures arising from strong adsorbate-adsorbate interactions rather than commensurability with the underlying substrate.

Current vs. force data for the second layer (n=2) is shown in Fig. 4.16. The sensitivity is limited by the very small currents involved (pA) and our conclusions are thus qualitative. We find the contact area increases gradually with load and is of the same order as found for the first layer. The pressure required to squeeze-out the second layer (n=2→1) is ~0.6 GPa. Interestingly, this is only slightly smaller than the pressure required for the n=1→0 layer transition and more than the theoretically predicted value of ~0.2 GPa [166], although it must be emphasized again that our small current values result in large error. We observe no "fast" region where the current increases suddenly just before the n=2→1 transition, suggesting that no significant conformation change occurs in the layer during compression. This may be a consequence of the second layer being in a more liquid like state than the first layer. However, to investigate the issues further requires C-AFM measurements to be undertaken at higher applied voltages (>>1V) to increase the current. Such experiments cannot be undertaken with the tips available at present.

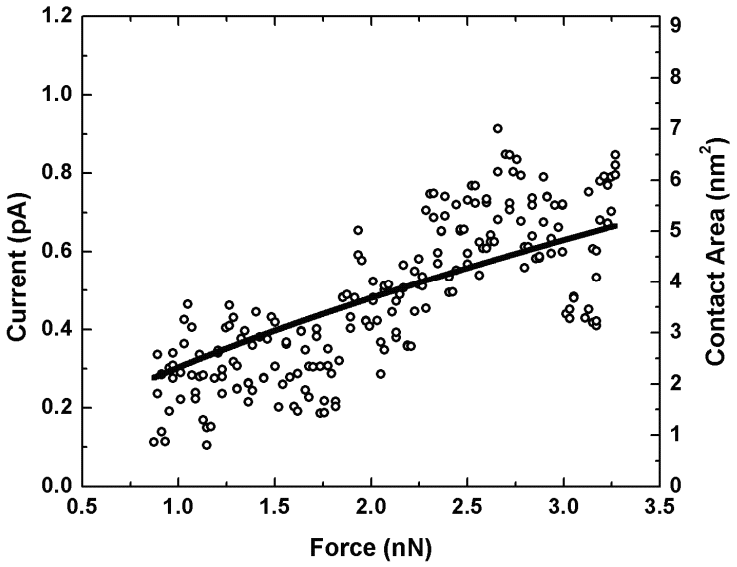

Figure 4.16: Variation in current as a function of applied force with the tip in contact with the second hexadecane layer (n=2). A DMT profile is superimposed (solid curve) to estimate the mechanical contact area.

4.3.1.3 Tunneling though an Alkane Monolayer

Current-Voltage (I-V) data can be found using C-AFM when the tip lies within a solvation layer, and Fig. 4.17 gives an example for the n=1 layer in hexadecane. However, there is considerable difficulty in accurate modeling of the electrical behaviour across the solvation layer which stems from the presence of the hexadecane between the electrodes. The tunneling between the tip and sample is modified by the presence of the molecular orbitals of the molecule. A very common approach is to approximate the transmission with a single barrier based on Simmons [112] (Eqn. 2.21). A curve fit using Simmons equation is shown for the hexadecane data of Fig. 4.17.

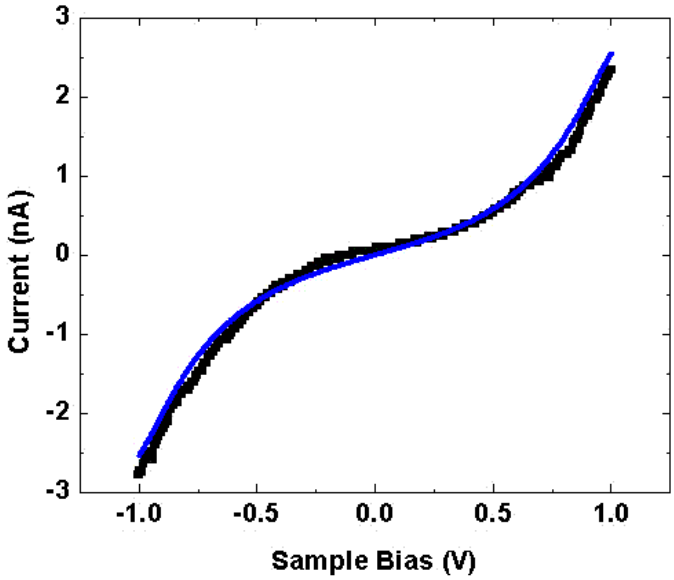

Figure 4.17: Data showing I-V curve obtained on a hexadecane monolayer on HOPG. The data is fitted with Eqn. 2.21 (blue curve).

The fit is good but the resulting parameters are clearly in error e.g. the fitted contact area is typically ~0.015 nm^2, the barrier height ϕ~0.56 eV. This problem is also observed for tunneling through alkanethiol monolayer on gold [113]. As discussed in Section 2.5.2, the utility of Eqn. 2.21 is very doubtful to accurately model the data.

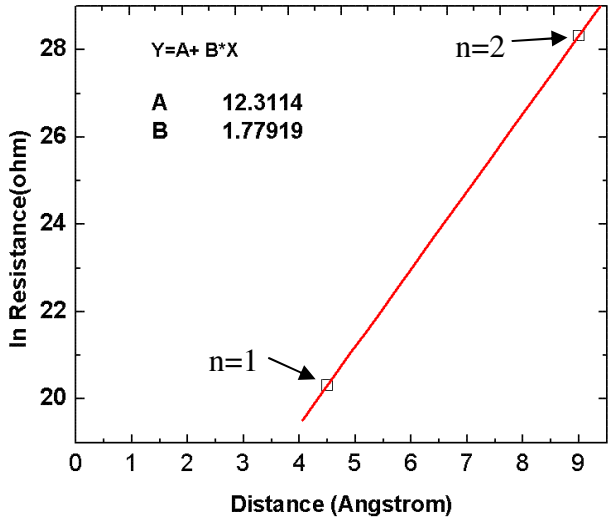

Figure 4.18: Log of resistance measured at low bias on hexadecane layers (n=1 and n=2) plotted against tip-sample distance. A linear fit (red line) provides the value of parameter β using Eqn. 2.23.

Analysis of the data based on Landauer formula (Eqn. 2.23 and 2.24) is shown in Fig. 4.18, where the contact resistance measured at low bias and low force for the n=1 and n=2 layers is plotted as a function of the tip-sample distance (which is equivalent to the tunnel gap s). Fitting the data to Eqn. 2.23 gives $\beta \approx 1.8$ Å^{-1} and $R_0 \approx 180$ kΩ. These are reasonable values for molecular systems but N (Eqn. 2.24), and hence the contact area, cannot be found from R_0 unless the transmissions T_{sub} and T_{tip} are known independently [113]. If we assume $T_{sub} \sim T_{tip} \sim 0.01$, as found for Au-$CH_3$ contacts [113], then from Eqn. 2.25 and 2.26 $N \sim 1000$ molecules. This corresponds to contact area of $\pi a^2 \approx 500$ nm^2 for the n=1 layer, which is two orders of magnitude higher than values calculated from the DMT model.

In summary, it is very difficult to extract reliable values of the *absolute* contact area from tunnel current measurements and the mechanical modeling approach is preferred.

4.3.2 Squalane

4.3.2.1 Conduction through the Au-HOPG Contact

We now present the analysis of the Au-HOPG contact in squalane. Fig 4.19 shows pull off current vs. force while the probe is in contact with the graphite (n=0) after pushing through all the solvation layers of squalane. The plot of current vs. force shows the *relative* change in area with applied force. As shown in Section 4.3.1.1 a detailed model of the Au-graphite contact can be made using the Maugis-Dugdale theory (MD) for an elastic contact. A good fit to the squalane current vs. force data is found (blue solid line) with a value of $\alpha = 0.06$ i.e. again close to the DMT model. The contact area is calculated from the data fit to the MD model.

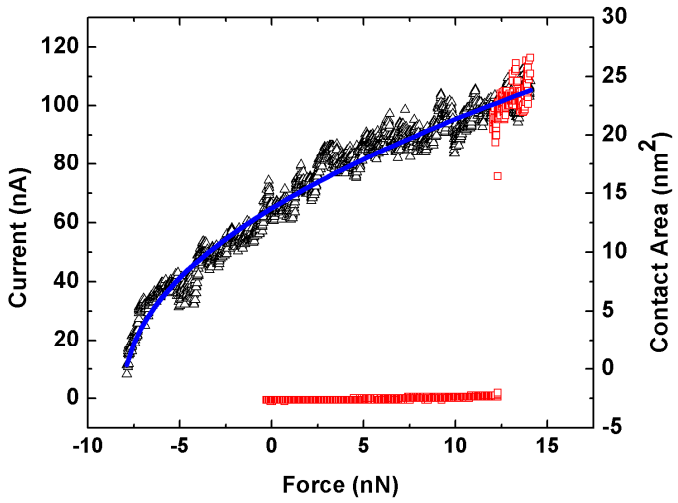

Figure 4.19: Current vs. force curve for squalane showing the tip is in contact with the graphite (n=0). On approach (red square) the current jumps to a high value when the monolayer (n=1) is squeezed out at ~12.5 nN. The variation in current while pulling off the tip (black triangles) is fitted with the Maugis-Dugdale model (blue solid line) to give the contact area. Data is taken at room temperature with a Au coated cantilever of spring constant 0.76 N/m and tip radius ~36 nm.

4.3.2.2 Conduction through Solvation Layers

The simultaneously measured current with force curve within the squalane monolayer (n=1) is shown in Fig. 4.20. Several force curves obtained using the same tip are re-plotted in Fig. 4.21 as current vs. force curves. The behavior of the curves is repeatable, although the force needed for n=1→0 transition varies slightly (~8-11 nN). The curves also reveal two distinct regions in the monolayer where the current shows a slow rise with force at low forces, and a fast current increase close to the complete squeeze-out of the layer (i.e. near n=1→0 transition). All this behavior is entirely similar to that observed for the squeeze-out of a hexadecane monolayer (Section 4.3.1.2). Similarly, we can model the slow varying region using continuum mechanics and assuming the current is proportional to the tip-sample contact area. The inset (Fig. 4.21) shows the current variation as the tip is pulled off the squalane monolayer. The data is well fitted to a DMT model. In the fast current region the molecules presumably undergo some rearrangement prior to being squeezed out of the contact, as in the case of hexadecane. Computer simulations would be required to check this hypothesis.

The fitting of the current vs. force data to the DMT model shows that in the slow current region changes in the tip-sample contact area are the principal cause of the observed variation in current flow. There is negligible deformation of the squalane monolayer (~ 1.0 Å) at the highest applied loads (~10 nN). This is entirely similar to the observations using hexadecane, and shows that the branched molecule squalane also behaves as an elastic solid-like monolayer.

Importantly, we note that at 25 °C both the hexadecane and squalane monolayers form an ordered lamellar structure which is imaged using STM (see Fig. 4.7). This is a major reason we describe the behavior as being "solid-like". Another strong reason is the good fit of the data to continuum models for a solid elastic contact. These two points compel us to associate current vs. force curves such as Fig. 4.21 with a solid-like behavior of the confined material.

Naturally, not all liquids exhibit solid-like mechanical properties when confined, nor does the same confined liquid show a fixed material state (solid, liquid) as the temperature and time scale of the experiment varies. These critical aspects (time, temperature, type of molecule) are discussed in the remainder of this chapter.

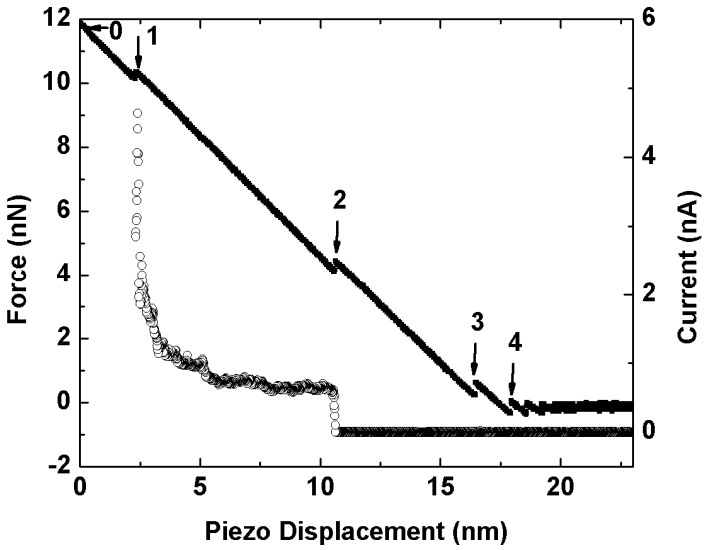

Figure 4.20: Simultaneous force (solid line) and current (circle) measurements for squalane on HOPG as a function of displacement of the piezoelectric actuator. Current is shown for the n=1 layer. The tip is approaching the surface. Solvation "jumps" are observed in both the force and current curves and are labeled n=0 to 4, with n=0 being the tip in contact with the HOPG substrate. Data is taken at room temperature with a Au coated cantilever of spring constant 0.76 N/m and tip radius ~ 36 nm.

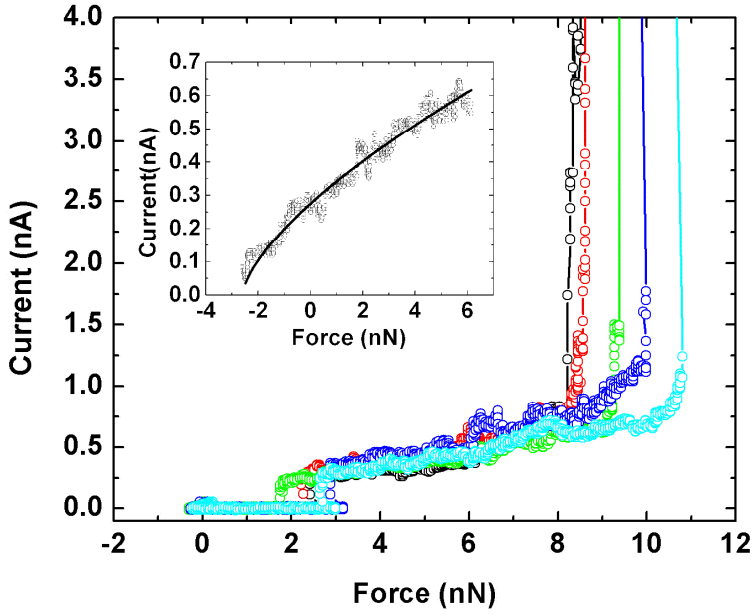

Figure 4.21: Current vs. force curve for the tip in contact with the first squalane layer (n=1). There are distinct "slow current" and "fast current" regions. The large increase in current corresponds to the n=1→0 layer transition. The inset shows data, taken with the same tip, as the tip is pulled off the first layer. The variation of current follows DMT mechanics.

4.3.3 *2,2,4,4,6,8,8-* Heptamethylnonane (HMN)

4.3.3.1 Conduction through Au-HOPG Contact

Fig. 4.22 shows current vs. force data for HMN with the tip in contact with the HOPG (n=0). In hexadecane and squalane the current vs. force curves are reversible in loading and unloading cycles. The tip-HOPG contact mechanics is very different in HMN. We observe a gradual variation of current, even up to forces of ~ 20 nN where the contact resistance in HMN (192±169 MΩ per nm^2) approaches the resistance found in squalane (76±21 MΩ per nm^2); an observation which gives confidence that the tip is indeed in electrical contact with the HOPG surface, at least under high loading. At smaller loads

(≤10 nN) the gradual increase in current makes it difficult to determine at what force mechanical contact first occurs. Also, the current variation with load does not follow a reversible path, with significant hysteresis and variability observed between the approach and retraction cycles.

Most importantly, we also find that the current vs. force curve cannot be fitted to the MD expression. This is a remarkable result as it implies the elastic deformation of the simple Au-HOPG contact in a liquid environment does not follow the known continuum mechanics of a point contact. A reason for this behaviour, the trapping of liquid within the contact zone (Fig. 4.25) is postulated in the next section.

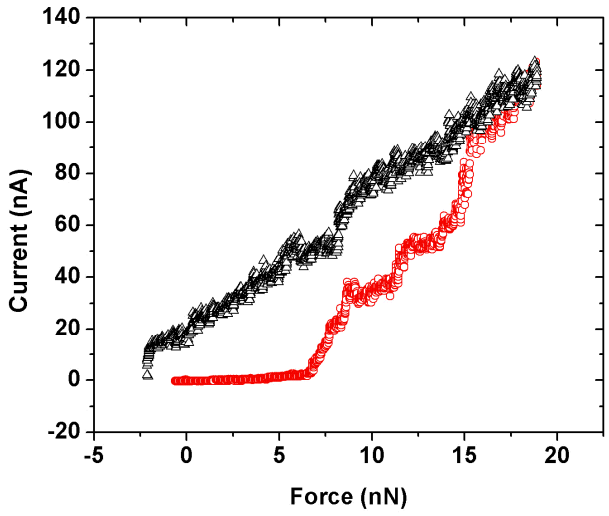

Figure 4.22: Current vs. force curve for the tip at high force in HMN. The variation in current is shown while approaching (red circles) and pulling off the surface (black triangles). The n=1→0 layer transition is very poorly defined.

4.3.3.2 Conduction through Solvation Layers

Fig. 4.23 shows a force curve and Fig. 4.24 corresponding sets of current vs. force measurements where the tip is probing the HMN monolayer (n=1). Solvation jumps are observed in the force and these can be associated with significant (but not abrupt) changes in the measured current. However, the current signals (Fig. 4.24) do not show a consistent variation with force, as compared to squalane or hexadecane and the data cannot be fitted to any generalized model of an elastic point contact, such as the MD model. A simple observation of Fig. 4.23 shows the current is varying in a complicated manner with load.

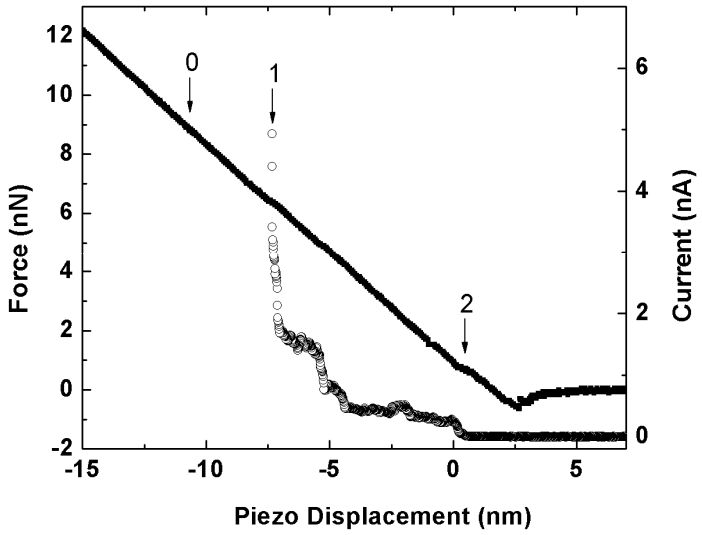

Figure 4.23: Simultaneous force (solid line) and current (circle) measurements for HMN on HOPG as a function of displacement of the piezoelectric actuator. Current is shown for the n=1 layer. The tip is approaching the surface.

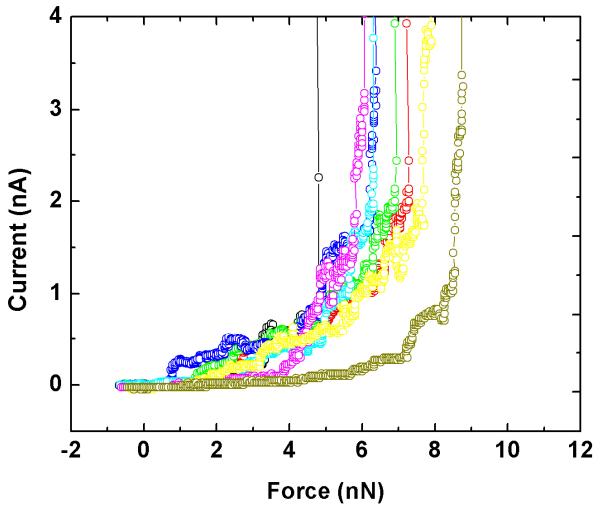

Figure 4.24: Current vs. force curve for HMN at low forces, where the tip is most probably within the HMN monolayer (n=1). The current variation with force is erratic and non-reproducible indicating the confined material is disordered or liquid-like.

We believe the trends in the HMN data (hysteresis, non-uniform variation with force), and also the kinks and blurred layer transitions (see Fig. 4.3) arise because the HMN molecules are in a liquid-like state. It is significant that we cannot fit elastic continuum models to the current vs. force data for both the HMN monolayer (n=1) and to the tip-graphite junction (n=0). This result is surprising and implies that the increased fluidity of the material near or within the junction negates the use of point contact models developed for simple elastic solids.

An explanation of the HMN results can be found in recent simulations comparing the squeeze-out of a linear alkane (butane) and it's branched isomer, iso-butane [99]. The linear molecules form an ordered monolayer and are completely removed from the contact zone under applied pressure. The branched isomer (iso-butane) remains liquid-

like in the contact zone and shows a higher resistance to displacement, leading to the trapping of a few molecules [99], even at very high pressure. Essentially, the confined molecules display viscoelastic behavior and are displaced only slowly from the gap. If the pressure becomes sufficiently high before the molecules can be displaced, then the confining surfaces will deform enabling hollows filled with iso-butane to be created. Fig. 4.25 shows the proposed hypothesis pictorially.

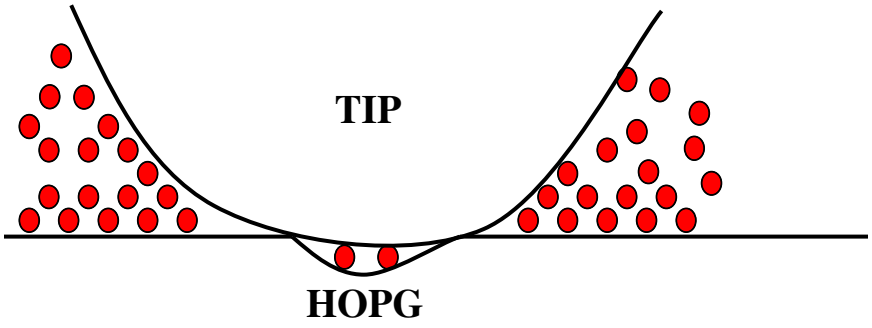

Figure 4.25: A cartoon showing trapping of confined molecules under the nanoscale contact.

We confirm this interpretation by drifting the tip extremely slowly (~ 1.0 nm/sec) towards the surface; waiting ~10 seconds at high applied load (~15-20 nN); and finally pulling the tip off the surface as in a routine force curve at ~ 10 nm/s. The pull off force curve is now similar to a tip in contact with HOPG in squalane or hexadecane and is well fitted by a DMT model (Fig. 4.26), i.e. a point contact elastic response is recovered, thus demonstrating that a solid-solid contact can be formed in HMN if the loading rate is very slow during approach. At the slower approach speed (~1nm/s) the confined molecules are not trapped but have time to be squeezed out of the contact zone.

Note that it is not possible to directly compare the approach force curve at ~1nm/s and ~10 nm/s because of experimental drift at low approach speeds. However, the approach curve in Fig 4.26 , which is done immediately after the pull off curve at a speed of ~10nm/s, reverts to the force curves shown previously (Fig. 4.22) indicating a trapping of HMN molecules. Thus, for the HMN system at 25 ^{o}C, there is a critical approach velocity of ~5 nm/s separating molecule trapping and non-trapping. A HMN molecule must typically move a distance of the contact radius a ~ 2.5 nm to be squeezed out of the tip-sample contact zone, giving a characteristic time for the molecular motion during squeeze-out of ~ 0.5 sec. This is a very long time but is not unusual for a solid of glassy material. In a recent AFM study [164] the interaction stiffness and viscosity was measured for OMCTS confined between a Si tip and a SiO_2 surface. The force curves showed solvation layering of the OMCTS but the state of the confined material depends critically on the tip-sample approach rate. At low speed ($\leq$ 0.3 nm/s) the confined OMCTS is liquid-like whereas at high speeds ($\geq$ 1 nm/s) the molecules become solid-like i.e. the molecules are "jammed" within the contact zone, inhibiting the squeeze-out. Thus, there is a liquid-glassy solid transition at a critical approach rate of ~0.5 nm//sec. This is similar to the critical approach rate in our experiments on HMN. While we cannot comment on the solid or liquid state of the confined HMN (we cannot measure a meaningful force curve at low approach speeds because of drift) our work proposes a new phenomenon, that of trapping or non-trapping of molecules, which is entirely consistent. At fast approach rates, the confined material becomes more solid like, and hence molecules may become trapped in the contact.

Finally, we also measure considerably smaller pull off force in HMN (3.7±1.4 nN) in comparison to squalane (7.8±2.5 nN), and hexadecane (6±1.2 nN) in agreement with a recent simulation showing the presence of liquid between two confining solid walls can reduce the pull off stress [191] .

All of the observations lead to the view that trapping of HMN molecules under the tip during compression is plausible.

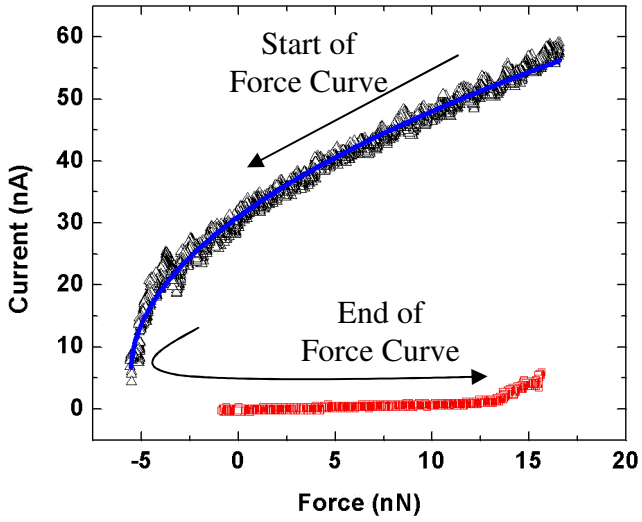

Figure 4.26: Current vs. force curve taken after slowly drifting the tip (~ 1 nm/sec) to the HOPG surface and taking a reverse force curve (pull off followed by approach) with normal speed (~10 nm/sec). The pull off curve shows solid-solid contact behavior and can be fitted with DMT model (blue curve). The approach curve shows much lower current at the same force indicating trapping of molecules under the contact zone, reducing the contact area and hence the measured current.

4.4 Measurements at Elevated Temperature

4.4.1 Squalane

The previous section and many publications [14, 45, 46, 66, 71, 99, 164] have shown that the dynamics of the molecules (i.e. timescale) is a key consideration in understanding confined liquid. The dynamics of molecular motion are intimately related to the temperature of the system, through changes in various energy barriers e.g. hole nucleation for squeeze-out, diffusion in bulk and on surfaces, etc. In this section the influence of time and temperature is examined to further understand the fundamental differences in behavior arising from the ordered or disordered state of the solvation monolayer. All experiments were carried out at elevated temperature and compared to the room temperature (25 °C) data discussed in the previous sections.

The squalane monolayer has been shown to undergo melting transitions above 50 °C from recent computer simulations [77]. To understand how this melting influences solvation and squeeze-out behavior, C-AFM experiments were performed at 65 °C in a similar fashion to those at room temperature. Fig. 4.27 shows a force vs. distance curve at 65 °C. The solvation jump distances are similar (6.3±0.4 Å) but the solvation layering is very weak compared to room temperature measurements (see Fig. 4.20). This indicates that it is easier to squeeze-out the solvation layers at higher temperature i.e. the activation barrier has been lowered by the temperature increase [104].

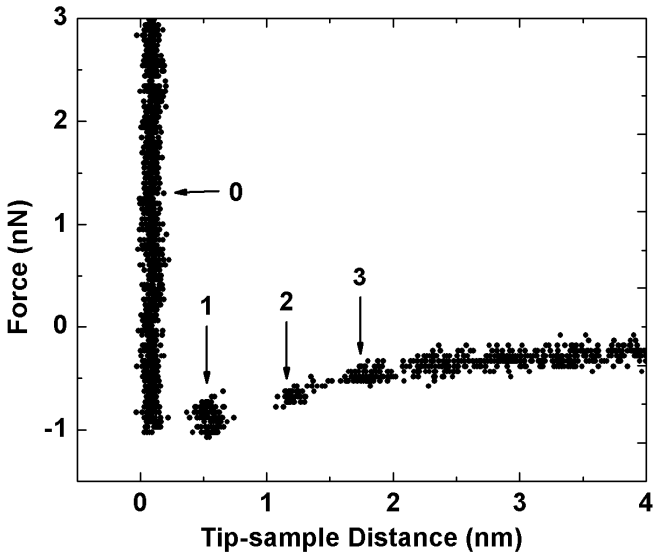

Figure 4.27: Force as a function of the tip-sample separation for squalane on HOPG at 65 ^{o}C. Solvation "jumps" are observed (labelled n=1, 2) but these are very weak.

Given the very small forces measured in the solvation layers, the best insight is gained by considering the tip-HOPG contact (n=0). Fig 4.28 shows current vs. force data at 65 ^{o}C with the tip in contact with HOPG (n=0). The tip-HOPG contact mechanics is very different from that at 25 °C (Fig. 4.19). We observe a gradual variation of current, even up to forces of ~ 15 nN; at which force the tip is certainly in contact with the HOPG surface for squalane at 65 °C. The current variation with load cannot be fitted to elastic contact models; and does not follow a reversible hysteresis path; and significant variability between data sets is observed. This behavior is very similar to the HMN data at 25 °C (see Fig. 4.22). We conclude that this behaviour indicates the trapping of molecules under the contact zone, as discussed in Section 4.3.3.2.

As discussed for HMN, the possibility of trapping of squalane molecules under the contact zone was confirmed by drifting the tip extremely slowly (~ 1.0 nm/sec) towards the surface; waiting ~10 seconds at high applied load; and finally pulling the tip off the surface as in a routine force curve at ~10nm/s. We observe a pull off force curve (Fig. 4.29) which is similar to a tip in hard contact with HOPG (Fig 4.19), demonstrating that a solid-solid contact can be formed if the loading rate is very slow. Under these conditions the current vs. force pull off curve can be well fitted using the DMT model. As described for HMN (Section 4.3.2.2), the slower approach speed allows molecules to escape from the contact zone and trapping does not occur.

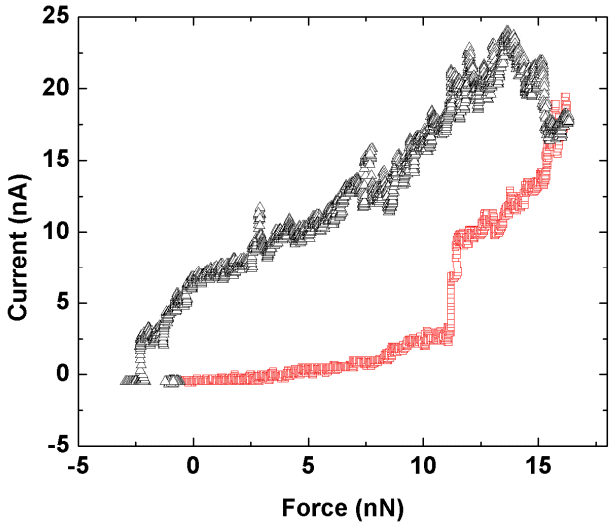

Figure 4.28: Current vs. force curve for squalane on HOPG at 65 °C. The variation in current is shown for approach (red) and pulling off (black). The approach curve between 0-5 nN is certainly sampling the squalane monolayer (n=1) and at high forces (≥ 11 nN) the HOPG substrate, but the transition of the tip from confined liquid to the graphite surface is not clearly defined.

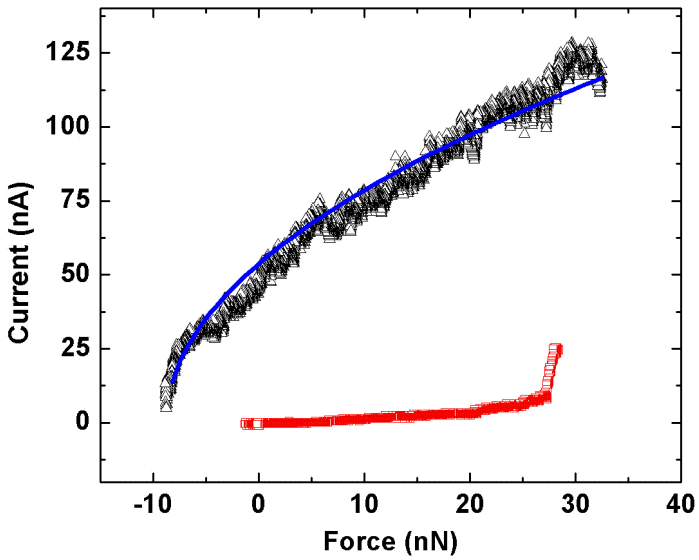

Figure 4.29: Current vs. force curve taken in squalane at 65 °C after slowly drifting the tip at ~ 1 nm/sec to the HOPG surface and taking a reverse force curve at ~10 nm/s i.e. a pull off is done first, followed by the approach. The pull off curve (black) shows solid-solid contact behavior and is fitted with the DMT model (blue curve). The approach curve (red) shows much lower current at the same force indicating trapped molecules under the contact zone.

The increase in temperature for squalane has led to molecule trapping in the contact zone during squeeze-out of the monolayer. This is surprising given that an increase in temperature decreases relaxation times of a material and lowers energy barriers i.e. molecules are more mobile and should move more *easily* out of the contact zone for a fixed approach rate. From this arrangement, one would expect trapping as the temperature was lowered. We believe the reason is because the solid monolayer at 25 °C has melted into a disordered state at 65 °C. Indeed, repeated STM experiments could not image any squalane related features at 65 °C. The trapping mechanics brings added complexity to the traditional view of confined liquids solely in terms of relaxation times.

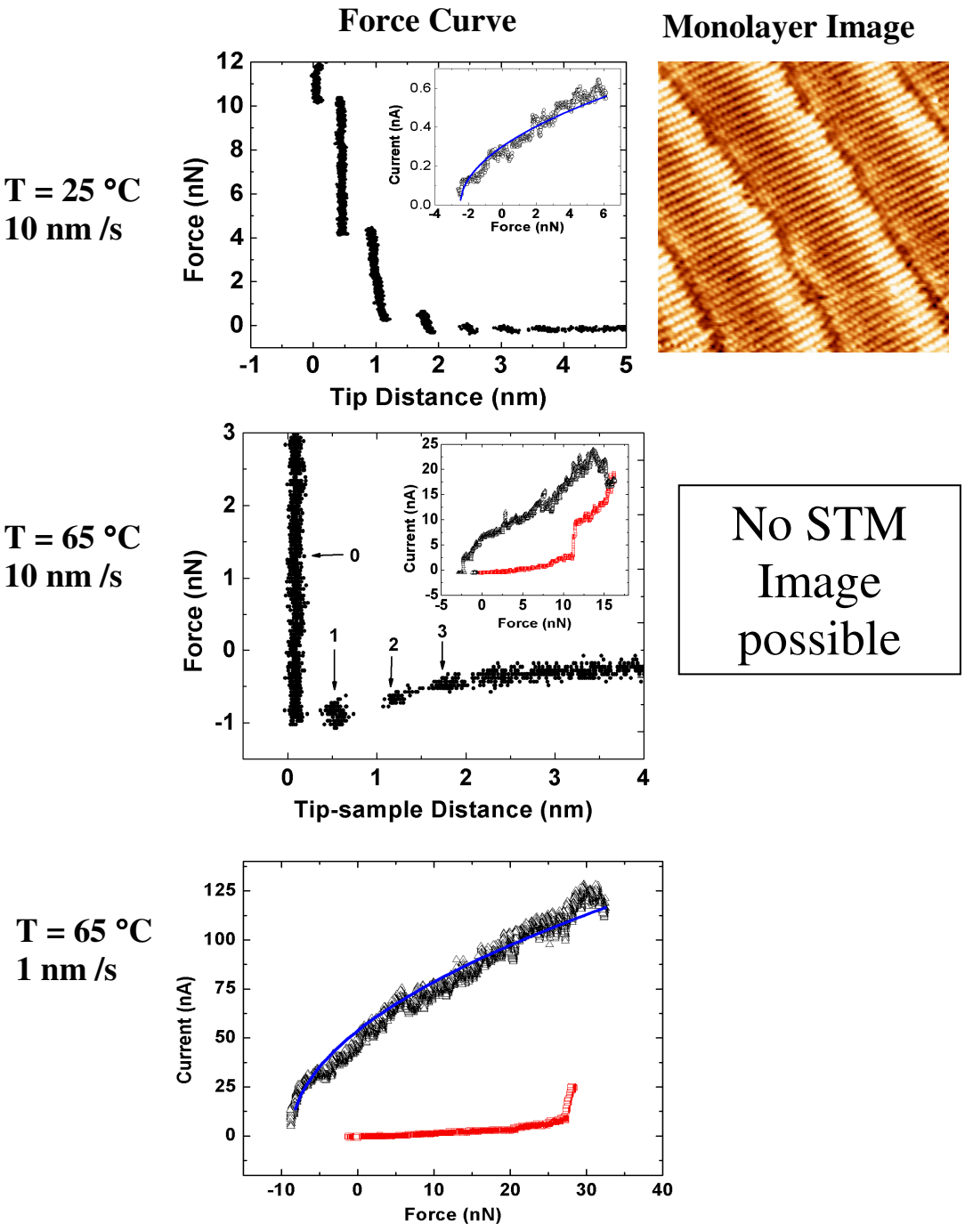

Fig 4.30: A montage summarizing the various states of the squalane system.

In the ordered solid monolayer (e.g. squalane at 25 °C) the relaxation time is very long but no molecules are trapped on squeeze-out because the film is sufficiently rigid that once hole nucleation occurs, entire rigidly coupled groupings of molecules are forced out of the contact. In the disordered monolayer (e.g. squalane at 65 °C) the confined monolayer is in a liquid or more probably glassy state (because of the very slow critical approach speeds, as discussed in Section 4.3.3.2). In this case the squeeze-out dynamics follows standard ideas on relaxation times, with slow times (i.e. slow approach rates) required to ensure molecules are not trapped.

Fig. 4.30 summarizes the general picture for the squalane system. At temperatures less than monolayer melting, the squalane behaves as a well ordered solid-like structure that can be imaged. Above monolayer melting temperatures (65 °C) the monolayer becomes disordered, no SPM image can be obtained and molecule trapping can occur at fast approach speeds.

4.4.2 HMN

Data for HMN (Fig 4.31) at elevated temperature (65 °C) shows similar behavior to measurements at 25 °C (Fig. 4.22). The current vs. force data taken after slowly drifting the tip to the HOPG surface at ~1 nm/s (Fig. 4.32) also shows entirely similar behaviour as the data taken at 25 °C (Fig. 4.26). This suggests that the HMN molecules, which are in disordered state at room temperature, do not appreciably enhance their mobility with an increase in temperature of 40 °C. Molecules remain trapped in the contact if approach speed is sufficiently fast.

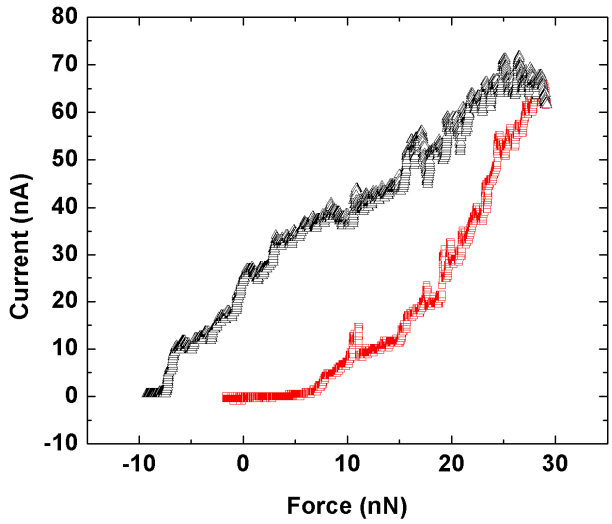

Figure 4.31: Current vs. force curve for the tip in HMN at 65 °C and ~10 nm/s approach speed. The data shows the variation in current while approaching (red circles) and pulling off (black triangles). The general form of the data is similar to that at 25 °C.

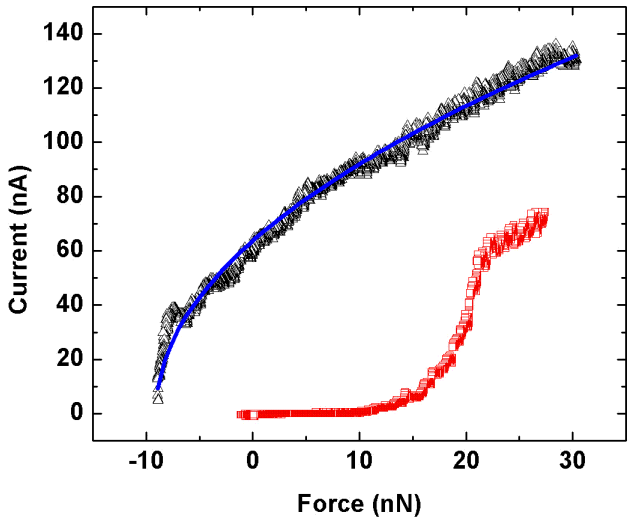

Figure 4.32: Current vs. force curve taken in HMN at 65 °C after slowly drifting the tip at ~ 1 nm/sec to the HOPG surface and taking a reverse force curve at ~10 nm/s i.e. a pull off is done first, followed by the approach. The pull off curve (black) shows solid-solid contact behavior and is fitted with the DMT model (blue curve). The approach curve (red) shows much lower current at the same force indicating trapped molecules under the contact zone.

4.4.3 n-Alkanes

The basis of the trapping results is confirmed by preliminary studies of a series of n-alkanes (decane C10, dodecane C12, tetradecane C14, hexadecane C16). As before, C-AFM was undertaken using Au coated Si_3N_4 tips on HOPG completely immersed in the liquids. Fig. 4.33 summarizes the current vs. force data. Solvation forces are observed in all the liquids and current flow is also measured in the monolayer (n=1), but Fig. 4.33 only highlights the high force region where the tip is in contact with the HOPG (n=0). In the n=0 region we clearly observe the trapping or non trapping behaviour, which is directly correlated with the monolayer being in either an ordered or disordered state. At room temperature the C16 and C14 monolayers are ordered. The C16 monolayer can be readily imaged using STM or AFM. We could not image the C14 monolayer at room temperature. The current vs. force curves at 25 °C show no trapping and sharp, well defined solvation layer transitions. The C12 and C10 monolayers cannot be imaged at 25 °C, being completely disordered as the melting temperature of the monolayers is well below room temperature (see Table 4.2). Consequently, the resulting current vs. force data shows poorly defined layer transitions and evidence of trapping (for approach speeds of ~10 nm/s).

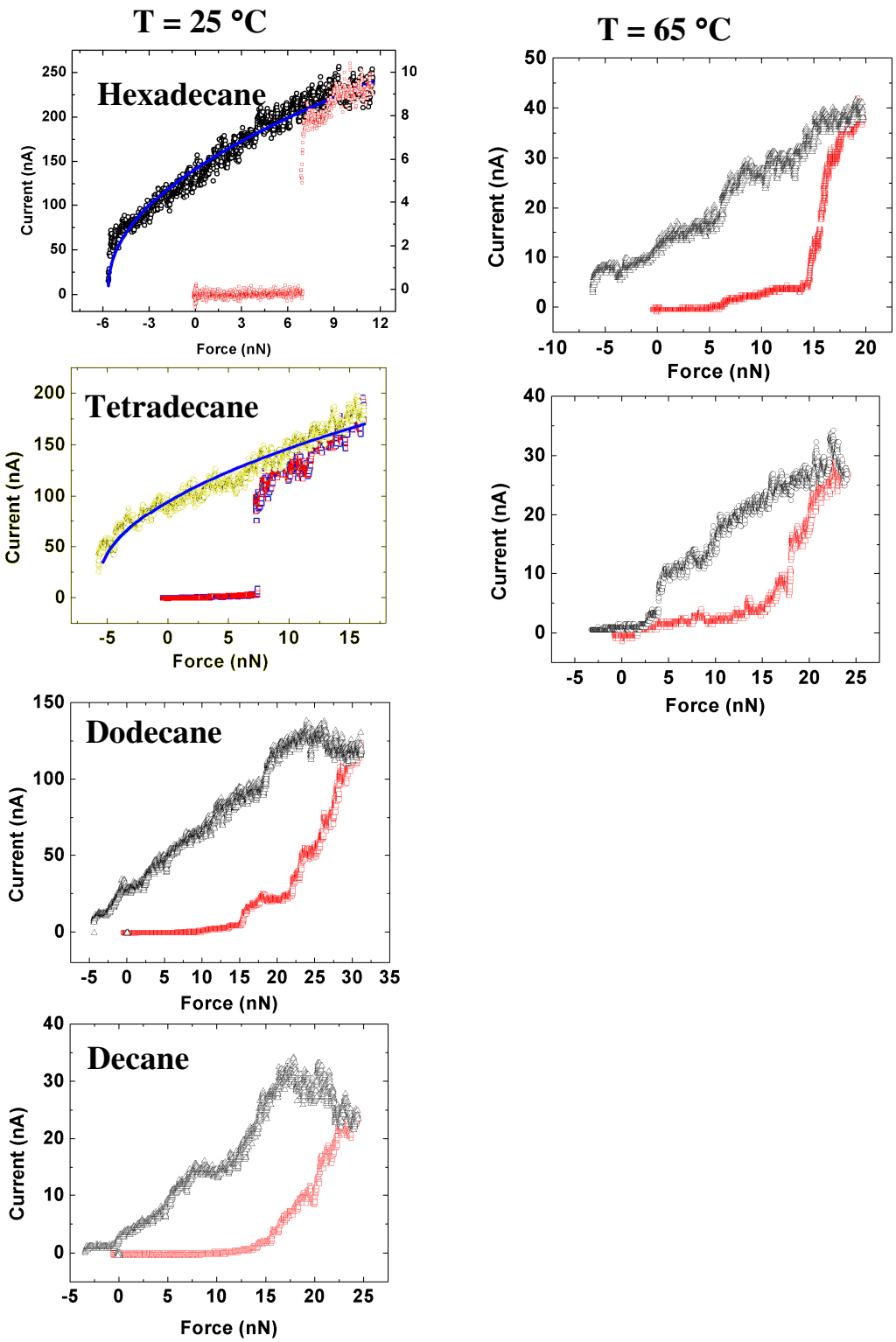

Figure 4.33: A montage summarizing the various force curves of alkane systems in contact with the HOPG (n=0). All force curves are taken at 10 nm/s approach speed.

Table 4.2: Summary of data for n-alkanes on graphite. The bulk and monolayer melting temperatures are from ref. [174].

No. Carbon atom C_nH_{n+2}	Bulk melting Temp. (°C)	Monolayer melting Temp. on graphite T_m (°C)	Image at 25 °C of monolayer?	Current vs. Force behaviour (at 25 °C)
C 10	-32	-5	No	Disordered
C 12	-12	19	No	Disordered
C 14	5	35	No	Ordered
C 16	16	55	Yes	Ordered

C-AFM experiments were also performed in C14 and C16 above their respective monolayer melting temperatures (Fig. 4.33). The current vs. force curves (at ~10 nm/s approach speed) show trapping behaviour in ~90% of the curves. Further, no image of the ordered monolayer could be obtained.

These findings verify the key role played by the ordered or disordered state of the monolayer in liquid trapping during squeeze-out and Table 4.2 summarizes the key findings this far. Note that the lack of an AFM or STM image of an ordered monolayer is convincing but not conclusive that the monolayer is disordered. The resolution may simply be too poor to image short range order in the smaller length alkanes. However, emphatic supporting evidence comes from spectroscopy measurements for alkane adsorption on powered graphite [174], which directly measure the monolayer melting temperatures T_m (see Table 4.2). Such data conclusively shows that at room temperature the C10 and C12 monolayers have melted whereas the C14 and C16 monolayers are

solid. Similarly, the lack of an image for the C14 monolayer at 25 °C does not imply there is no ordered monolayer. The melting temperature is only slightly above room temperature and perhaps a lack of long range order or increased molecule mobility makes imaging very difficult experimentally.

4.5 Summary

We have performed simultaneous force and conductivity measurement of hexadecane, squalane and HMN liquids confined between a conducting AFM tip and graphite surface. For hexadecane, both the current and the force data reveal discrete solvation layering near the surface and at more realistic forces than previously reported [163]. The squeeze-out of the monolayer of hexadecane at room temperature (25 °C) follows that of a solid, ordered monolayer. The variation of current with force is well described by continuum mechanical models of the junction deformation, excepting a region just before the n=1→0 layer transition where prior to the complete removal of the n=1 layer there is a rearrangement of molecules under the tip apex bringing the tip closer to the substrate. This subtle configuration change could not be inferred from measurement of the applied force curve only and is an interesting result for lubrication studies showing that, even for nanoscale asperity contacts, the squeezing out of the boundary layer is not a smooth, continuous event. We have also compared the absolute electrical and mechanical contact area for the tip-graphite contact (n=0) and the mechanical approach appears more robust.

We observe that strong solvation layering and surface ordering is possible even in the highly branched alkane squalane. The ordered nature of the squalane monolayer is

supported by the first direct imaging of the squalane monolayer using scanning tunneling microscopy, in agreement with recent simulation studies. Conducting AFM data shows that the expulsion of the ordered squalane molecules at 25 °C is a step-like event, exactly similar to hexadecane. In contrast, the more densely branched alkane HMN cannot be imaged and is in a disordered state at room temperature. The force curves show poorly defined solvation layering. Importantly, the force data for HMN cannot be modeled as a single elastic contact and comparison with simulations indicates that some confined material remains trapped in the contact zone, even at high pressure.

In brief, continuum elastic models are well suited to describing the current vs. force data of ordered, solid-like material such as squalane and hexadecane at 25 °C. However, when the confined liquid is disordered, as for HMN or squalane at 65 °C, the current vs. force curve is qualitatively very different, and simple elastic models cannot be applied because of molecule trapping. Trapping of molecules was further confirmed by experiments a) at different tip-sample approach rates, showing that at sufficiently low speeds molecules can escape the contact zone and a solid-solid tip-sample contact formed; b) at higher temperatures (65 °C), above the monolayer melting transition, the squalane monolayer data shows similar behaviour as obtained for HMN; c) in a series of n-alkanes at 25 °C, the current vs. force curves for the shorter chain alkanes (C10 and C12) show trapping behaviour because the monolayers are disordered, whereas the well ordered, solid monolayers of C14 and C16 follow a continuum elastic response.

Chapter 5

Measurements on a Self-assembled Monolayer

In this chapter a C-AFM study of chemically adsorbed alkanethiol molecules (decanethiol, also labeled as C10SH) is presented. These molecules form a well ordered self-assembled monolayer (SAM) on atomically smooth Au(111) surface [192]. Such chemically adsorbed species provide a means of modifying the chemistry of metallic surfaces (e.g. Au, Ag, Pt etc.) [193]. The alkanethiol monolayer produces a very low surface energy surface and behaves as an ideal molecular lubricant [193], as these monolayers are robust and inhibit direct contact of the underlying metal surface with other surface brought into contact. An important aspect is to understand the mechanical behavior of these model boundary lubricants at the molecular scale. A feasible approach is to use C-AFM because, as we revealed in Chapter 4, combining force and current measurements can provide a much deeper understanding of the contact mechanics. However, the fundamental basis of conduction across the SAM in a liquid environment must first be understood before any application in tribology; and this is the issue addressed in this chapter.

SAMs have also been extensively studied for molecular electronics to understand charge transport through the molecular layer sandwiched between two metallic electrodes as these monolayers can form an ideal tunnel junction between two electrodes [194]. However contacting the monolayer surface with a nanoscale electrode (e.g. AFM probe) introduces a large stress (few GPa) on the SAM [183]. Thus, understanding the detailed

mechanics of electrical contacts at the nanoscale with SAMs is also of great interest for applications in molecular electronics.

As discussed in Section 2.6.2, C-AFM has emerged as a very suitable technique to make contacts with molecular layers. A further refinement is to undertake C-AFM in a liquid environment. This minimizes surface contamination and eliminates capillary forces. However, a central problem is that a range of studies conducted on simple monothiol SAM have revealed a discrepancy by orders of magnitude in the measured contact resistance. In this chapter, the underlying reason for such discrepancy is investigated. We use C-AFM to study the liquid-monothiol SAM interface, the solvation layering which gives rise to oscillatory forces prior to the tip contact with the SAM, and the effect of these forces on the measured SAM contact resistance. The changes occurring in the transport characteristics of the junction in various surrounding media (air, hexadecane, OMCTS) were also measured as a function of applied force. In hard contact, the electrical measurements of the alkane monolayer SAM junctions are dependent upon the elasticity of the SAM (which in turn may depend on the surrounding fluid) and the applied force because the measured current is determined by intermolecular spacing (i.e. tilt) of the SAM molecules [125, 195].

Hexadecane and OMCTS were chosen as liquid media as these liquids are chemically inert and are geometrically well defined. These liquids have also been studied rigorously to understand fluid confinement effects [63, 64, 160]. At least two decanethiol SAM samples were studied in each medium. Each sample was tested with 4-5 new Au tips prepared under identical conditions.

Our results show that at very low forces (<3nN), there is no significant difference in contact resistance values measured using C-AFM in hexadecane and OMCTS, but a much lower contact resistance is measured in air. Liquid layering (solvation) can be observed as the liquid is confined between the tip and the SAM, but has no effect on the measured resistance of the SAM. At higher forces (> 5-6 nN) we find that the contact resistance drops dramatically in hexadecane in comparison with OMCTS. Current vs. force measurements and sample modulation AFM (SM-AFM) data indicate a significant variation in contact stiffness of the SAM in different liquids, consistent with the observed variation with force of the contact resistance. Thus the mechanical deformation of the SAM is very different in different fluid environments and this can account for the wide variations in the measured resistance of the SAM.

5.1 Structure and Stability of the Self-assembled Monolayer: Imaging

Firstly, it is important to confirm the structural integrity of the monolayer in various solvent media used. This is done by imaging the decanethiol (C10SH) SAM using STM in hexadecane, OMCTS and air. All the SAM samples were imaged before and after the C-AFM experiments using STM within the liquid. The $(\sqrt{3}\times\sqrt{3})R30°$ structure with c(4×2) superlattice of the SAM is always observed as previously reported [149] . There is no evidence of desorption of the SAM in the liquid mediums used within the period of the C-AFM measurements (3 to 4 hours) i.e. molecular resolution STM imaging showed identical structural details of the SAM irrespective of the surrounding media for a period of ~4 hours or more.

Fig. 5.1 and 5.2 show high resolution STM imaging in hexadecane, revealing that the SAM maintains structural integrity (packing density and lattice structure) after 3 to 4 hours exposure to hexadecane. Molecular scale imaging shows the typical c(4×2) lattice structure.

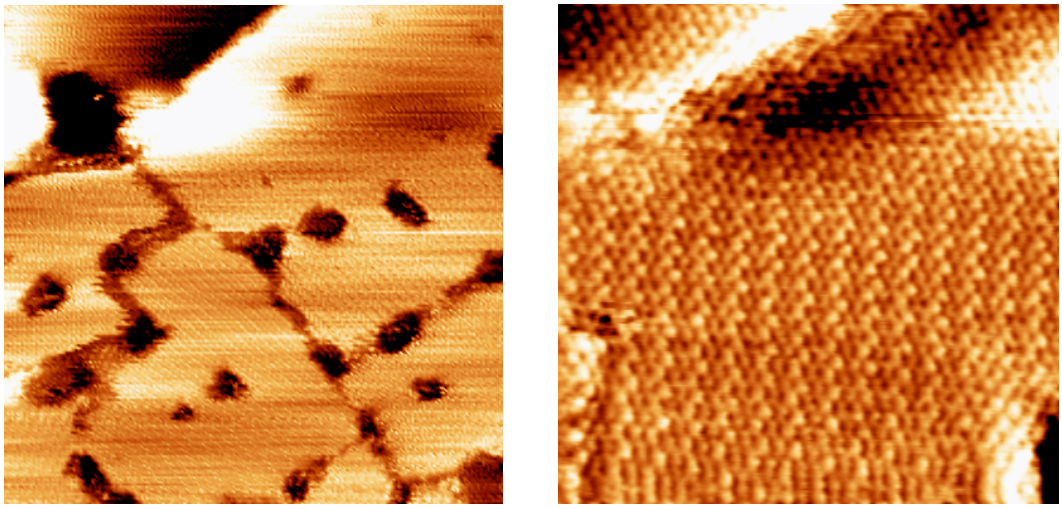

(a) **(b)**

Figure 5.1: STM images of the fresh C10SH monolayer in hexadecane, taken almost immediately after removing the sample from the alkanethiol solution: (a) 50 nm × 50 nm topographic image, (b) 15 nm × 15 nm topographic image. Tunneling conditions: V_{sample} = -1.0V, i_t=2 pA.

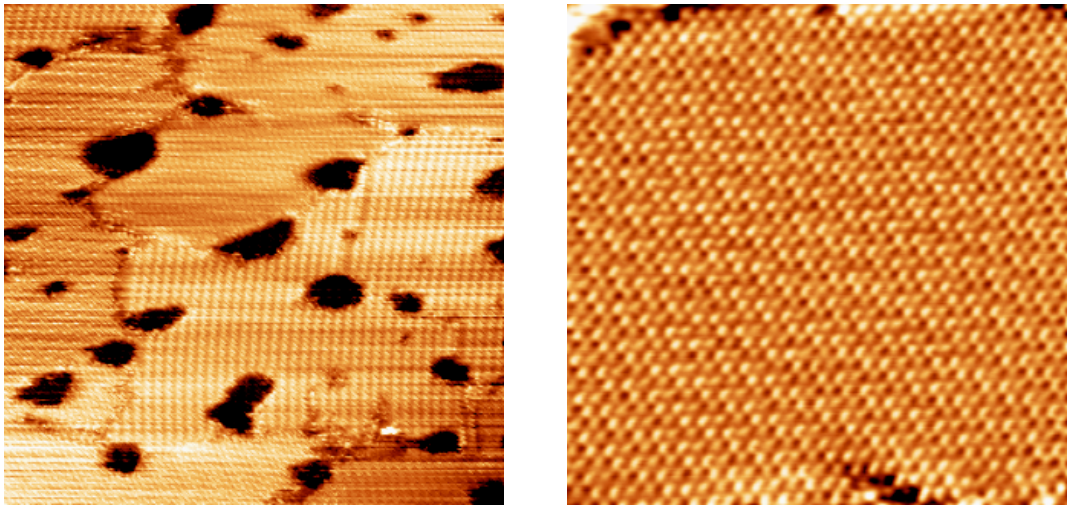

(a) **(b)**

Figure 5.2: STM images of C10SH monolayer taken after ~4 hours exposure to hexadecane: (a) 50 nm × 50 nm topographic image (b) 15 nm × 15 nm topographic image. Tunneling conditions: V_{sample} = -1.0V, i_t=2 pA.

Similarly, in OMCTS, the SAM was found to be stable and no change in structure was observed after 4 to 5 hours exposure to OMCTS (Fig. 5.3 & 5.4).

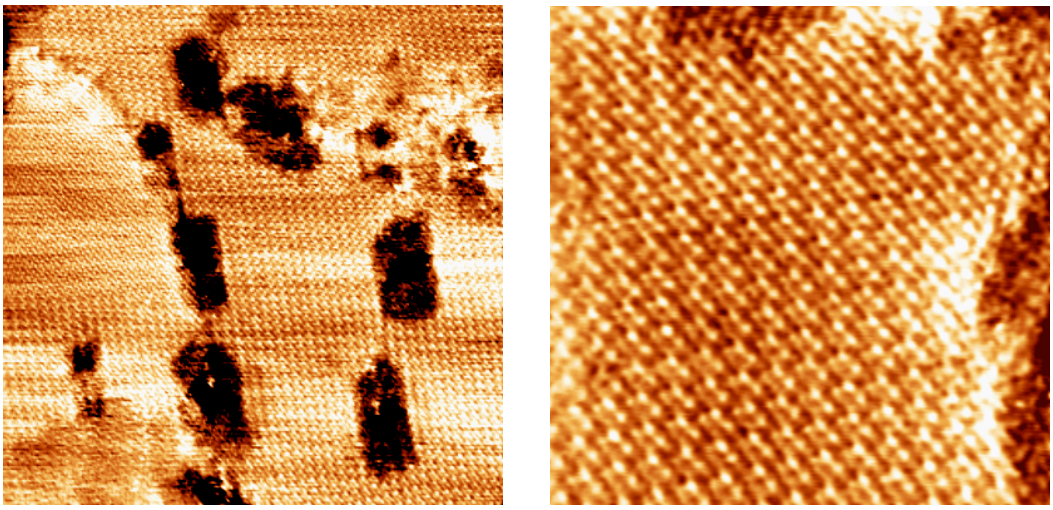

(a) **(b)**

Figure 5.3: STM images of C10SH monolayer in OMCTS, taken almost immediately after removing the sample from the alkanethiol solution: (a) 50 nm × 50 nm topographic image (b) 15 nm × 15 nm topographic image. Tunneling conditions: V_{sample} = -1.0V, i_t=2 pA.

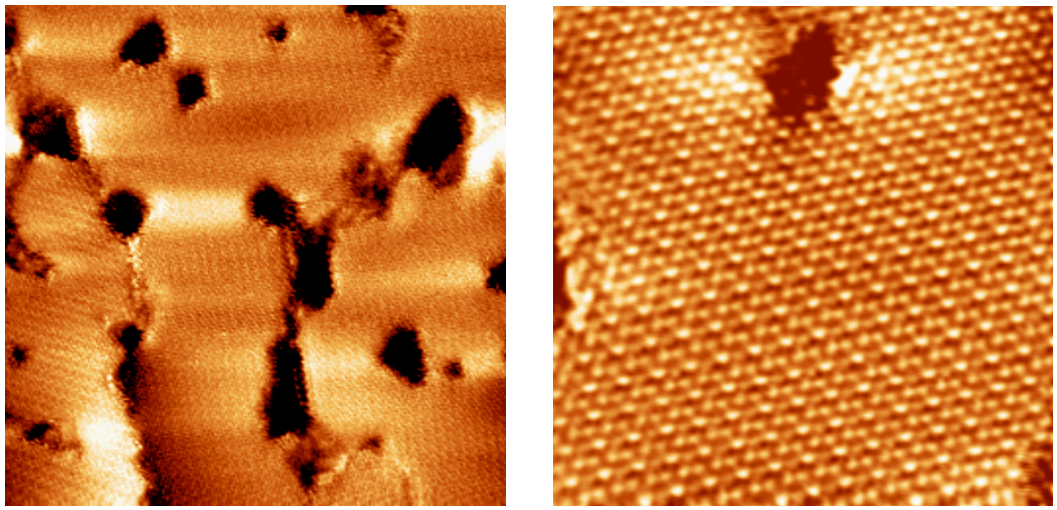

(a) **(b)**

Figure 5.4: STM images of C10SH monolayer taken after ~4 hours exposure to OMCTS: (a) 50 nm × 50 nm topographic image (b) 15 nm × 15 nm topographic image. Tunneling conditions: V_{sample} = -1.0V, i_t=2 pA.

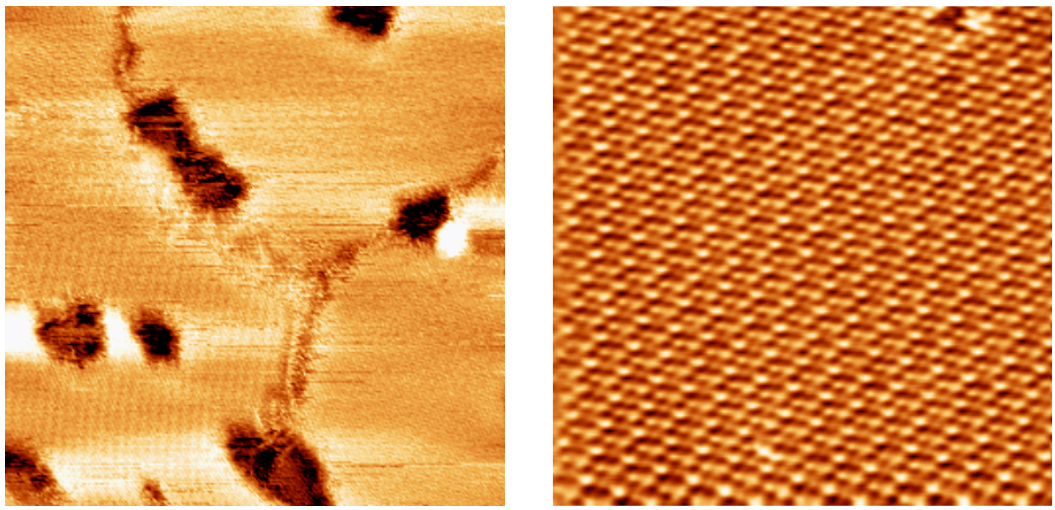

(a) **(b)**

Figure 5.5: STM images of C10SH monolayer taken in air, taken almost immediately after removing the sample from the alkanethiol solution: (a) 50 nm × 50 nm topographic image (b) 15 nm × 15 nm topographic image. Tunneling conditions: V_{sample} = -1.0V, i_t=3 pA.

STM imaging of the SAM was performed under ambient conditions (air, relative humidity of ~65%). No observable change in the SAM structure over several hours was noticed (Fig. 5.5 & 5.6).

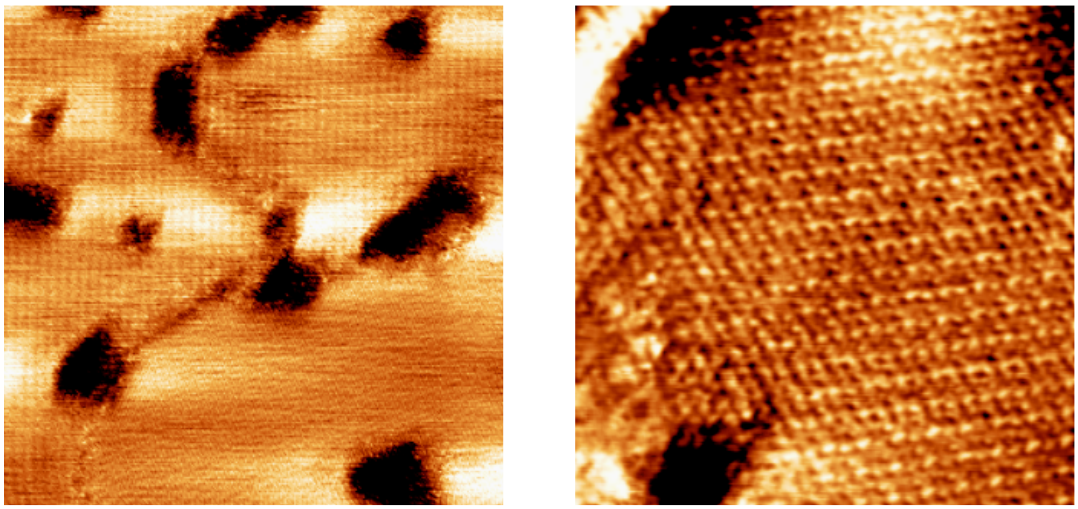

(a) **(b)**

Figure 5.6: STM images of C10SH monolayer taken after ~4 hours exposure to OMCTS: (a) 50 nm × 50 nm topographic image (b) 15 nm × 15 nm topographic image. Tunneling conditions: V_{sample} = -1.0V, i_t=2 pA.

5.2 Measurement of Solvation Forces on n-decanethiol SAM: Static Mode AFM

5.2.1 Measurements in OMCTS

The measurements in OMCTS clearly reveal several solvation layers of OMCTS molecules close to the SAM surface. Fig. 5.7 shows ~5 solvation layers with spacing of ~0.9 nm, consistent with the molecular diameter of OMCTS. It is striking to observe that the solvation layering of OMCTS on a SAM surface is as strong as observed on an atomically flat HOPG surface [63]. Presumably the surface corrugation (i.e. molecular roughness) is not high enough to perturb the layering of a molecule as large as OMCTS

(~0.9 nm diameter). The retraction force curve shows adhesion of the probe with the SAM surface and the measured pull off force is ~ 1.5 nN.

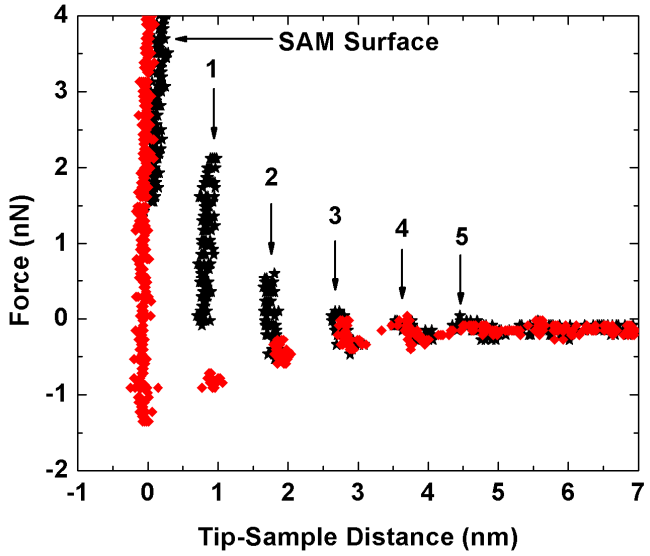

Figure 5.7: Discrete solvation layering of OMCTS as the tip approaches a C10SH SAM. Solvation jump distances of ~0.9 nm were observed corresponding to the diameter of the OMCTS molecule. The tip contacts the SAM at D=0 nm. The solvation layers are labeled n=1-5.

5.2.2 Measurements in Hexadecane

Measurements in Hexadecane also clearly reveal several solvation layers close to the SAM surface. Fig 5.8 shows ~3 solvation layers with spacing of ~0.5 nm, consistent with the molecular diameter of Hexadecane molecules. The retraction force curve shows adhesion of the probe with the SAM surface and the measured pull off force is ~ 0.8 nN. The strength of solvation layers is comparable to that of OMCTS but much weaker than that on a HOPG surface. There are two possibilities for the weaker ordering which cannot be distinguished from the present data. Firstly, the HOPG surface is particularly suited to

the formation of ordered monolayers of linear alkanes. This ordered monolayer (n=1) requires considerable force to squeeze-out and may induce further order in the higher (n=2, 3) solvation layers. A second explanation is that the molecular roughness of the SAM disrupts the formation of solvation layers [44] .

The approach and the retraction curves reveal kinks in the force curves which do not correspond to the diameter of the hexadecane molecules. In Fig 5.8, the force data shows a kink of ~0.1 nm in the approach curve (labeled A) and ~0.3 nm in the retraction curve (labeled B). These smaller jumps or kinks can be attributed to the yielding of the SAM under pressure. A detailed analysis of this observation is presented in Section 5.5.

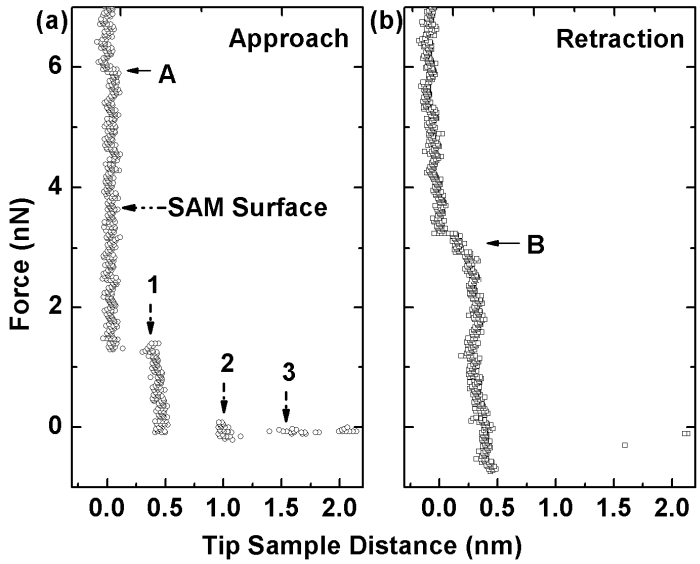

Figure 5.8: Force curve measured in hexadecane on C10SH SAM, revealing discrete layering of hexadecane as the tip approaches the surface. The approach (a) and retraction (b) curves are separated for clarity. Jump distances of ~0.5 nm were observed in the approach curve, corresponding to the diameter of the hexadecane molecule. A pull off force of ~ 0.8 nN is measured. The tip contacts the SAM at D=0 nm. The kinks labeled A and B show small deformations of the SAM under load.

5.3 Measurements on n-decanethiol SAM: Sample Modulation-AFM

Sample modulation AFM (SM-AFM) can also be used in order to provide additional information on force interactions in liquid [63, 133]. As discussed in the following sections, SM-AFM has higher sensitivity for measurement of weak solvation forces. This technique also overcomes the instability problem (i.e. snap in) in the attractive regime with static measurements and a full force interaction profile can be obtained, including the attractive regime, while traversing through the solvation layers. The amplitude variation of the oscillating cantilever while interacting with the solvation layers and the underlying substrates gives a direct measure of the interaction stiffness (Section 3.1.3).

All the SM-AFM data was taken using stiff Si cantilevers (k_c ~40 N/m) and at small amplitudes of sample oscillation (2 $Å_{peak\text{-}to\text{-}peak}$).

5.3.1 Measurements in OMCTS

Fig 5.9 shows the simultaneous static deflection of the cantilever and the SM-AFM amplitude measured with force in OMCTS on a C10SH SAM surface. Five to six solvation layers are clearly visible in the amplitude signal, whereas the static deflection curve shows only 3 layers. The change in amplitude of the cantilever gives a quantitative measure of interaction stiffness of the tip-SAM contact which is discussed in detail in Section 5.3.4 and [63, 133]. The major point of interest for this data is that significant solvation layering occurs even when one of the surfaces (C10SH) is rough at a molecular scale.

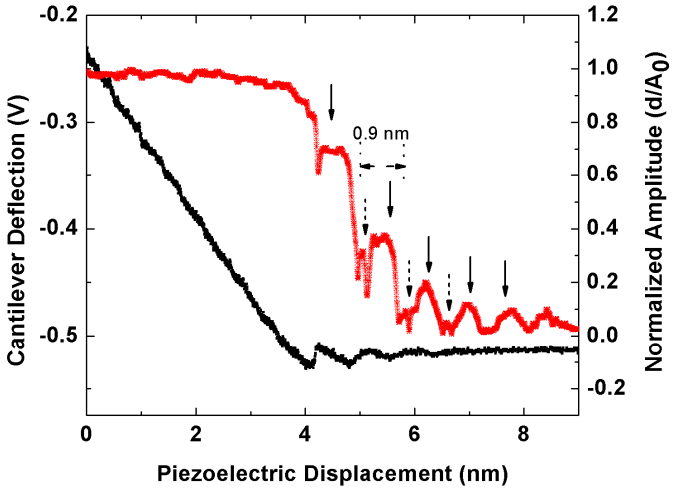

Figure 5.9: Raw data (pull off curve) showing cantilever deflection and cantilever amplitude (normalized) taken in OMCTS on C10SH SAM with a Si cantilever (k_c=40 N/m). The sample was modulated using a piezotransducer with peak-to-peak amplitude (A_1) of ~2 Å. Vertical continuous arrows indicate individual solvation layers of OMCTS. The dashed arrows show the periodicity doubling effect arising from interactions in the attractive regime [63].

5.3.2 Measurements in Hexadecane

In hexadecane we also observe discrete solvation layering close to the SAM surface using SM-AFM which is barely resolved in the static deflection signal (Fig. 5.10). The layer periodicity is ~0.5 nm, indicating that the hexadecane has it's long axis parallel to the surface. The normalized cantilever amplitude in contact with the SAM surface is smaller than the OMCTS data, suggesting a lower interaction stiffness of the SAM in Hexadecane. This is indeed the case and the stiffness and yielding of the SAM is discussed in detail in Sections 5.3.4 and 5.5.

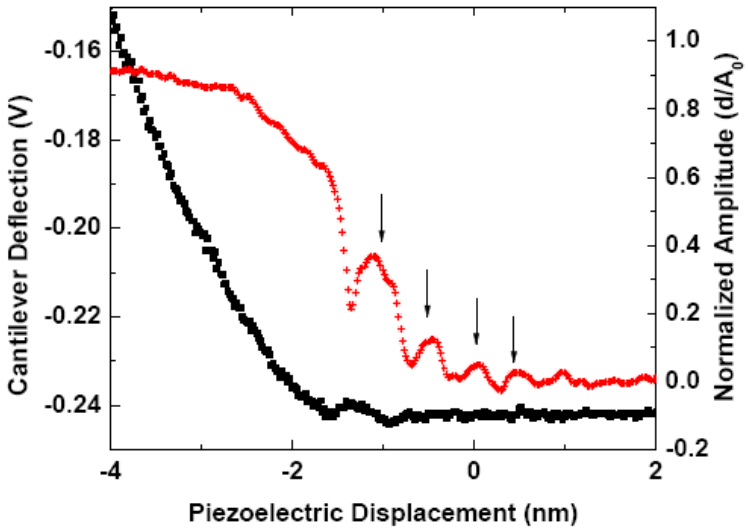

Figure 5.10: Raw data (pull off curve) showing cantilever deflection and cantilever amplitude (normalized) taken in Hexadecane on C10SH SAM with a Si cantilever (k_c=40N/m). The sample was modulated using a piezotransducer with a peak-to-peak amplitude (A_1) of ~2 Å. Vertical arrows indicate individual solvation layer of hexadecane.

5.3.3 Measurements in Air

Fig. 5.11 shows cantilever static deflection and SM-AFM amplitude data taken in air on pull off. There is a long range attractive force, which is presumably due to capillary effects. Note that this data is obtained with a stiff cantilever (k_c= 40 N/m) so there is no "jump off" of the contact. The force varies smoothly between the attractive and repulsive region. The adhesion minimum is ~-50 nN. The SM-AFM amplitude measures the *gradient* of the force. Hence there is a sharp change in amplitude at the turning point of the force curve (indicated by an arrow in Fig. 5.11), not at the adhesion minima.

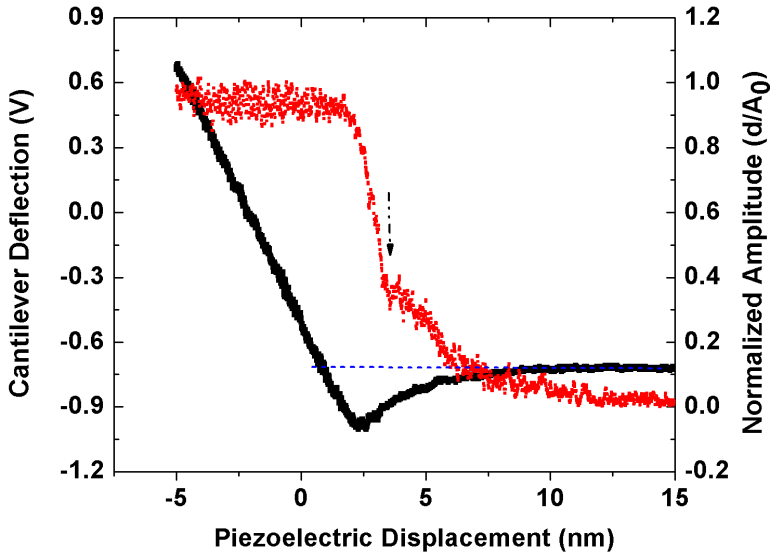

Figure 5.11: Raw data (pull off curve) showing cantilever deflection and SM-AFM amplitude (normalized) taken in air with a Si cantilever (k_c=40 N/m). The sample was modulated using a piezotransducer with peak-to-peak amplitude (A_1) of ~2 Å. The vertical arrow indicates the turning point of the force curve.

5.3.4 Measurement of Interaction Stiffness of the SAM

Of major interest in this work is to understand the mechanical behavior of the tip-SAM interaction (or contact) stiffness in the various surrounding media. Data such as Fig. 5.9-5.11 can be used to obtain contact stiffness (k_i) using Eqn. 3.9. We use the SM-AFM data obtained from the retraction of the tip from the surface. In this way, we are certain that all the solvation layers have been removed from the tip-sample gap and the tip is in hard contact with the SAM surface.

Fig. 5.12 shows the variation of stiffness of the SAM with applied force in air and liquids (OMCT, hexadecane). The contact stiffness measured in air or OMCTS show almost identical values. The contact stiffness measured in hexadecane is significantly smaller in magnitude in comparison to OMCTS and air. These results confirm that hexadecane

causes a softening of the SAM i.e. reduction in contact stiffness. The decrease in SAM stiffness has important consequences in the measurement of the resistance of the SAM, as will be discussed in Section 5.4. The reason behind these observations (Fig. 5.12) could be the higher mobility (i.e. fluidity) of the terminal methyl groups of the SAM molecules interacting with the hexadecane molecules, which may lead to easier deformation on the application of force. Simulations and experiments have shown that SAM molecules can deform near the end groups, even at low applied pressures, and the deformation increases and reaches a limiting value at higher pressure due to the stiffer backbone of the molecules closer to the underlying substrate [196-199].

The weak influence of OMCTS on the SAM may arise from the intrinsically poor solubility of alkanethiol in OMCTS or the larger size of the OMCTS molecule, either of which lessens the probability of the liquid solvating the SAM layer.

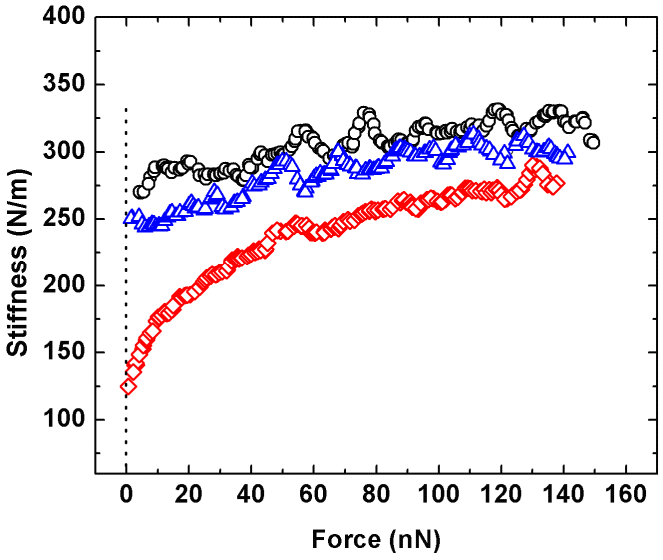

Figure 5.12: Variation of the contact stiffness with force for a C10SH SAM measured using sample modulation AFM with a Si probe. The stiffness variation during unloading is shown for measurements in hexadecane (□), air (Δ) and OMCTS (○).

5.4 Conducting AFM Measurements

5.4.1 Current-Voltage (I-V) Measurements

To measure the resistance of the C10SH SAM, current-voltage (I-V) measurements were undertaken using C-AFM with the tip in contact with the SAM surface. This was done as a function of the applied force in air and liquid (OMCTS and hexadecane). For the I-V measurements, the samples were first imaged at very low normal force (~1.0 nN) to find flat Au(111) terraces on which experiments were undertaken. Subsequently, two basic experiments are done, namely I-V curves and current vs. force spectroscopy.

For I-V measurement the applied force was held constant, the voltage linearly ramped from -0.5 to +0.5 V, and the current was recorded. About 30 to 40 I-V curves were recorded with each tip at different locations on a terrace and at different normal force. I-V curves on the SAM were found to be symmetric and linear over this voltage range allowing the contact resistance to be found from the slope of the curve at low bias. For example, Fig. 5.13 shows data for I-V curves obtained at different normal loads in OMCTS.

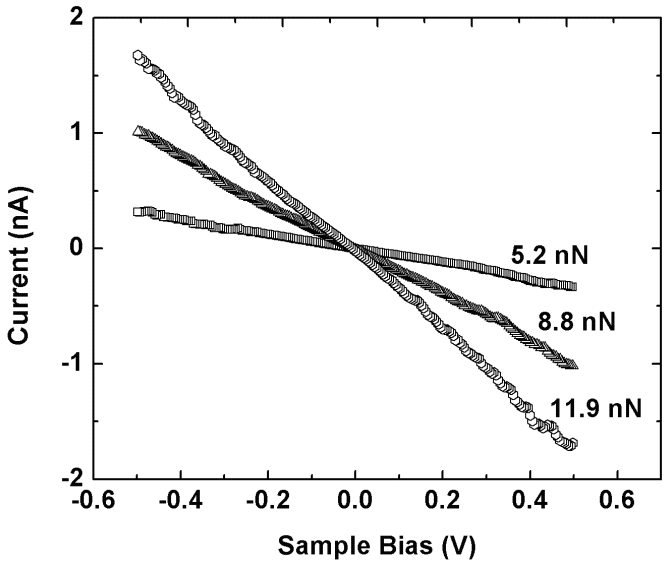

Figure 5.13: I-V curves taken on C10SH SAM on Au(111) in OMCTS at three different forces. The curves are linear and symmetrical over the low voltage range used. Contact resistance is calculated from the slope of the curves.

The low bias I-V curves are linear for all the systems studied and the contact resistance thus provides an easily available parameter for comparative purposes. Fig. 5.14 a, b and c show variation of contact resistance with load in hexadecane, OMCTS and air. The resistance measured from the I-V curve is normalized by dividing by the tip-sample contact area (in nm^2) which is found for each experiment using continuum mechanics models (see Section 5.5). There is significantly higher decrease in contact resistance with load in hexadecane in comparison to OMCTS and air. In hexadecane the contact resistance for every tip decreases by ~ two orders of magnitude with increase in applied load. In OMCTS and air, the decrement is less than ~ one order of magnitude, with half of the tips showing very small decrease (a factor of ~ 3).

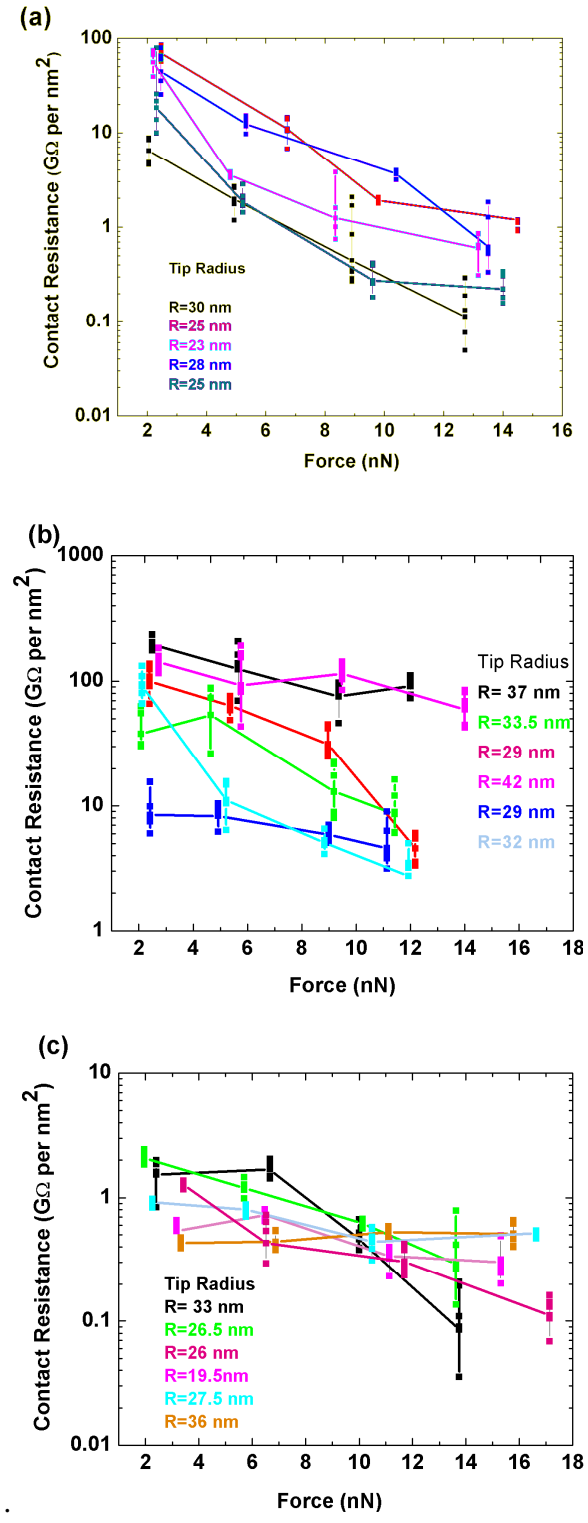

Figure 5.14 (a) Data showing Au-SAM contact resistance vs. applied force measured with different Au coated cantilevers taken in (a) hexadecane (b) OMCTS, (c) Air.

The data of Fig 5.14 are taken with essentially the same tip radius (the radius of the tip only varies from 20 to 42 nm), yet the scatter in the data is high for nominally identical experiments. This is certainly due to unknown tip-sample contact geometry at the atomic scale (i.e. molecular roughness), making the DMT model predictions overly simplistic. Nevertheless the data trend is clear. At low loads (2nN) the contact resistance is tightly grouped around 1.2±0.8 GΩ per nm^2 for air and 130±90 GΩ per nm^2 for OMCTS. The contact resistance in hexadecane has a broader distribution, from ~7 to 70 GΩ per nm2. Fig. 5.15 shows the average contact resistance values obtained from the I-V measurements in OMCTS, hexadecane and in air. There are two important observations namely; a) within error, there is minimal difference in contact resistance at low applied force (2 nN) in both of the liquids. However we observe a much lower contact resistance in air even at very low applied forces. b) At higher forces, the contact resistance decreases sharply in hexadecane in comparison to OMCTS and progressively becomes closer to the value observed in air as the force increases. The contact resistance in OMCTS decreases with increasing applied force but always differs by more than an order of magnitude compared to data taken in air. These results can be explained by the change in the stiffness of the SAM in the different media. In OMCTS, the SAM remains stiff and undergoes only elastic deformation. In hexadecane, the SAM is mechanically softer and can undergo plastic deformation (see Section 5.4.2.2).

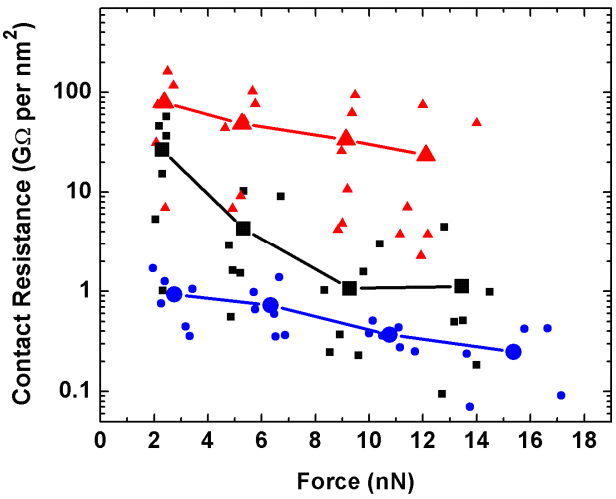

Figure 5.15: Contact resistance of C10SH measured by C-AFM in Air (●), Hexadecane (■) and OMCTS (▲) as a function of applied normal force. The bigger symbols (circles, squares and triangles) are the average of all the measurements for each surrounding medium. The smaller symbols are average of measurements for individual tips for each surrounding medium.

5.4.2 Current vs. Force Spectroscopy

We now tie up the previous sections on SAM stiffness, solvation and contact resistance by discussing the current vs. force data measured on the C10SH SAM in the various mediums.

5.4.2.1 OMCTS

Fig. 5.16a shows a current vs. force measurement of C10SH SAM taken in OMCTS. Fig. 5.16b shows the corresponding force as a function of tip-sample distance (D). Clear solvation layers of OMCTS liquid are observed and the tip only contacts the SAM surface (D=0) above a normal force of ~1.25 nN. A measurable current was observed

only on the SAM surface i.e. only after all the OMCTS was squeezed out. No current was measurable (at 1 pA sensitivity) when the tip was within the first solvation layer (D ≈ 0.9 nm). Thus the solvation layers have no influence on the measured SAM resistance.

We now consider the tip-SAM contact (D=0). During approach and retraction of the probe when in contact with the SAM, the current follows almost the same path (Fig. 5.16a) and the hysteresis is negligible. This indicates that the deformation of the SAM under the probe is elastic in OMCTS. It is widely accepted that the current flow across an alkanethiol SAM at constant voltage has two components, chain to chain coupling and a through-bond component [125, 195, 200].

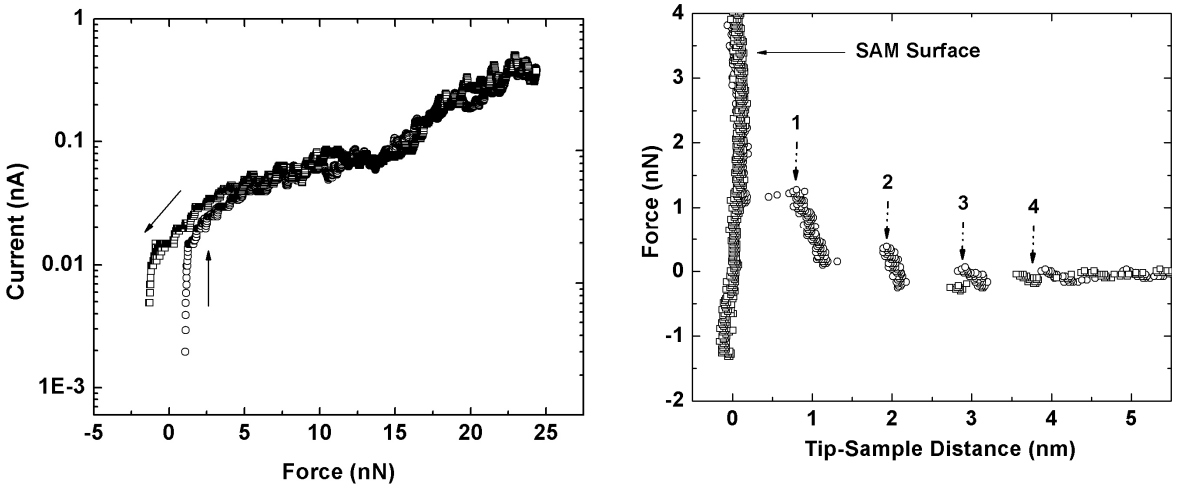

Figure 5.16: (a) Current vs. force curve for C10SH taken in OMCTS with sample at fixed bias of 1.0 V. The approach (○) and retraction (□) curves do not show significant hysteresis in the measured current. A pull off force of ~ 1.4 nN is measured. (b) Simultaneously measured force curve revealing discrete solvation layering of OMCTS as the tip approaches the surface. Jump distances of ~0.9 nm were observed corresponding to the diameter of the OMCTS molecule. The tip contacts the SAM at D=0 nm.

When the SAM is compressed, only the chain to chain tunneling component varies due to the increase in tilt angle of the SAM molecules with respect to the surface normal. Thus the current flow at constant voltage is dependent on two main parameters; the contact area of the junction (which varies with applied force) and the gap between the Au tip and the Au(111) substrate which varies the tilt and hence intermolecular tunneling between the SAM molecules. In OMCTS, both the contact area and SAM deformation, both of which can be calculated from the current vs. force curve, vary with force as expected for an elastic contact (this statement is quantified in Section 5.5).

5.4.2.2 Hexadecane

Fig. 5.17a shows a current vs. force curve on C10SH in hexadecane and Fig. 5.17b shows the corresponding force vs. distance curve (this is Fig. 5.8, repeated here for clarity). The confined hexadecane forms solvation layers near the SAM. A small but measurable current only occurs when the probe contacts the SAM surface, after squeezing out all the hexadecane solvation layers. Thus, as for OMCTS, the solvation layers have no effect on the measured current at 1 pA resolution (corresponding to a resistance of 1TΩ).

We now consider the tip-SAM contact (D=0). The contact resistance in hexadecane shows a complicated variation with force and significant hysteresis. A small current flows up to a threshold force (5-6nN), beyond which the current shows a sharp rise (shown by arrow A; Fig. 5.17a). Retraction of the tip shows higher values of current compared to the approach curve for the same applied force and the current drops sharply below a certain force (~ 3 nN, shown by arrow B).

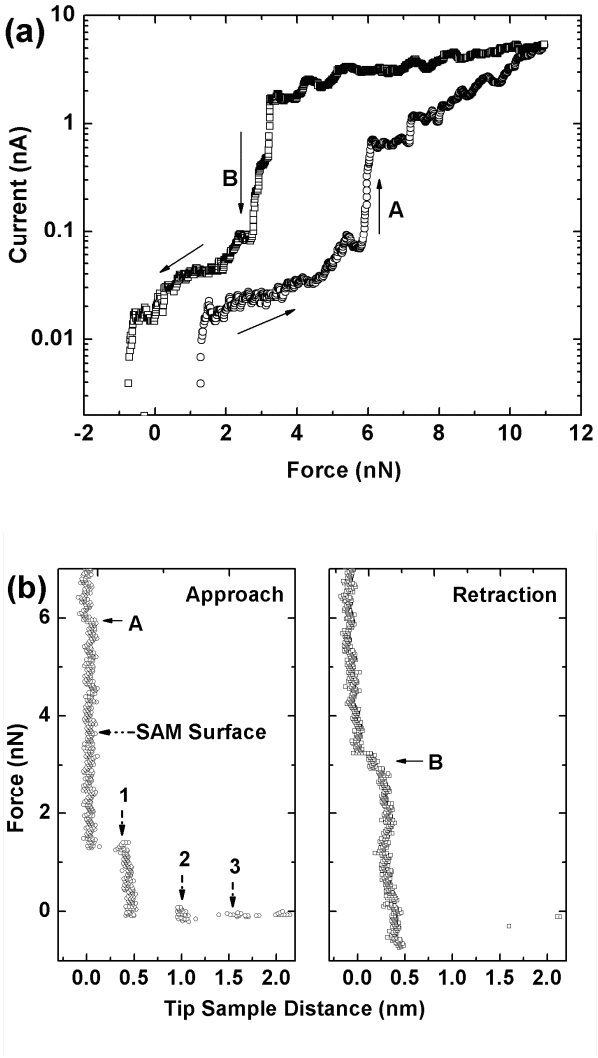

Figure 5.17: (a) Current vs force curve for C10SH taken in hexadecane with sample at fixed bias of 1.0 V. The current variation with force during approach (○) shows a sharp rise in current corresponding to the kink observed in the force curve (marked with arrow A). During retraction (□) there is also a sharp decrease in current corresponding to a kink observed in the force curve (marked with arrow B). Significant hysteresis is observed in the measured current. (b) Simultaneously measured force curve revealing discrete solvation layers of hexadecane as the tip approaches the surface. The approach and retraction curves are separated for clarity. Jump distances of ~0.5 nm were observed in the approach curve, corresponding to the diameter of the hexadecane molecule. The tip contacts the SAM at D=0.

This behavior is repeatable and probably indicates a sudden change in conformation of the SAM above a critical force. Similar observations have been previously reported [183,

201]. Associated with the sudden changes in current are small kinks in the force curve (labeled A and B, Fig. 5.17b). The kinks are similar to pop-in and pop-out events observed in nano-indentation experiments, suggesting that they might be linked to yielding or the formation of gauche defects in the SAM at certain critical force [201]. The kink at arrow A gives a current increase by a factor of ~8 and the current decrease at arrow B is by a factor of ~20. From the tunneling equation, which is valid for conduction across the SAM, we can write the current (i_t) at fixed voltage as (see Eqn. 2.23),

$$i_t \propto \exp(-\beta.s) \tag{5.1}$$

where β is the decay factor and s is the thickness of the SAM. Note that the major change in current flow with applied force arises from changes in intermolecular distance i.e. tilt. The tilt varies the distance between SAM molecules and hence the through-space tunnel current flow. The variation of tunnel current with deformation of the SAM is related through the parameter β. We can find the expected change in current from the measured decrease in SAM thickness (Δs) at the kinks in Fig. 5.16b ($\Delta s \approx 1$ Å during approach, $\Delta s \approx 3$ Å during retraction). Using β=0.9 Å^{-1} [200] we estimate the increase in current at arrow A during approach as a factor of ~3 and decay in current at arrow B during retraction as a factor of ~15, in approximate agreement with our observations. The larger jump distance of the kink during the retraction curve can be an indication of reversibility of the compressed SAM molecules [201, 202], which seems feasible as the current falls to almost the same value as that observed during the approach cycle (≈ 20 pA). The large hysteresis and the presence of the kinks indicate that some plastic deformation occurs on

loading. This is not surprising given that the SAM has been "softened" by exposure to the hexadecane environment, as shown explicitly in the SM-AFM stiffness data (Fig. 5.12).

5.4.2.3 Air

Fig. 5.18 shows the current vs. force measurements of C10SH SAM taken in ambient air. Much higher currents (i.e. lower contact resistance) are observed in air compared to liquid media even at very low applied loads which can be attributed to the strong adhesive forces (≈ 7 nN) acting between the probe and the SAM surface leading to higher deformation of the SAM from high stress near the periphery of the contact. The current remains high (≥1nA) in air even during the retraction cycle of the force curve and shows significant hysteresis in the measured current during approach and retraction of the tip. This indicates that plastic deformation is occurring during the loading cycle. Similar conclusions have recently been made in the measurement of conductance of C10SH SAM in air occurs due to plastic deformation of the SAM [200] .

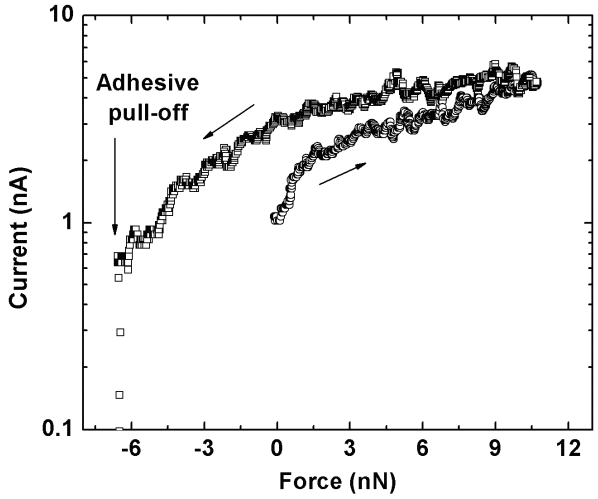

Figure 5.18: Current vs. force curve for C10SH taken in air with sample at fixed bias of 0.5 V. The approach (○) and retraction (□) curves show hysteresis in the measured current and a pull off force of ~ 7.0 nN is observed.

5.5 Determination of SAM Deformation

It is evident that the electrical measurements are strongly dependent on the mechanical properties of the junction, and we now consider the force curves in more detail. We introduce the contact resistance (R) of the junction, per unit area, given as [200]:

$$R = \frac{R_0}{\pi \cdot a^2} \exp(\beta.s) \approx \frac{R_0}{\pi \cdot a^2} \exp\left(\beta\left(\delta_{SAM} - \left(\delta_e + \delta_p\right)\right)\right) \tag{5.2}$$

where δ_{SAM} is the undeformed SAM thickness, δ_p is the SAM plastic deformation and δ_e is the SAM elastic deformation. R_0 is the resistance of the molecule-metal contact. For elastic deformation, the DMT model can be applied to calculate the contact area ($\pi.a^2$) and elastic deformation (δ_e) of the junction as [7]:

$$a = \left\{\frac{3r}{4K}\left(F_a + F_c\right)\right\}^{1/3} \tag{5.3}$$

$$\delta_e = \frac{a^2}{r} = \frac{1}{r^{1/3}}\left(\frac{3\left(F_a + F_c\right)}{4K}\right)^{2/3} \tag{5.4}$$

where a is the contact radius, r is the tip radius of curvature, K is the effective elastic modulus, F_a is the applied normal force and F_c is the pull off force. We use an effective modulus of K= 48 GPa for the C10SH-Au contact [200]. The normalization of the resistance to the elastic contact area is very useful for comparison of the measured resistance at low forces, but is clearly only a crude approximation of area if plastic deformation occurs. The I-V data previously reported in Section 5.4.1 was normalized using Eqn. 5.3.

Accounting for plastic deformation is less straightforward. It is difficult to analyze the plastic deformation in the hexadecane system because of the presence of the large kinks in the data (Fig. 5.17a). However, the Au-SAM-Au junction also undergoes plastic deformation in air and for this data (Fig. 5.18), the current vs. force curve is continuous. To analyse we follow a reported formalism [200] to estimate the plastic deformation (δ_p) of the junction by defining the hysteresis ratio (H) as the ratio of the unloading current to the loading current at a given force. The hysteresis ratio is a function of total force F, $\left(F = F_a + F_c\right)$ and for tunneling conduction across an alkane SAM we can write,

$$H \equiv \frac{i_{unloading}(F)}{i_{loading}(F)} \approx \exp\left(\beta\left(\delta_p(F_{\max}) - \delta_p\left(F\right)\right)\right) \tag{5.5}$$

where $F_{\max}$ is the maximum *total* force, F_a is the applied force and F_c is the adhesive force. The plastic deformation can be described by a power law as,

$$\delta_p\left(F_{\max}\right) \equiv bF_{\max}^{n} \equiv \delta_p \tag{5.6}$$

where b and n are constants. Hence Eqn. 5.5 can be written as,

$$H \approx \exp\left(\beta.b\left(F_{\max}^{n} - F^{n}\right)\right) \tag{5.7}$$

Fig. 5.19a shows fitting of the hysteresis ratio vs. total force curve (solid line) with b and n allowed to vary freely. For this data the parameters are $\beta = 0.9$ Å^{-1}, F_{max} ~ 17 nN, b=1 and n=0.38. The fitting parameters allow one to calculate the plastic deformation after the application of some maximum force (F_{max}) using Eqn 5.7. For the data of Fig. 5.18, a value of δ_p=2.9 Å is found after F_{max} ~17 nN is applied. It is useful to view the indentation data graphically, as shown in Fig. 5.19b. The indentation in air shows a

permanent plastic deformation (δ_p). The OMCTS data also shows deformation, but this is purely elastic.

For completeness, the indentation (δ) of the SAM is calculated as [200],

On loading: $$\delta = \delta_p(F) + \delta_e = b.F^n + \frac{K}{K_{SAM}}\left(\frac{9}{16}R\right)^{1/3}\left(\frac{1}{K}\right)^{2/3}F^{2/3} \quad (5.8)$$

On unloading: $$\delta = \delta_p(F_{\max}) + \delta_e = \delta_p + \frac{K}{K_{SAM}}\left(\frac{9}{16}R\right)^{1/3}\left(\frac{1}{K}\right)^{2/3}F^{2/3} \quad (5.9)$$

where K is the effective elastic modulus of the Au-SAM contact (48 GPa) and K_{SAM} is the SAM modulus (38 GPa). Eqns. 5.8 and 5.9 are valid for a DMT or Hertz model of the elastic deformation.

The data taken in air shows that after unloading there remains a permanent deformation δ_p of the contact. We found the average SAM plastic deformation for all the data taken in air to be ~ 3.3 ± 0.8 Å at the maximum forces of ~20 nN. Note that the maximum force is a *total* force (i.e. the applied force plus the adhesive force). It is the plastic deformation that gives rise to low contact resistance in air because the SAM thickness is considerably reduced (3.3 ± 0.8 Å) by indentation of the tip into the SAM.

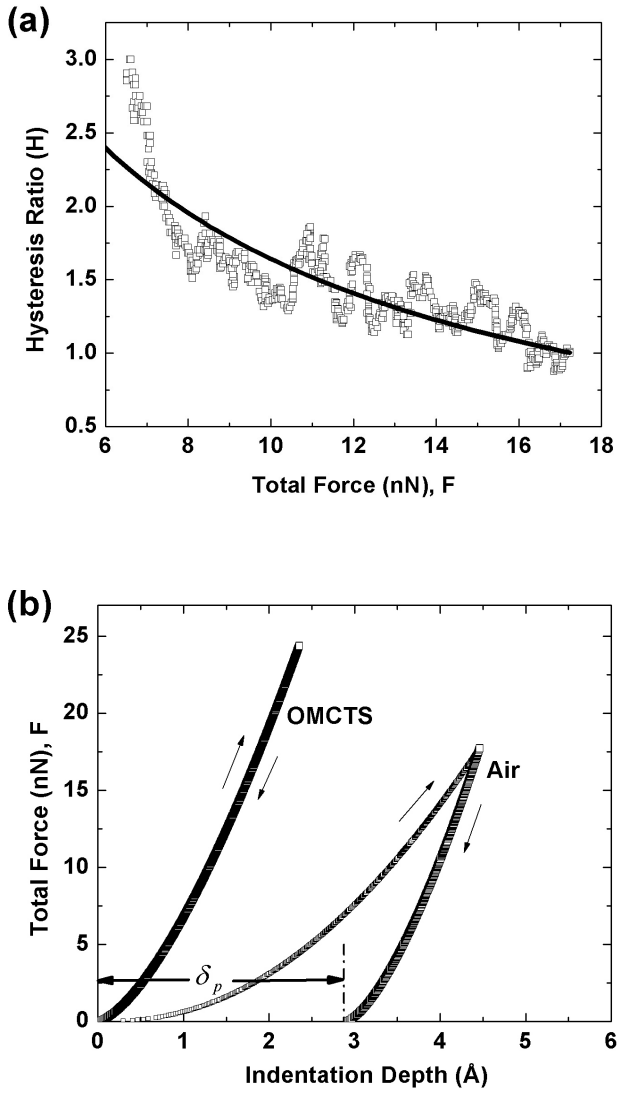

Figure 5.19: (a) Hysteresis ratio vs. total force (F), plotted for the data of Fig. 5.18 (C10SH taken in air). The solid line shows the data fitted with a power law equation to estimate the plastic deformation. (b) Calculated indentation for C10SH in OMCTS and Air. The indentation in OMCTS is elastic, whereas in air there is a plastic component of the SAM deformation (δ_p). In this example, for the data of Fig. 5.18 and 5.19a, we find δ_p=2.9 Å. Note that the total force $F=F_a + F_c$.

5.6 Summary

Conduction through an alkanethiol (C10SH) monolayer on Au(111) is measured at low applied forces using Au coated C-AFM probes in air and in liquids (OMCTS and hexadecane). Liquid layering near the SAM surface was observed, but this does not influence the measured contact resistance when the tip contacts the SAM surface. The surrounding media does, however, influence the measured molecular resistance by changing the mechanical response of the SAM. Variation by orders of magnitude in the measured resistance can arise at the same applied force, as verified using current vs. force measurements. Significant plastic deformation of the SAM occurs in air and above a critical force in hexadecane. However, in OMCTS, the SAM behaves elastically. We support these observations by measuring the contact stiffness of the junction in different liquids which reveals a much lower stiffness for the SAM in hexadecane, suggesting the SAM is easier to deform in comparison to experiments in OMCTS. This suggests a solvent dependent variation in interfacial properties of SAM, which affects the deformation behaviour of the SAM. Several spectroscopic studies have also shown that solvents can have dramatic influence on interfacial order of SAMs depending upon the extent of interaction of the solvent with the SAM molecules [203, 204].

The measurement of the conductivity of molecules with C-AFM does appear to be best done in liquid; at least for the class of experiments which do not have a chemical bond formed at both ends of the tip-molecule-metal contact e.g. dithiols. The measurements done in air have strong adhesive forces deforming the contact zone. However, even in a

liquid environment, for reproducible measurement of SAM resistance one should ensure there is little adhesion in the system chosen and measure at small applied forces. Moreover, current vs. force curves should be obtained to verify that the mechanical behavior of the contact is elastic at the forces used. Elastic behavior leads to two important benefits, namely; a) the contact area can be estimated using continuum mechanics models, enabling the current per unit area to be found, and b) to rule out changes in measured current flow arising from plastic deformations.

Chapter 6

Conclusions and Future Work

In this work solvation forces and contact mechanics between two approaching surfaces have been studied at the nanoscale using atomic force microscopy (AFM) in molecular liquids. A variety of inert and non-polar liquids such as spherical molecules (e.g. OMCTS), linear alkanes (e.g. hexadecane) and branched alkanes (e.g. squalane and 2,2,4,4,6,8,8-heptamethylnonane (HMN)) were studied on graphite and self assembled monolayer surfaces. In addition to simply measuring forces as in conventional AFM, experiments were also performed using conducting AFM in liquid where current through the probe is monitored. Such simultaneous force and conductivity measurements provide a more comprehensive understanding of subtle changes occurring within the contact zone.

The first experimental section (Chapter 4) detailed the behavior of the liquids on graphite. We find the squeezing of "solid-like" monolayers of linear alkanes (e.g. hexadecane) and the branched alkane, squalane, can be described by continuum mechanics models for an elastic solid. This is for the tip both in contact with the underlying substrate and within the solvation layers. The use of C-AFM shows that just before the squeeze-out of the monolayer there is a characteristic subtle rearrangement of the molecules under the tip apex, in agreement with recent computer simulations [165]. Moreover, the solid-like nature of the squalane monolayer on graphite is verified by direct imaging using STM. This is the first such imaging of a highly branched alkane and confirms simulations which have suggested that even highly branched molecules can exhibit very long range

order on adsorption [77]. The existence of this long range order has been controversial because previous approaches have all used diffraction based methods.

In contrast, 2,2,4,4,6,8,8-heptamethylnonane (HMN), a more densely branched alkane, remains disordered on the surface. Although both squalane and HMN are strongly branched alkanes, the disorder/order distinction in the state of the confined monolayer leads to striking differences in the solvation layering and squeeze-out behavior of the two molecules. Squeezing of HMN reveals significant variability in data due to its disordered state. Surprisingly, continuum elastic models cannot be applied to describe the contact, either on the monolayer or with the tip in contact with the graphite. We postulate that "liquid-like" HMN molecules always remain trapped within the tip-sample junction, even at very high applied loads, as suggested in a recent simulation showing trapping of molecules under a nanoscale confinement [99]. Molecular scale STM images of this disordered system could never be obtained.

The mechanism of trapping of the disordered molecules within the nanoscopic contacts was further confirmed by repeating the current vs. force measurements at elevated temperatures (above the monolayer melting temperatures of hexadecane and squalane) which changes the data from solid like behaviour (at low temperature) to that observed for disordered HMN molecules. Also, current vs. force measurements of short-chain alkanes (decane and dodecane), which do not form an ordered monolayer on graphite at room temperature, reveal similar behavior as HMN. Finally, experiments performed at much slower approach speed, which allows enough time for the confined molecules to

diffuse out of the contact zone, reveal elastic solid-solid contact. All the results suggest that the dynamics of the confined molecules between have significant implications in contact mechanics, particularly when one must now consider a new mechanism; molecule trapping.

In the second section (Chapter 5), surface forces in air, hexadecane and OMCTS on a self-assembled monolayer (SAM) surface were studied using C-AFM in order to understand the effects of liquids on measured contact resistance. This is an important issue for molecular electronics because a range of C-AFM studies conducted on simple monothiol SAM in various liquids and air have revealed orders of magnitude discrepancies in the measured contact resistance. We show that liquid solvation layering does occur near the SAM surface but this *does not* influence the measured contact resistance provided the tip contacts the SAM surface. The surrounding media *does* influence the measured resistance by changing the mechanical response of the SAM. Significant plastic deformation of the SAM occurs in air and above a critical force in hexadecane. However, in OMCTS, the SAM always behaves elastically and it is under elastic loading that reproducible results can be obtained. The observation of oscillatory solvation forces on SAM is also of fundamental interest as it shows that these surface forces may also occur on molecularly rough surfaces, opening the possibility of studying solvation forces and lubrication near individual molecules imbedded within a model SAM film.

The work presented in dissertation shows that various factors such as shape of molecules, temperature, speed of experiments etc. can have significant effect on solvation forces and squeeze-out behaviour of confined materials. This opens numerous possibilities to explore these systems with other AFM techniques and to study different systems of intent for tribology and biology. Dynamic mode AFM can be used to give information about the viscosity of the confined molecular liquids. Measuring the effect of molecular shape, temperature and speed of approach on viscosity with dynamic mode AFM will provide critical information on the timescales of the molecular motion and lead to a quantification of the terms "solid-like" and "liquid-like". It is also possible to combine conductivity measurements with dynamic mode AFM measurements to give additional information about the confined material, as demonstrated in this work. Conducting AFM would be more versatile if robust metallic tips were available. At present, only low voltages can be applied and scanning kept to a minimum. The fabrication of robust tips would enable, for example, the measurement of current flow in outer solvation layers by increasing the applied bias voltage. The current flow during scanning could also be measured and thus the current measured simultaneously with the friction forces acting on the point contact.

Applying the C-AFM and solvation force measurements to other systems is also of considerable interest. Using various SAMs it is possible to create a variety of interesting surfaces to understand effect of substrate properties on solvation forces. For example, molecular roughness can be created by mixing thiol molecules with different chain lengths or surface chemistry can be tuned by using thiol molecules with variety of end groups (-CH_3, -OH, -NH_2, -COOH etc.). The solvation forces and friction (viscosity) measured on such surfaces will probe confinement phenomena on a highly local scale.

Similarly, biomolecules such as proteins and DNA interact within solvents and their behaviour (e.g. folding, recognition) depends on forces in liquids acting over molecular length scales. The measurement of such forces is a key undertaking.

Bibliography

1. Bowden, F.P. and D. Tabor, The Friction and Lubrication of Solids, (Clarendon Oxford, 1950), Pt. 1.
2. Johnson, K.L., Contact Mechanics. (Cambridge University Press: Cambridge, UK, 1985).
3. Horn, R.G. and J.N. Israelachvili, *Direct Measurement of Structural Forces Between 2 Surfaces in a Non-Polar Liquid.* Journal of Chemical Physics, 1981. 75(3): p. 1400-1411.
4. Binnig, G., C.F. Quate, and C. Gerber, *Atomic Force Microscope.* Physical Review Letters, 1986. 56(9): p. 930-933.
5. Hertz, H. and J. Reine, *On the Contact of Elastic Solids.* Angew. Math., 1882. 92: p. 156.
6. Johnson, K.L., K. Kendall, and A.D. Roberts, *Surface Energy and the Contact of Elastic Solids.* Proc. R. Soc. London, Ser. A, 1971. 324: p. 301.
7. Derjaguin, B.V., V.M. Muller, and Y.P. Toporov, *Effect of Contact Deformations on the Adhesion of Particles.* J. Colloid Interface Sci., 1975. 53: p. 314.
8. B.V. Derjaguin, L.D. Landau, *Theory of Stability of Highly Charged Lyophobic Sols and Adhesion of Highly Charged Particles in Solutions of Electrolytes.* Acta Physicochim. URSS, 1941: p. 633.
9. E.J.W. Verwey, J.T.G. Overbeek, *Theory of the Stability of Lyophobic Colloids.* Elsevier Publishing Inc., 1948.
10. Israelachvili, J. N. (1992) *Intermolecular and Surface Forces* (Academic Press, New York).
11. Dzyaloshinskii, I.E., E.M. Lifshitz, and L.P. Pitaevskii, *The General Theory of van der Walls Forces.* Advances in Physics, 1961. 10: p. 165.
12. O'Shea, S.J., M.E. Welland, and T. Rayment, *Solvation Forces near a Graphite Surface Measured with an Atomic Force Microscope.* Applied Physics Letters, 1992. 60(19): p. 2356-2358.

13. Ducker, W.A., T.J. Senden, and R.M. Pashley, *Direct Measurement of Colloidal Forces using an Atomic Force Microscope.* Nature, 1991. 353(6341): p. 239-241.
14. Becker, T. and F. Mugele, *Nanofluidics: Viscous Dissipation in Layered Liquid Films.* Physical Review Letters, 2003. 91(16).
15. O'Shea, S.J., *Oscillatory Forces in Liquid Atomic Force Microscopy.* Japanese Journal of Applied Physics Part 1-Regular Papers Short Notes & Review Papers, 2001. 40(6B): p. 4309-4313.
16. Carpick, R.W. and M. Salmeron, *Scratching the Surface: Fundamental Investigations of Tribology with Atomic Force Microscopy.* Chemical Reviews, 1997. 97(4): p. 1163-1194.
17. Alonso, J.L. and W.H. Goldmann, *Feeling the Forces: Atomic Force Microscopy in Cell Biology.* Life Sciences, 2003. 72(23): p. 2553-2560.
18. Cui, X.D., et al., *Reproducible Measurement of Single-Molecule Conductivity.* Science, 2001. 294(5542): p. 571-574.
19. Hardy, W.B., *The Influence of Chemical Constitution upon Interfacial Tension.* Proceedings of the Royal Society of London. Series A, 1912. 86: p. 610.
20. Henniker, J.C., *The Depth of the Surface Zone of a Liquid.* Reviews of Modern Physics, 1949. 21: p. 322.
21. Taylor, A.M. and A. King, Nature, 1933. 132: p. 64.
22. McFaffie, I.R. and S. Lenher, Journal of Chemical Society, 1925. 127: p. 1559.
23. Boyes-Watson, J., E. Davidson, and M.F. Perutz, Proceedings of Royal Society of London A, 1947. 191: p. 83.
24. Brummage, K.G., Proceedings of Royal Society of London A, 1947. 191: p. 243.
25. Deryagin, B.V., G. Strakhovsky, and D. Malysheva, Acta Physicochim. U.R.S.S., 1944. 19: p. 541.
26. Bradley, R.S., Zeits. F. Krist., 1937. 96: p. 499.
27. Deryagin, B.V., M.M. Kusakov, and L. Lebedeva, Comptes Rendus U.R.S.S., 1939. 23: p. 671.
28. Deryagin, B.V., M.M. Kusakov, and L. Lebedeva, Acta Physicochim. U.R.S.S., 1939. 10: p. 25.

29. Christenson, H.K., *Non-DLVO Forces between Surfaces - Solvation, Hydration and Capillary Effects.* Journal of Dispersion Science and Technology, 1988. 9(2): p. 171-206.
30. Israelachvili, J. N., *Solvation Forces and Liquid Structure, as Probed by Direct Force Measurements.* Accounts of Chemical Research, 1987. 20(11): p. 415-421.
31. Israelachvili, J.N. and S.J. Kott, *Liquid Structuring at Solid Interfaces as Probed by Direct Force Measurements - The Transition from Simple to Complex Liquids and Polymer Fluids.* Journal of Chemical Physics, 1988. 88(11): p. 7162-7166.
32. Lee, C.S. and G. Belfort, *Changing Activity of Ribonuclease-A during Adsorption - A Molecular Explanation.* Proceedings of the National Academy of Sciences of the United States of America, 1989. 86(21): p. 8392-8396.
33. Parker, J.L. and H.K. Christenson, *Measurements of the Forces between a Metal-Surface and Mica across Liquids.* Journal of Chemical Physics, 1988. 88(12): p. 8013-8014.
34. Smith, C.P., et al., *Ultrathin Platinum Films on Mica and the Measurement of Forces at the Platinum-Water Interface.* Journal of Physical Chemistry, 1988. 92(1): p. 199-205.
35. Israelachvili, J.N., *Adhesion Forces between Surfaces in Liquids and Condensable Vapors.* Surface Science Reports, 1992. 14(3): p. 109-159.
36. Christenson, H.K., et al., *Structuring in Liquid Alkanes between Solid-Surfaces - Force Measurements and Mean-Field Theory.* Journal of Chemical Physics, 1987. 87(3): p. 1834-1841.
37. Horn, R.G., et al., *A Re-evaluation of Forces Measured across Thin Polymer-Films - Nonequilibrium and Pinning Effects.* Journal of Chemical Physics, 1989. 90(11): p. 6767-6774.
38. Horn, R.G. and J.N. Israelachvili, *Molecular-Organization and Viscosity of a Thin-Film of Molten Polymer between 2 Surfaces as Probed by Force Measurements.* Macromolecules, 1988. 21(9): p. 2836-2841.
39. Christenson, H.K., *Forces Between Solid-Surfaces in a Binary Mixture of Non-Polar Liquids.* Chemical Physics Letters, 1985. 118(5): p. 455-458.

40. Schoen, M., et al., *Shear Forces in Molecularly Thin-Films.* Science, 1989. 245(4923): p. 1223-1225.
41. Thompson, P.A. and M.O. Robbins, *Origin of Stick-Slip Motion in Boundary Lubrication.* Science, 1990, 250(4982): p. 792-794.
42. Landman, U., et al., *Atomistic Mechanisms and Dynamics of Adhesion, Nanoindentation, and Fracture.* Science, 1990. 248(4954): p. 454-461.
43. McGuiggan, P.M. and J.N. Israelachvili, *Adhesion and Short-Range Forces between Surfaces.2. Effects of Surface Lattice Mismatch.* Journal of Materials Research, 1990. 5(10): p. 2232-2243.
44. Gee, M.L. and J.N. Israelachvili, *Interactions of Surfactant Monolayers across Hydrocarbon Liquids.* Journal of the Chemical Society-Faraday Transactions, 1990. 86(24): p. 4049-4058.
45. Heuberger, M., M. Zach, and N.D. Spencer, *Density Fluctuations under Confinement: When is a Fluid not a Fluid?* Science, 2001. 292(5518): p. 905-908.
46. Mukhopadhyay, A., et al., *Contrasting Friction and Diffusion in Molecularly Thin Confined Films.* Physical Review Letters, 2002. 89(13).
47. Gee, M.L., et al., *Liquid to Solid-Like Transitions of Molecularly Thin-Films under Shear.* Journal of Chemical Physics, 1990. 93(3): p. 1895-1906.
48. Homola, A.M., et al., *Fundamental Experimental Studies in Tribology - The Transition from Interfacial Friction of Undamaged Molecularly Smooth Surfaces to Normal Friction with Wear.* Wear, 1990. 136(1): p. 65-83.
49. Vanalsten, J. and S. Granick, *Molecular Tribometry of Ultrathin Liquid-Films.* Physical Review Letters, 1988. 61(22): p. 2570-2573.
50. Homola, A.M., et al., *Measurements of and Relation between the Adhesion and Friction of 2 Surfaces Separated by Molecularly Thin Liquid-Films.* Journal of Tribology-Transactions of the ASME, 1989. 111(4): p. 675-682.
51. Demirel, A.L. and S. Granick, *Friction Fluctuations and Friction Memory in Stick-Slip Motion.* Physical Review Letters, 1996. 77(21): p. 4330-4333.
52. Demirel, A.L. and S. Granick, *Glasslike Transition of a Confined Simple Fluid.* Physical Review Letters, 1996. 77(11): p. 2261-2264.

53. Binnig, G., et al., *Tunneling through a Controllable Vacuum Gap.* Applied Physics Letters, 1982. 40(2): p. 178-180.

54. Banin, U. and O. Millo, *Tunneling and Optical Spectroscopy of Semiconductor Nanocrystals.* Annual Review of Physical Chemistry, 2003. 54: p. 465-492.

55. Besenbacher, F., *Scanning Tunneling Microscopy Studies of Metal Surfaces.* Reports on Progress in Physics, 1996. 59(12): p. 1737-1802.

56. Giancarlo, L.C. and G.W. Flynn, *Scanning Tunneling and Atomic Force Microscopy Probes of Self-Assembled, Physisorbed Monolayers: Peeking at the Peaks.* Annual Review of Physical Chemistry, 1998. 49: p. 297.

57. Frederix, P., et al., *Atomic Force Bio-Analytics.* Current Opinion in Chemical Biology, 2003. 7(5): p. 641-647.

58. Giessibl, F.J., *Advances in Atomic Force Microscopy.* Reviews of Modern Physics, 2003. 75(3): p. 949-983.

59. Fukuma, T., et al., *True Atomic Resolution in Liquid by Frequency-Modulation Atomic Force Microscopy.* Applied Physics Letters, 2005. 87(3).

60. O'Shea, S.J., M.E. Welland, and T. Rayment, *Atomic Force Microscope Study of Boundary-Layer Lubrication.* Applied Physics Letters, 1992. 61(18): p. 2240-2242.

61. Lim, L., Unpublished.

62. O'Shea, S.J., M.E. Welland, and J.B. Pethica, *Atomic-Force Microscopy of Local Compliance at Solid-Liquid Interfaces.* Chemical Physics Letters, 1994. 223(4): p. 336-340.

63. Lim, R., S.F.Y. Li, and S.J. O'Shea, *Solvation Forces using Sample-Modulation Atomic Force Microscopy.* Langmuir, 2002. 18(16): p. 6116-6124.

64. O'Shea, S.J. and M.E. Welland, *Atomic Force Microscopy at Solid-Liquid Interfaces.* Langmuir, 1998. 14(15): p. 4186-4197.

65. Maali, A., et al., *Oscillatory Dissipation of a Simple Confined Liquid.* Physical Review Letters, 2006. 96(8).

66. Patil, S., et al., *Combined Atomic Force Microscopy and Fluorescence Correlation Spectroscopy Measurements to Study the Dynamical Structure of Interfacial Fluids.* Langmuir, 2007. 23(9): p. 4988-4992.

67. Fukuma, T., M.J. Higgins, and S.P. Jarvis, *Direct Imaging of Individual Intrinsic Hydration Layers on Lipid Bilayers at Angstrom Resolution.* Biophysical Journal, 2007. 92(10): p. 3603-3609.

68. Butt, H.J., B. Cappella, and M. Kappl, *Force Measurements with the Atomic Force Microscope: Technique, Interpretation and Applications.* Surface Science Reports, 2005. 59(1-6): p. 1-152.

69. Lim, R. and S.J. O'Shea, *Solvation Forces in Branched Molecular Liquids.* Physical Review Letters, 2002. 88(24).

70. Israelachvili, J.N., et al., *Forces between Mica Surfaces across Hydrocarbon Liquids - Effects of Branching and Polydispersity.* Macromolecules, 1989. 22(11): p. 4247-4253.

71. Zhu, Y.X. and S. Granick, *Superlubricity: A Paradox about Confined Fluids Resolved.* Physical Review Letters, 2004. 93(9).

72. Gourdon, D. and J. Israelachvili, *Comment on "Superlubricity: A Paradox about Confined Fluids Resolved".* Physical Review Letters, 2006. 96(9).

73. Wong, J.S., et al., *Comment on "Superlubricity: A Paradox about Confined Fluids Resolved" - Reply.* Physical Review Letters, 2006. 96(9).

74. Fuhrmann, D. and A.P. Graham, *Spectroscopy of the Conformational Disorder in Molecular Films: Tetracosane and Squalane on Pt(111).* Journal of Chemical Physics, 2004. 120(5): p. 2439-2444.

75. Fuhrmann, D., et al., *Effects of Chain Branching on the Monolayer Structure of Alkanes at Interfaces: a Neutron and Helium Atom Scattering Study.* Surface Science, 2001. 482: p. 77-82.

76. Mo, H.D., G. Evmenenko, and P. Dutta, *Ordering of Liquid Squalane near a Solid Surface.* Chemical Physics Letters, 2005. 415(1-3): p. 106-109.

77. Enevoldsen, A.D., et al., *Comparative Study of Normal and Branched Alkane Monolayer Films Adsorbed on a Solid Surface. I. Structure.* Journal of Chemical Physics, 2007. 126(10).

78. Mitchell, D.J., B.W. Ninham, and B.A. Pailthorpe, Journal of the Chemical Society Faraday Transactions II, 1978. 74: p. 1089.

79. The Collected Works of Irving Langmuir, ed. C. Guy Smith (Pergamon, Oxford, 1961), vol. 6-9.
80. Deryaguin, B.V. and L.D. Landau, Acta Physico-Chem.U.R.S.S., 1941. 14: p. 633.
81. Onsager, L., Ann. N.Y. Acad. Sci., 1949. 51: p. 627.
82. Langmuir, I., Journal of Chemical Physics, 1938. 6: p. 873.
83. Mitchell, D.J., B.W. Ninham, and B.A. Pailthorpe, Journal of the Chemical Society Faraday Transactions II, 1978. 74: p. 1116.
84. Abraham, F.F., Journal of Chemical Physics, 1978. 68: p. 3713.
85. I., S., *Structure of Dense Liquids at Solid Interfaces.* Journal of Chemical Physics, 1979. 70: p. 3099.
86. I.K., S., Journal of Chemical Physics, 1978. 68: p. 2134.
87. Snook, I.K. and W. Vanmegen, *Solvation Forces in Simple Dense Fluids.1.* Journal of Chemical Physics, 1980. 72(5): p. 2907-2913.
88. Magda, J.J., M. Tirrell, and H.T. Davis, *Molecular-Dynamics of Narrow, Liquid-Filled Pores.* Journal of Chemical Physics, 1985. 83(4): p. 1888-1901.
89. Tarazona, P., U.M.B. Marconi, and R. Evans, *Phase-Equilibria of Fluid Interfaces and Confined Fluids - Nonlocal versus Local Density Functionals.* Molecular Physics, 1987. 60(3): p. 573-595.
90. Tarazona, P. and L. Vicente, *A Model For Density Oscillations In Liquids Between Solid Walls.* Molecular Physics, 1985. 56(3): p. 557-572.
91. Tarazona, P., *Free-Energy Density Functional For Hard-Spheres.* Physical Review A, 1985. 31(4): p. 2672-2679.
92. Vanderlick, T.K., L.E. Scriven, and H.T. Davis, *Molecular Theories of Confined Fluids.* Journal of Chemical Physics, 1989. 90(4): p. 2422-2436.
93. Cui, S.T., P.T. Cummings, and H.D. Cochran, *Effect of Branches on the Structure of Narrowly Confined Alkane Fluids: n-Hexadecane and 2,6,11,15-Tetramethylhexadecane.* Journal of Chemical Physics, 2001. 114(14): p. 6464-6471.

94. Gao, J.P., W.D. Luedtke, and U. Landman, *Structure and Solvation Forces in Confined Films: Linear and Branched Alkanes.* Journal of Chemical Physics, 1997. 106(10): p. 4309-4318.

95. Wang, J.C. and K.A. Fichthorn, *Effects of Chain Branching on the Structure of Interfacial Films of Decane Isomers.* Journal of Chemical Physics, 1998. 108(4): p. 1653-1663.

96. Wang, Y., K. Hill, and J.G. Harris, *Comparison of Branched and Linear Octanes in the Surface Force Apparatus - A Molecular-Dynamics Study.* Langmuir, 1993. 9(8): p. 1983-1985.

97. Ghatak, C. and K.G. Ayappa, *Solvation Force, Structure and Thermodynamics of Fluids Confined in Geometrically Rough Pores.* Journal of Chemical Physics, 2004. 120(20): p. 9703-9714.

98. Porcheron, F., M. Schoen, and A.H. Fuchs, *Monte Carlo Simulation of a Complex Fluid Confined to a Pore with Nanoscopically Rough Walls.* Journal of Chemical Physics, 2002. 116(13): p. 5816-5824.

99. Tartaglino, U., et al., *Impact of Molecular Structure on the Lubricant Squeeze-Out between Curved Surfaces with Long Range Elasticity.* Journal of Chemical Physics, 2006. 125(1).

100. Dijkstra, M., *Confined Thin Films of Linear and Branched Alkanes.* Journal of Chemical Physics, 1997. 107(8): p. 3277-3288.

101. Mundy, C.J., et al., *Equilibrium and Non-Equilibrium Simulation Studies of Fluid Alkanes in Bulk and at Interfaces.* Faraday Discussions, 1996: p. 17-36.

102. Wang, J.C. and K.A. Fichthorn, *Molecular Dynamics Studies of the Effects of Chain Branching on the Properties of Confined Alkanes.* Journal of Chemical Physics, 2002. 116(1): p. 410-417.

103. Wang, Y.T., K. Hill, and J.G. Harris, *Confined Thin-Films of a Linear and Branched Octane - A Comparison of the Structure and Solvation Forces Using Molecular-Dynamics Simulations.* Journal of Chemical Physics, 1994. 100(4): p. 3276-3285.

104. Persson, B.N.J. and F. Mugele, *Squeeze-out and Wear: Fundamental Principles and Applications.* Journal of Physics-Condensed Matter, 2004. 16(10): p. R295-R355.

105. Lantz, M.A., et al., *Atomic-Force-Microscope Study of Contact Area and Friction on $NbSe_2$.* Physical Review B, 1997. 55(16): p. 10776-10785.

106. Maugis, D., *Adhesion of Spheres - The JKR-DMT Transition using a Dugdale Model.* Journal of Colloid and Interface Science, 1992. 150(1): p. 243-269.

107. Lantz, M.A., S.J. O'Shea, and M.E. Welland, *Simultaneous Force and Conduction Measurements in Atomic Force Microscopy.* Physical Review B, 1997. 56(23): p. 15345-15352.

108. Carpick, R.W., D.F. Ogletree, and M. Salmeron, *A General Equation for Fitting Contact Area and Friction vs. Load Measurements.* Journal of Colloid and Interface Science, 1999. 211(2): p. 395-400.

109. Jansen, A.G.M., A.P. Vangelder, and P. Wyder. *Point-Contact Spectroscopy in Metals.* J. Phys. C, 1980. 13(33): p. 6073.

110. Maxwell, J.C., A Treatise on Electricity and Magnetism (Oxford, 1904).

111. Sharvin, Y., *A Possible Method for Studying Fermi Surfaces.* Sov. Phys. JETP, 1965. 21: p. 655.

112. G.Simmons, J., *Generalized Thermal J-V Characteristic for the Electric Tunnel Effect.* Journal of Applied Physics, 1964. 35(9): p. 2655-2658.

113. Engelkes, V.B., J.M. Beebe, and C.D. Frisbie, *Length-Dependent Transport in Molecular Junctions Based on SAMs of Alkanethiols and Alkanedithiols: Effect of Metal Work Function and Applied Bias on Tunneling Efficiency and Contact Resistance.* Journal of the American Chemical Society, 2004. 126(43): p. 14287-14296.

114. Wang, W.Y., T. Lee, and M.A. Reed, *Mechanism of Electron Conduction in Self-Assembled Alkanethiol Monolayer Devices.* Physical Review B, 2003. 68(3).

115. Cyr, D.M., B. Venkataraman, and G.W. Flynn, *STM Investigations of Organic Molecules Physisorbed at the Liquid-Solid Interface.* Chemistry of Materials, 1996. 8(8): p. 1600-1615.

116. Liang, W., et al., *Electronic Origin of Scanning-Tunneling-Microscopy Images and Carbon Skeleton Orientations of Normal-Alkanes Adsorbed on Graphite.* Advanced Materials, 1993. 5(11): p. 817-821.

117. Fisher, A.J. and P.E. Blochl, *Adsorption and Scanning-Tunneling-Microscope Imaging of Benzene on Graphite and MoS_2.* Physical Review Letters, 1993. 70(21): p. 3263-3266.

118. Faglioni, F., et al., *Theoretical Description of the STM Images of Alkanes and Substituted Alkanes Adsorbed on Graphite.* Journal of Physical Chemistry B, 1997. 101(31): p. 5996-6020.

119. Landauer, R., *Electrical Resistance of Disordered One-Dimensional Lattices.* Philosophical Magazine, 1970. 21(172): p. 863.

120. Oliver, W.C. and G.M. Pharr, *Measurement of Hardness and Elastic Modulus by Instrumented Indentation: Advances in Understanding and Refinements to Methodology.* Journal of Materials Research, 2004. 19(1): p. 3-20.

121. Gregory, S., *Inelastic Tunneling Spectroscopy and Single-Electron Tunneling in an Adjustable Microscopic Tunnel Junction.* Physical Review Letters, 1990. 64(6): p. 689-692.

122. Reed, M.A., et al., *Conductance of a Molecular Junction.* Science, 1997. 278(5336): p. 252-254.

123. Frank, S., et al., *Carbon Nanotube Quantum Resistors.* Science, 1998. 280(5370): p. 1744-1746.

124. Slowinski, K., et al., *Evidence for Inefficient Chain-to-Chain Coupling in Electron Tunneling through Liquid Alkanethiol Monolayer Films on Mercury.* Journal of the American Chemical Society, 1996. 118(19): p. 4709-4710.

125. Slowinski, K., et al., *Through-Bond and Chain-to-Chain Coupling. Two Pathways in Electron Tunneling through Liquid Alkanethiol Monolayers on Mercury Electrodes.* Journal of the American Chemical Society, 1997. 119(49): p. 11910-11919.

126. Wold, D.J. and C.D. Frisbie, *Formation of Metal-Molecule-Metal Tunnel Junctions: Microcontacts to Alkanethiol Monolayers with a Conducting AFM tip.* Journal of the American Chemical Society, 2000. 122(12): p. 2970-2971.

127. Wold, D.J., et al., *Distance Dependence of Electron Tunneling through Self-Assembled Monolayers Measured by Conducting Probe Atomic Force Microscopy: Unsaturated versus Saturated Molecular Junctions.* Journal of Physical Chemistry B, 2002. 106(11): p. 2813-2816.

128. Wold, D.J. and C.D. Frisbie, *Fabrication and Characterization of Metal-Molecule-Metal Junctions by Conducting Probe Atomic Force Microscopy.* Journal of the American Chemical Society, 2001. 123(23): p. 5549-5556.

129. Beebe, J.M., et al., *Contact Resistance in Metal-Molecule-Metal Junctions based on Aliphatic SAMs: Effects of Surface Linker and Metal Work Function.* Journal of the American Chemical Society, 2002. 124(38): p. 11268-11269.

130. Salomon, A., et al., *Comparison of Electronic Transport Measurements on Organic Molecules.* Advanced Materials, 2003. 15(22): p. 1881-1890.

131. Li, X.L., et al., *Conductance of Single Alkanedithiols: Conduction Mechanism and Effect of Molecule-Electrode Contacts.* Journal of the American Chemical Society, 2006. 128(6): p. 2135-2141.

132. Gruter, L., et al., *Electrical Conductance of Atomic Contacts in Liquid Environments.* Small, 2005. 1(11): p. 1067-1070.

133. Burnham, N.A., et al., *Scanning Local-Acceleration Microscopy.* Journal of Vacuum Science & Technology B, 1996. 14(2): p. 794-799.

134. Florin, E.L., et al., *Atomic-Force Microscope with Magnetic Force Modulation.* Review of Scientific Instruments, 1994. 65(3): p. 639-643.

135. Pierson, H.O., *Handbook of carbon, graphite, diamond and fullerenes: properties, processing, and applications*, Noyes Publications, Park Ridge, NJ (1993).

136. Bailey, S.W., *Classification and Structures of the Micas.* Reviews in Mineralogy, 1984. 13: p. 1-12.

137. www.chemistry.binghamton.edu/ZHONG/spm/afmmica1.htm.

138. Cleveland, J.P., et al., *A Nondestructive Method for Determining the Spring Constant of Cantilevers for Scanning Force Microscopy.* Review of Scientific Instruments, 1993. 64(2): p. 403-405.

139. Hazel, J.L. and V.V. Tsukruk, *Spring Constants of Composite Ceramic/gold Cantilevers for Scanning Probe Microscopy.* Thin Solid Films, 1999. 339(1-2): p. 249-257.

140. Kaye, G. and T. Laby, *Tables of Physical and Chemical Constants (Longman, London, UK, 1973).*

141. Derose, J.A., et al., *Gold Grown Epitaxially on Mica - Conditions for Large Area Flat Faces.* Surface Science, 1991. 256(1-2): p. 102-108.

142. Barth, J.V., et al., *Scanning Tunneling Microscopy Observations on the Reconstructed Au(111) Surface - Atomic-Structure, Long-Range Superstructure, Rotational Domains, and Surface-Defects.* Physical Review B, 1990. 42(15): p. 9307-9318.

143. Woll, C., et al., *Determination of Atom Positions at Stacking-Fault Dislocations on Au(111) by Scanning Tunneling Microscopy.* Physical Review B, 1989. 39(11): p. 7988-7991.

144. Hulsken, B., J.W. Gerritsen, and S. Speller, *Measuring the Au(111) Surface State at the Solid-Liquid Interface.* Surface Science, 2005. 580(1-3): p. 95-100.

145. Schreiber, F., *Structure and Growth of Self-Assembling Monolayers.* Progress in Surface Science, 2000. 65(5-8): p. 151-256.

146. Schwartz, D.K., *Mechanisms and Kinetics of Self-Assembled Monolayer Formation.* Annual Review of Physical Chemistry, 2001. 52: p. 107-137.

147. Poirier, G.E., *Mechanism of Formation of Au Vacancy Islands in Alkanethiol Monolayers on Au(111).* Langmuir, 1997. 13(7): p. 2019-2026.

148. Edinger, K., et al., *Formation of Self-Assembled Monolayers of N-Alkanethiols on Gold - A Scanning Tunneling Microscopy Study on the Modification of Substrate Morphology.* Langmuir, 1993. 9(1): p. 4-8.

149. Poirier, G.E., *Characterization of Organosulfur Molecular Monolayers on Au(111) using Scanning Tunneling Microscopy.* Chemical Reviews, 1997. 97(4): p. 1117-1127.

150. Poirier, G.E. and M.J. Tarlov, *The C(4x2) Superlattice of N-Alkanethiol Monolayers Self-Assembled an Au(111).* Langmuir, 1994. 10(9): p. 2853-2856.

151. Bucher, J.P., L. Santesson, and K. Kern, *Selective Imaging of Self-Assembled Monolayers by Tunneling Microscopy.* Applied Physics A-Materials Science & Processing, 1994. 59(2): p. 135-138.

152. Nuzzo, R.G., E.M. Korenic, and L.H. Dubois, *Studies of the Temperature-Dependent Phase-Behavior of Long-Chain Normal-Alkyl Thiol Monolayers on Gold.* Journal of Chemical Physics, 1990. 93(1): p. 767-773.

153. Camillone, N., et al., *Superlattice Structure At The Surface of a Monolayer of Octadecanethiol Self-Assembled on Au(111).* Journal of Chemical Physics, 1993. 98(4): p. 3503-3511.

154. Mar, W. and M.L. Klein, *Molecular-Dynamics Study of the Self-Assembled Monolayer Composed of $S(CH_2)(14)CH_3$ Molecules using an all-Atoms Model.* Langmuir, 1994. 10(1): p. 188-196.

155. Fenter, P., A. Eberhardt, and P. Eisenberger, *Self-Assembly of n-Alkyl Thiols as Disulfides on Au(111).* Science, 1994. 266(5188): p. 1216-1218.

156. Yeganeh, M.S., et al., *Interfacial Atomic-Structure of a Self-Assembled Alkyl Thiol Monolayer Au(111) - A Sum-Frequency Generation Study.* Physical Review Letters, 1995. 74(10): p. 1811-1814.

157. Smith, R.K., P.A. Lewis, and P.S. Weiss, *Patterning Self-Assembled Monolayers.* Progress in Surface Science, 2004. 75(1-2): p. 1-68.

158. Christenson, H.K., *Experimental Measurements of Solvation Forces on Non-Polar Liquids.* Journal of Chemical Physics, 1983. 78(11): p. 6906-6913.

159. Gosvami, N.N., et al., *Solvation and Squeeze Out of Hexadecane on Graphite.* Journal of Chemical Physics, 2007. 126(21).

160. He, M.Y., et al., *Effect of Interfacial Liquid Structuring on the Coherence Length in Nanolubrication.* Physical Review Letters, 2002. 88(15).

161. Israelachvili, J.N., S.J. Kott, and L.J. Fetters, *Measurements of Dynamic Interactions in Thin-Films of Polymer Melts - The Transition from Simple to Complex Behavior.* Journal of Polymer Science Part B-Polymer Physics, 1989. 27(3): p. 489-502.

162. Israelachvili, J.N. and P.M. McGuiggan, *Forces between Surfaces in Liquids.* Science, 1988. 241(4867): p. 795-800.

163. Klein, D.L. and P.L. McEuen, *Conducting Atomic-Force Microscopy of Alkane Layers on Graphite.* Applied Physics Letters, 1995. 66(19): p. 2478-2480.

164. Patil, S., et al., *Solid or liquid? Solidification of a Nanoconfined Liquid under Nonequilibrium Conditions.* Langmuir, 2006. 22(15): p. 6485-6488.

165. Persson, B.N.J. and P. Ballone, *Squeezing Lubrication Films: Layering Transition for Curved Solid Surfaces with Long-Range Elasticity.* Journal of Chemical Physics, 2000. 112(21): p. 9524-9542.

166. Sivebaek, I.M., V.N. Samoilov, and B.N.J. Persson, *Squeezing Molecular Thin Alkane Lubrication Films between Curved Solid Surfaces with Long-Range Elasticity: Layering Transitions and Wear.* Journal of Chemical Physics, 2003. 119(4): p. 2314-2321.

167. Lim, R., *Solvation Forces in Confined Molecular Liquids.* PhD Thesis, National University of Singapore, 2003.

168. Israelachvili, J.N., et al., *Entropic Orientational Forces between Surfaces in Anisotropic Liquids.* Langmuir, 1989. 5(4): p. 1111-1113.

169. O'Shea, S.J., M.E. Welland, and T. Rayment, *an Atomic-Force Microscope Study of Grafted Polymers on Mica.* Langmuir, 1993. 9(7): p. 1826-1835.

170. Thibaudau, F., G. Watel, and J. Cousty, *Scanning Tunneling Microscopy Imaging of Alkane Bilayers Adsorbed on Graphite - Mechanism of Contrast.* Surface Science, 1993. 281(1-2): p. L303-L307.

171. Watel, G., F. Thibaudau, and J. Cousty, *Direct Observation of Long-Chain Alkane Bilayer Films on Graphite by Scanning Tunneling Microscopy.* Surface Science, 1993. 281(1-2): p. L297-L302.

172. Bruch, L.W., R.D. Diehl, and J.A. Venables, *Progress in the Measurement and Modeling of Physisorbed Layers.* Reviews of Modern Physics, 2007. 79(4): p. 1381-1454.

173. Castro, M.A., et al., *Competitive Adsorption of Simple Linear Alkane Mixtures onto Graphite.* Journal of Physical Chemistry B, 1998. 102(51): p. 10528-10534.

174. Espeau, P. and J.W. White, *Thermodynamic Properties of n-Alkanes in Porous Graphite.* Journal of the Chemical Society-Faraday Transactions, 1997. 93(17): p. 3197-3200.

175. Castro, M., et al., *New Scattering Techniques to Characterise the Structure of Solid Monolayers Adsorbed from Condensed Phases to Solid Substrates.* Physica B, 1997. 241: p. 1086-1088.

176. Clarke, S.M., *Neutron Diffraction and Incoherent Neutron Scattering from Adsorbed layers.* Current Opinion in Colloid & Interface Science, 2001. 6(2): p. 118-125.

177. Winkler, R.G., et al., *Molecular Dynamics Simulation Study of the Dynamics of Fluids in Thin Films.* Journal of Chemical Physics, 1996. 104(20): p. 8103-8111.

178. Askadskaya, L. and J.P. Rabe, *Anisotropic Molecular-Dynamics in the Vicinity of Order-Disorder Transitions in Organic Monolayers.* Physical Review Letters, 1992. 69(9): p. 1395-1398.

179. Enachescu, M., et al., *Integration of Point-Contact Microscopy and Atomic-Force Microscopy: Application to Characterization of Graphite/Pt(111).* Physical Review B, 1999. 60(24): p. 16913-16919.

180. Lantz, M.A., S.J. O'Shea, and M.E. Welland, *Characterization of Tips for Conducting Atomic Force Microscopy in Ultrahigh Vacuum.* Review of Scientific Instruments, 1998. 69(4): p. 1757-1764.

181. Mate, C.M., et al., *Direct Measurement of Forces during Scanning Tunneling Microscope Imaging of Graphite.* Surface Science, 1989. 208(3): p. 473-486.

182. Ogbazghi, A.Y., *Conductance through Nanometer-scale Metal-to-Graphite Contacts.* PhD Thesis, 2005.

183. Cui, X.D., et al., *Making Electrical Contacts to Molecular Monolayers.* Nanotechnology, 2002. 13(1): p. 5-14.

184. Uchic, M.D., et al., *Sample Dimensions Influence Strength and Crystal Plasticity.* Science, 2004. 305(5686): p. 986-989.

185. Agrait, N., G. Rubio, and S. Vieira, *Plastic Deformation in Nanometer Scale Contacts.* Langmuir, 1996. 12(19): p. 4505-4509.

186. Butt, H.J. and V. Franz, *Rupture of Molecular Thin Films Observed in Atomic Force Microscopy. I. Theory.* Physical Review E, 2002. 66(3).

187. Butt, H.H. and R. Stark, *Atomic Force Microscopy in Structured Liquids: Remark on the Interpretation of Jumps in Force Curves.* Colloids and Surfaces A-Physicochemical and Engineering Aspects, 2005. 252(2-3): p. 165-168.

188. Franz, V. and H.J. Butt, *Confined Liquids: Solvation Forces in Liquid Alcohols between Solid Surfaces.* Journal of Physical Chemistry B, 2002. 106(7): p. 1703-1708.

189. Loi, S., et al., *Rupture of Molecular Thin Films Observed in Atomic Force Microscopy. II. Experiment.* Physical Review E, 2002. 66(3).

190. Persson, B.N.J. and E. Tosatti, *Layering Transition in Confined Molecular Thin-Films - Nucleation and Growth.* Physical Review B, 1994. 50(8): p. 5590-5599.

191. Yang, C., U. Tartaglino, and B.N.J. Persson, *How do Liquids Confined at the Nanoscale Influence Adhesion?* Journal of Physics-Condensed Matter, 2006. 18(50): p. 11521-11530.

192. Dubois, L.H. and R.G. Nuzzo, *Synthesis, Structure, and Properties of Model Organic-Surfaces.* Annual Review of Physical Chemistry, 1992. 43: p. 437-463.

193. Love, J.C., et al., *Self-Assembled Monolayers of Thiolates on Metals as a form of Nanotechnology.* Chemical Reviews, 2005. 105(4): p. 1103-1169.

194. Wang, W.Y., T. Lee, and M.A. Reed, *Electron Tunnelling in Self-Assembled Monolayers.* Reports on Progress in Physics, 2005. 68(3): p. 523-544.

195. Song, H., H. Lee, and T. Lee, *Intermolecular Chain-to-Chain Tunneling in Metal-Alkanethiol-Metal Junctions.* Journal of the American Chemical Society, 2007. 129(13): p. 3806.

196. Leng, Y.S. and S.Y. Jiang, *Atomic Indentation and Friction of Self-Assembled Monolayers by Hybrid Molecular Simulations.* Journal of Chemical Physics, 2000. 113(19): p. 8800-8806.

197. Tutein, A.B., S.J. Stuart, and J.A. Harrison, *Indentation Analysis of Linear-Chain Hydrocarbon Monolayers Anchored to Diamond.* Journal of Physical Chemistry B, 1999. 103(51): p. 11357-11365.

198. Thomas, R.C., et al., *The Mechanical Response of Gold Substrates Passivated by Self-Assembling Monolayer Films.* Science, 1993. 259(5103): p. 1883-1885.

199. Tutein, A.B., S.J. Stuart, and J.A. Harrison, *Role of Defects in Compression and Friction of Anchored Hydrocarbon Chains on Diamond.* Langmuir, 2000. 16(2): p. 291-296.

200. Engelkes, V.B. and C.D. Frisbie, *Simultaneous Nanoindentation and Electron Tunneling through Alkanethiol Self-Assembled Monolayers.* Journal of Physical Chemistry B, 2006. 110(20): p. 10011-10020.

201. Bonner, T. and A. Baratoff, *Molecular Dynamics Study of Scanning Force Microscopy on Self-Assembled Monolayers.* Surface Science, 1997. 377(1-3): p. 1082-1086.

202. Siepmann, J.I. and I.R. McDonald, *Monte-Carlo Simulation of the Mechanical Relaxation of a Self-Assembled Monolayer.* Physical Review Letters, 1993. 70(4): p. 453-456.

203. Sandroff, C.J., S. Garoff, and K.P. Leung, *Surface-enhanced Raman study of the solid/liquid interface: Conformational changes in adsorbed molecules.* Chemical Physics Letters, 1983. 96(5): p. 547.

204. Anderson, M.R., M.N. Evaniak, and M. Zhang, *Influence of Solvent on the Interfacial Structure of Self-Assembled Alkanethiol Monolayers.* Langmuir, 1996. 12(10): p. 2327-2331.

List of Publications

Journals

1. ***N. N. Gosvami***, S.K. Sinha and S. J. O'Shea, "Squeeze out of Branched Alkanes on Graphite", ***Physical Review Letters*** **100, (2008) 076101.**

2. ***N. N. Gosvami***, S.K. Sinha, M. P. Srinivasan, S. J. O'Shea, "Effect of Surrounding Medium on Resistance of a Molecular Monolayer Junction", ***Journal of Physical Chemistry C,*** **112, (2008) 297 -302.**

3. ***N. N. Gosvami***, W. Hofbauer, S. J. O'Shea, S.K. Sinha, "Solvation and Squeeze out of Hexadecane on Graphite", ***Journal of Chemical Physics*** **126, (2007) 214708.**

4. N. Satyanarayana, ***N. N. Gosvami***, S. K. Sinha, M.P. Srinivasan, "Friction, adhesion and wear life studies of ultra-thin (<10nm) PFPE overcoated 3-Glycidoxypropyltrimethoxy silane SAM on Si surface", ***Philosophical Magazine, 87 (2007), 3209-3227.***

5. S. K. Mohanta, R. K. Soni, ***N. Gosvami***, S. Tripathy, "Morphological and micro-Raman investigations on Ar^{+}-ion irradiated nanostructured GaAs surface", ***Applied Surface Science,*** **253 (2007) 4531-4536.**

6. S.K. Mohanta**,** R. K. Soni, ***N. N. Gosvami***, A.P. Vajpeyi, S. Tripathy, "Structural modifications in InP nanostructures prepared by Ar+-ion irradiation", ***Journal of Applied Physics,*** **102, (2007) 074313.**

7. ***N. Gosvami,*** K. H. A. Lau S. K. Sinha, S. J. O'Shea*,* "Effect of End Groups on Contact Resistance of Alkanethiol Based Metal-Molecule-Metal Junctions using Current Sensing AFM"**,** ***Applied Surface Science,*** **252, (2006) 3956-3950.**

8. Han Gao, ***Nitya N. Gosvami***, Jie Deng, Le-Shon Tan, Melissa S. Sander, "A General and Simple Approach to Generate Dense, Uniform, Sub-100 nm Self-Assembled Monolayer Features on Surfaces Using Porous Anodic Alumina Templates", ***Langmuir, 22*** **(2006) 8078 - 8082.**

9. Kumar Bhupendra, Hao Gong, ***Nitya Nand Gosvami***, Ramam Akkipeddi**,** "Nano-scaled Electrical Homogeneity of Indium Zinc Oxide Films", ***Applied Physics Letters*****, 88,(2006), 093111.**